

## **INFORMATION TO USERS**

This manuscript has been reproduced from the microfilm master. UMI films the text directly from the original or copy submitted. Thus, some thesis and dissertation copies are in typewriter face, while others may be from any type of computer printer.

**The quality of this reproduction is dependent upon the quality of the copy submitted.** Broken or indistinct print, colored or poor quality illustrations and photographs, print bleedthrough, substandard margins, and improper alignment can adversely affect reproduction.

In the unlikely event that the author did not send UMI a complete manuscript and there are missing pages, these will be noted. Also, if unauthorized copyright material had to be removed, a note will indicate the deletion.

Oversize materials (e.g., maps, drawings, charts) are reproduced by sectioning the original, beginning at the upper left-hand corner and continuing from left to right in equal sections with small overlaps. Each original is also photographed in one exposure and is included in reduced form at the back of the book.

Photographs included in the original manuscript have been reproduced xerographically in this copy. Higher quality 6" x 9" black and white photographic prints are available for any photographs or illustrations appearing in this copy for an additional charge. Contact UMI directly to order.

# U·M·I

University Microfilms International  
A Bell & Howell Information Company  
300 North Zeeb Road, Ann Arbor, MI 48106-1346 USA  
313: 761-4700 800: 521-0600



Order Number 9123480

**Atmospheres of comets: Gas dynamic models and inference of  
kinematic parameters**

Hu, Hongyao, Ph.D.

The University of Arizona, 1991

**U·M·I**  
300 N. Zeeb Rd.  
Ann Arbor, MI 48106



## **NOTE TO USERS**

**THE ORIGINAL DOCUMENT RECEIVED BY U.M.I. CONTAINED PAGES WITH SLANTED AND POOR PRINT. PAGES WERE FILMED AS RECEIVED.**

**THIS REPRODUCTION IS THE BEST AVAILABLE COPY.**



**ATMOSPHERES OF COMETS:  
GAS DYNAMIC MODELS AND INFERENCE OF KINEMATIC PARAMETERS**

by  
**Hongyao Hu**

---

**A Dissertation Submitted to the Faculty of the  
DEPARTMENT OF PHYSICS  
In Partial Fulfillment of the Requirements  
for the Degree of  
DOCTOR OF PHILOSOPHY  
In the Graduate College  
THE UNIVERSITY OF ARIZONA**

**1991**

---

THE UNIVERSITY OF ARIZONA  
GRADUATE COLLEGE

As members of the Final Examination Committee, we certify that we have read  
the dissertation prepared by Hongyao Hu

entitled Atmospheres of Comets: Gas Dynamic Models and Inference of  
Kinematic Parameters

and recommend that it be accepted as fulfilling the dissertation requirement  
for the Degree of Doctor of Philosophy.

Harold P. Larson  
Harold P. Larson

April 8, 1991  
Date

Laurence G. McIntyre  
Laurence G. McIntyre

4-8-91  
Date

Robert H. Parmenter  
Robert H. Parmenter

April 8, 1991  
Date

K. C. Hsieh  
K. C. Hsieh

9 April 1991  
Date

Stanley Bashkin  
Stanley Bashkin

4/17/91  
Date

Final approval and acceptance of this dissertation is contingent upon the  
candidate's submission of the final copy of the dissertation to the Graduate  
College.

I hereby certify that I have read this dissertation prepared under my  
direction and recommend that it be accepted as fulfilling the dissertation  
requirement.

K. C. Hsieh  
Dissertation Director K. C. Hsieh

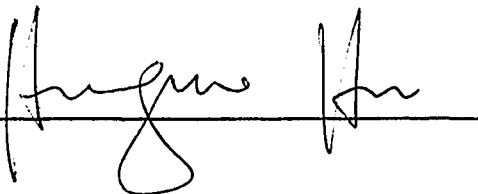
9 April 1991  
Date

**STATEMENT BY AUTHOR**

This thesis has been submitted in partial fulfillment of requirements for an advanced degree at The University of Arizona and is deposited in the University Library to be made available to borrowers under rules of the Library.

Brief quotations from this thesis are allowable without special permission, provided that accurate acknowledgement of source is made. Requests for permission for extended quotation from or reproduction of this manuscript in whole or in part may be granted by the head of the major department or the Dean of the Graduate College when in his or her judgement the proposed use of the material is in the interests of scholarship. In all other instances, however, permission must be obtained from the author.

SIGNED: \_\_\_\_\_

A handwritten signature in black ink, written over a horizontal line. The signature is cursive and appears to read "Hugues".

## ACKNOWLEDGEMENTS

I wish to thank my co-advisors, Drs. Harold P. Larson and K. C. Hsieh, for their support and helpful discussions in this research. Without their encouragement and guidance this thesis would not exist. Hal's excellence in scientific research helped me greatly during the last few years and his critical comments and suggestions had enormous influence over the formulation of the models and the writing of this dissertation.

I also thank Drs. Stanley Bashkin, Laurence C. McIntyre, William H. Wing and Robert H. Parmenter for their constructive criticisms on the dissertation and their services in my final examination committee.

I wish to extend my thanks and love to my wife, Jie, and my mother-in-law, ZHU Wenhuan. I am particularly grateful for their care and help during last few years when poor health caused me frequent physical exhaustion. My thanks and love also go to our baby, Jason (DuDu), whose smiles bring a lot of joy and happiness to my life. Finally, I would like to take this opportunity to thank my parents, HU Guoxin and LU Qingmei, my brother HU Tao, and my four sisters. Their constant encouragement and unconditional support throughout my undergraduate and graduate studies were the reason for any success I might have.

This thesis is dedicated to my grandmother (1900 - 1979).

## TABLE OF CONTENTS

LIST OF ILLUSTRATIONS .....	7
LIST OF TABLES .....	10
ABSTRACT .....	11
CHAPTER 1. INTRODUCTION .....	12
<b>PART I. GAS DYNAMIC MODELS OF COMETARY ATMOSPHERES</b>	
CHAPTER 2. A DILUTE GAS MODEL OF COMETARY ATMOSPHERES .	20
2.1. Introduction .....	20
2.2. Description of Cometary Comae .....	21
2.3. Derivation of the Cometary Boltzmann Equation .....	30
2.4. Direct Solutions of the Boltzmann Equation .....	35
CHAPTER 3. RELATIONSHIP OF THE COMETARY BOLTZMANN EQUATION TO OTHER GAS MODELS .....	38
3.1. The Cometary Transport Equation .....	41
3.2. The Haser Formula and the Cometary Boltzmann Equation .....	44
3.3. Molecular Excitation Conditions and the Cometary Boltzmann equation .....	50
3.4. Hydrodynamic Equations and the Cometary Boltzmann Equation .....	51
3.5. Monte Carlo Particle Trajectory Methods .....	59
CHAPTER 4. NEUTRAL GAS DENSITY DISTRIBUTIONS .....	64

4.1.	Introduction . . . . .	64
4.2.	Density Distributions for Non-uniform Velocity . . . . .	65
4.3.	Time-dependence and Anisotropy . . . . .	70
4.4.	The Outflow of H <sub>2</sub> O . . . . .	75

**PART II. INFERENCE OF KINEMATIC PARAMETERS FROM  
SPECTRAL LINE PROFILES**

<b>CHAPTER 5.</b>	<b>A SPECTRAL OUTFLOW MODEL . . . . .</b>	<b>82</b>
5.1.	Introduction . . . . .	82
5.2.	Line Broadening Mechanisms . . . . .	85
5.3.	The Physical Model . . . . .	89
5.4.	Computational Procedures . . . . .	95
5.5.	Molecular Spectral Line Shapes . . . . .	102
5.6.	Summary . . . . .	114
<b>CHAPTER 6.</b>	<b>APPLICATION TO OBSERVATIONS . . . . .</b>	<b>122</b>
6.1.	Introduction . . . . .	122
6.2.	Observations and Data Analysis . . . . .	123
6.2.	Interpretation of Cometary H <sub>2</sub> O Profiles . . . . .	132
6.4.	Summary . . . . .	166
<b>CHAPTER 7.</b>	<b>SUMMARY AND DISCUSSION . . . . .</b>	<b>170</b>
	<b>LIST OF REFERENCES . . . . .</b>	<b>174</b>

## LIST OF ILLUSTRATIONS

Figure	Page
1.1. The appearance of a comet . . . . .	13
3.1. The central relationship of the cometary Boltzmann equation to gas dynamic models of the coma . . . . .	40
3.2. Relationships between the cometary Boltzmann equation, the Haser model, and molecular excitation models . . . . .	49
3.3. Relationships between the cometary Boltzmann equation and hydrodynamic models of the coma . . . . .	57
3.4. Relationships between the cometary Boltzmann equation and Monte Carlo particle trajectory methods (MCPTM's) . . . . .	60
4.1a. The effect of production rate $Q_p$ on the $H_2O$ outflow velocity . . . . .	78
4.1b. The effect of heliocentric distance $R_h$ on the $H_2O$ outflow velocity . . . . .	79
4.2a. The effect of production rate $Q_p$ on the temperature profiles of $H_2O$ molecules . . . . .	80
4.2b. The effect of heliocentric distance $R_h$ on the temperature profiles of $H_2O$ molecules . . . . .	81
5.1. The cometocentric coordinate system for interpreting Earth-based observations . . . . .	90
5.2. Block diagram of the spectral outflow model computer program . . . . .	100
5.3. Comparison of typical monokinetic and hydrodynamic cometary lines . . . . .	103
5.4. Illustration of the effect of different expansion velocities on monokinetic profiles . . . . .	106

5.5.	Illustration of the effect of the FOV on monokinetic line profiles . . . . .	108
5.6.	Illustration of the effect of the FOV on hydrodynamic line profiles . . . . .	109
5.7.	Illustration of the effect of asymmetric outflow on hydrodynamic line profiles . . . . .	111
5.8.	Effect of the coma kinetic temperature on hydrodynamic line profiles . . . . .	113
5.9.	Effect of adding collisional broadening to monokinetic line profiles . . . . .	115
6.1.	KAO spectra of cometary H <sub>2</sub> O lines . . . . .	125
6.2.	H <sub>2</sub> O line profiles in comet P/Halley preperihelion . . . . .	129
6.3.	Functions $\cos^n(\theta)$ . . . . .	131
6.4.	Model fit to the deconvolved H <sub>2</sub> O line profile in comet P/Halley preperihelion . . . . .	134
6.5.	The two-dimensional column density map of H <sub>2</sub> O in comet P/Halley preperihelion . . . . .	135
6.6.	The velocity curves used in the kinematic model . . . . .	137
6.7.	H <sub>2</sub> O line profiles in comet P/Halley postperihelion . . . . .	142
6.8.	Model fit to the deconvolved H <sub>2</sub> O line profile in comet P/Halley postperihelion . . . . .	144
6.9.	The two-dimensional column density map of H <sub>2</sub> O in comet P/Halley postperihelion . . . . .	145
6.10.	Synthetic <i>in situ</i> H <sub>2</sub> O density profiles along hypothetical spacecraft trajectories . . . . .	154
6.11.	H <sub>2</sub> O line profiles in comet Wilson . . . . .	158

6.12.	Model fit to the deconvolved H <sub>2</sub> O line profile in comet Wilson . . . . .	159
6.13.	The two-dimensional column density map of H <sub>2</sub> O in comet Wilson . . . . .	160
6.14.	Comparison of the synthetic H <sub>2</sub> O profiles fit to comets Halley and Wilson with a Haser line profile . . . . .	167

**LIST OF TABLES**

<b>Table</b>		<b>Page</b>
5.1.	Contributions to cometary spectral line widths . . . . .	88
5.2.	Summary of spectral outflow models of cometary comae . . . . .	120
6.1.	Airborne IR observations of H <sub>2</sub> O in comets . . . . .	124
6.2.	Haser model fits to <i>in situ</i> observations of comet Halley . . . . .	152

## ABSTRACT

Cometary nuclei may be our best available probes of the physical and chemical nature of the presolar nebula. However, *in situ* sampling of cometary nuclei to determine their composition is generally not feasible. Instead, remote spectroscopic observations of cometary comae are used to infer cometary composition. This approach relies on one's ability to model accurately the density distributions of gas and dust in the comae and complex network of photochemical and molecular processes. Previously, a variety of theoretical models had been developed and, unfortunately, they are applicable only to a portion of the coma or to specific problems. In the first part of this thesis we introduce a preliminary version of a gas model built upon the concepts of dilute gas theory. This model is valid over the whole coma and it incorporates all previous models as its special cases, thus providing a new theoretical foundation for future cometary studies.

In the second part of the thesis we discuss a spectral outflow model. This model is a special case of the dilute gas model and is tailored specifically to retrieve kinematic properties of cometary comae from velocity-resolved spectral line profiles. We review the formation of cometary spectral line profiles and we develop an analytic expression that maps three dimensional number density distributions into synthetic spectral line profiles. After discussing simplifications and Monte Carlo computational procedures, we apply the spectral outflow model to interpret infrared observations of H<sub>2</sub>O in comets Halley and Wilson.

## CHAPTER 1

### INTRODUCTION

A comet observed from Earth usually consists of three parts: nucleus, coma and tails (Fig. 1.1). The *nucleus* is the core of the comet. As suggested by Whipple (1950, 1951), it is a solid mixture of mineral dust grains and ices of volatile materials. A typical cometary nucleus has a diameter of 1 - 10 km. The density of the nucleus is not well known; typical estimates lie between 0.1 - 1.0 g cm<sup>-3</sup>. This puts the mass of a comet between 10<sup>15</sup> - 10<sup>18</sup> g (or 10<sup>9</sup> - 10<sup>12</sup> metric tons). The *coma* or *atmosphere* of the comet develops as it approaches the Sun when the solar radiation "melts" the volatile ices on the surface of the nucleus and produces large quantities of dust grains and gases. The size of the coma depends on heliocentric distance, and is typically 10<sup>5</sup> - 10<sup>6</sup> km when the comet is 1 AU from the Sun. Besides the nucleus and coma, two tails are often developed (Fig. 1.1). The *ion tail* is formed by ionized gas molecules, while the *dust tail* is formed from dust dragged out by sublimating gases.

Cometary nuclei are the least modified materials remaining from the early solar system and may be our best available probes of physical and chemical conditions in the presolar nebula. It is therefore important to retrieve all information that is contained in cometary nuclei in order to understand the formation and evolution of our solar system. Since the last apparition of comet Halley there has been considerable interest in the continuing and in-depth studies of comets. Unfortunately, direct observations of cometary nuclei are impossible from Earth-based observatories due to their small size

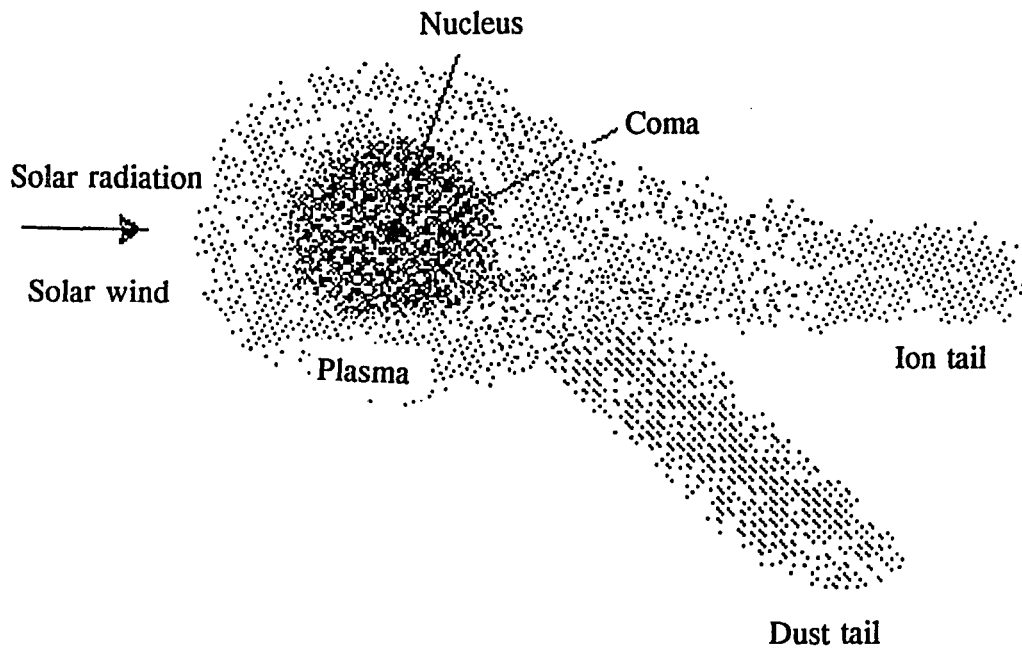


**Figure 1.1.** The appearance of a comet.

and lack of contrast between the nuclei and their surrounding comae. *In situ* sampling of cometary nuclei is still a very distant prospect. Instead, remote spectroscopic observations of cometary comae are used to infer cometary compositions. This approach relies on one's ability to model accurately the density distribution of gases and dust in the comae and the complex network of photochemical reactions and molecular processes that modify these materials.

The coma of a comet differs from the atmospheres of the planets such as Earth in two major aspects. First, the coma is a transient phenomenon that exists only when the comet comes near the Sun. Second, due to the small mass and low gravitational force of the nucleus, the gas molecules flow outward and disappear into interplanetary space. Compositional studies of cometary comae are important subjects because they provide the only direct link to materials in the nuclei. These properties distinguish the modelling of cometary comae from that of other atmospheres.

Models of cometary comae have developed rapidly during the last decade, but a unifying approach has not yet emerged. Rather, a variety of theoretical methods and techniques are being used. We classify previous coma models into four categories. The earliest study of a cometary coma was by Eddington (1910) who published a model that described space and column density distributions. The early studies of comet atmospheres treated the nucleus as a point-like source that emitted molecules isotropically. All of the emitted gas molecules were assumed to move radially outward with constant velocity and without collisions. The neutral gaseous molecules were eventually broken up by solar ultraviolet (UV) photons into daughter products which

remained at the same velocity as the parents and continued to flow outward until they were also destroyed by UV photons. The process repeated until all neutral species were dissociated into ions and electrons which eventually disappeared into interplanetary space. This simple, collisionless outflow is often referred to as a *Haser*-type model, attributed to a widely quoted paper by Haser (1957). In this thesis we will also refer to the Haser model as a *monokinetic model* because of its use of a single, uniform velocity to characterize the outflow.

A radically different approach to coma modeling uses *hydrodynamic* equations. The fundamental assumption in hydrodynamic models of the coma is that molecules in the coma are collisionally coupled so that local thermal equilibrium (LTE) is maintained. This ensures that the *Navier-Stokes* or *Euler* equations for a gaseous fluid are applicable and, consequently, that physical quantities such as outflow velocity, temperature, pressure, *etc.* may be calculated by numerical integration of the hydrodynamic equations.

While the hydrodynamic model is easily implemented with computer techniques, its scientific usefulness is limited by its requirement for intensive collisions. In an average cometary coma, collisions are restricted to the inner coma where the radial distance is smaller than  $10^3 - 10^4$  km. Very few collisions occur beyond  $r > 10^4$  km in the outer coma. To accommodate this situation some hydrodynamic modelers divide the coma into two zones: (1) a collision zone in the inner coma where the hydrodynamic equations apply, and (2) an outer free-flow zone where the Haser model applies. One drawback of this approach is its neglect of the transition region between the collision

and free-flow zones. In a real coma the collision rate decreases gradually so the transition region is very large and cannot be ignored.

*A third type of model, the Monte Carlo particle trajectory methods (MCPTM)* were first applied to cometary comae by Combi and Delsemme (1980). Their model was a random walk study of collisionless outflow of daughter products. The technique was quickly adapted by Bockelée-Morvan and Gérard (1984) to study Doppler-shifted OH radio line profiles. Kitamura *et al.* (1985) improved the random walk model by introducing collisions and two-dimensional geometry in their study of hydrogen comae. Recently, Combi and Smyth (1988) published a rather complete gas dynamic/MCPTM model where the parent gas in the inner coma was modeled by hydrodynamic equations and the movement of daughter products was treated by MCPTM. Hodges (1990) presented a theoretically more complete model in which all molecules were treated by the MCPTM.

The fourth type of coma model concerns the excitation properties of gas molecules. These models are important because the excitation of molecules and their subsequent emission of photons provide the only way to observe them. A molecular excitation model predicts the excitation properties of a molecular species by calculating the relative population distribution of its energy levels. The central equation of a molecular excitation model is the statistical equilibrium equation. However, density distributions and temperature profile must be imported from other models in order to solve the statistical equilibrium equation. So far, molecular excitation models have been built for H<sub>2</sub>O (Weaver and Mumma 1984, Bockelée-Morvan 1987), CO (Chin and

Weaver 1984), HCN and linear molecules (Crovisier 1987) and H<sub>2</sub>CO (Reuter *et al.* 1989).

All of these models or techniques contribute significantly to our current understanding of cometary comae and have led to the rapid expansion of theoretical cometary studies. Crifo (1989) estimated that before 1981 there was about one paper per year dealing with coma models, but after 1981 publications dealing with coma models increased rapidly to about 10 per year with much of the increase attributed to hydrodynamic methods. However, significant work remains. An intrinsic problem with these models is that they are applicable only to a portion of the coma or to specific problems. For example, the Haser model applies only to the outer coma because of the assumption that there are no collisions, while hydrodynamic models apply only to the inner coma due to its requirement for intensive collisions. Molecular excitation models are not self-determinate and require input from other models. Monte Carlo particle trajectory techniques depend on the particular formulation and algorithms have so far been developed only for problems with very simple geometries.

We therefore believe that a more comprehensive model must be introduced. Such a model should be valid over the whole coma and would incorporate all previous models as special cases. That is, the new model should be a unifying theory. The development of such a model is the primary objective of the first part of this thesis. In *Part I* we consider alternate ways in which gas dynamic principles may be incorporated into physical models of the coma. We present a preliminary version of a gas dynamic model built upon the concepts of dilute gas theory. The classical Boltzmann equation

of dilute gas is rederived for the more complicated cometary environment (Chapter 2). Although mathematically complex, the generalized cometary Boltzmann equation is valid over the whole coma and therefore provides a theoretical foundation that other models can relate to. We then demonstrate (Chapter 3) that such diverse coma models such as Haser outflow, molecular excitation, and hydrodynamic equations are all approximations that may be derived from the generalized Boltzmann equation. Coma models using Monte Carlo particle trajectory methods are actually statistical methods for solving the generalized Boltzmann equation.

Ideally, our dilute gas approach could be further developed to allow the calculation of very complex density distributions and kinematic properties in the coma, which can then be used to interpret the increasingly sophisticated data that already exist or will be obtained in the future. However, the generalized Boltzmann equation is an integral-differential equation that is very difficult to solve. Fortunately, the cometary Boltzmann equation provides a unifying approach to developing new and specialized models. In Chapter 4 we use the cometary Boltzmann equation as the starting point to demonstrate that some unrealistic assumptions associated with the Haser model can be readily removed in favor of more general number density formulae. These formulae are then used to develop a specialized model in *Part II*.

For convenience, we distinguish between two types of outflow models. One is the *gas dynamic model* where the emphasis is on calculating the density, expansion velocity, and kinetic temperature from gas dynamic principles. The second is a *spectral outflow model* used to infer the density, expansion velocity and kinetic temperature from

observed spectral line profiles. In Chapter 5 (see also Hu *et al.* 1991) we build a spectral outflow model for parent molecules in order to retrieve the kinematic properties of cometary comae. We review the formation of cometary spectral line profiles and incorporate the most important gas dynamic processes into an integral that maps three dimensional density distributions into synthetic line profiles. After discussing the simplifications and the Monte Carlo computational procedures that are required to make practical use of the model, we use it to make the first systematic study of the formation of spectral line profiles of parent molecules, including the influence of specific coma conditions such as field-of-view (FOV), expansion velocity, kinetic temperature, and anisotropic outflow distributions. This model is then applied to airborne infrared (IR) observations of H<sub>2</sub>O in comets P/Halley and Wilson (1987 VII) in Chapter 6 (see also Larson *et al.* 1991).

## CHAPTER 2

### A DILUTE GAS MODEL OF COMETARY ATMOSPHERES

#### 2.1. Introduction

Conventional statistical theory of gases is based on the assumption that intermolecular collisions are very intensive and, consequently, that a Maxwell-Boltzmann distribution describes the statistical nature of molecular motion. This assumption is adequate for the gas in environments such as Earth's atmosphere. However, the cometary atmospheres are unique in that gas number densities drop rapidly with an inverse square law. Consequently, the assumption of intensive collisions is invalid for most of a cometary atmosphere and non-equilibrium gas theory must be used.

The study of dilute gas theory can be traced back to the last century but major development came only after World War II due to growing interest in space and high altitude flights. Most of these studies are described as *rarefied gas dynamics* and a comprehensive record of activity in the field is available from the published proceedings of the *International Symposia on Rarefied Gas Dynamics* (see, e.g., Muntz *et al.* 1989). The kinematic theory of a dilute gas encompasses such diverse topics as internal flow in a vacuum system and aerodynamics of upper-atmospheres. The central theme in the study of a dilute gas is that the discrete nature of molecules cannot be ignored, hence the continuum approach is no longer valid. The fundamental equation of dilute gas theory is the Boltzmann equation. For a simple gas without internal freedom and in the absence of any external force, the Boltzmann equation may be written in the form (see,

*e.g.*, Bird 1976)

$$\frac{\partial f}{\partial t} + \mathbf{v} \cdot \frac{\partial f}{\partial \mathbf{r}} + \frac{\mathbf{F}}{m} \cdot \frac{\partial f}{\partial \mathbf{v}} = J(f) \quad (2.1)$$

where  $f$  is a distribution function,  $J(f)$  is a collision term,  $\mathbf{F}$  is external force, and  $\mathbf{v}$  is velocity. This equation is not adequate for representing the gaseous component of cometary comae, however. The first complication that must be addressed is that the coma contains multiple gas species. Even if the nucleus were pure water ice, the subliming  $\text{H}_2\text{O}$  molecules would soon become the source of H, OH, O, *etc.*, because of photodissociation by solar UV photons. In addition, collisions, radiative transfer, and radial expansion affect the state of the coma. In this chapter we present a preliminary version of a dilute gas model of cometary comae. Much of our effort is to generalize current theory to accommodate major physical processes and to include all gaseous species.

## 2.2. Description of Cometary Comae

### 2.2.1. Cometary comae as dilute gases

The number density of a gaseous component in a cometary coma can be calculated with the Haser formula or other expressions that will be presented in Chapter 3 and Chapter 4. Here we present some estimates of the number densities. The typical gas production rate in an average comet is  $10^{28} - 10^{29}$  molecules  $\text{sec}^{-1}$ , while a active

comet like comet Halley has a peak production rate of  $2 \times 10^{30}$  molecules  $\text{sec}^{-1}$ . The typical size of a cometary nucleus is 1 km, whereas comet Halley's radius is  $\approx 5$  km. To estimate the upper limit of gas density, we take a comet with a rather high production rate of  $2 \times 10^{30}$  molecules  $\text{sec}^{-1}$  and a nuclear radius 1 km. The gas number density is  $10^{14}$  molecules  $\text{cm}^{-3}$  near the nuclear surface of such a comet. The number density decreases with radial distance according to an approximate inverse square law. For comparison, the gas density is  $2.69 \times 10^{19}$  molecules  $\text{cm}^{-3}$  on Earth's surface. Thus we conclude that the gas density on the nuclear surface is indeed very low ( $\approx 10^{-5}$  that on Earth's surface). This low density could be achieved on Earth by a moderately good mechanical vacuum pump. This comparison demonstrates that the gas in cometary comae is *dilute*. A more precise definition of a dilute gas includes the following conditions:

- 1). The time between collisions is much greater than the duration of a collision.
- 2). Collisions involving three particles occur very rarely compared to two-particle collisions. The treatment of collisions can therefore be restricted to the simpler case of two interacting particles.
- 3). The two colliding particles are statistically uncorrelated (molecular chaos), *i.e.*, the last collision between the same particles was so long ago that neither "remembers" it.
- 4). Classical mechanics applies to the motion of molecules between collisions.

Cometary comae satisfy the above conditions. The typical distance between molecules is  $D = (1/n)^{1/3} \approx 10^{-5}$  cm and the typical size of molecules in the coma is  $d \approx 10^{-8}$  cm. The intermolecular force has a finite range with a typical radius  $\Delta < 10^{-7}$  cm. Bird (1976) stated that if  $D \gg d, \Delta$ , as is the case, then the first three conditions above are satisfied. The fourth condition is guaranteed because the de Broglie wavelength of a molecule is much smaller than the average distance between molecules.

### 2.2.2. Phase space and distribution functions

The state of a molecule is described by movement of its center of mass and its internal energy. The motion of the center of mass is represented by the spatial position  $\mathbf{r}$  and the velocity  $\mathbf{v}$  for a total of six degrees of freedom while the internal state is represented by an energy variable  $\varepsilon$ . We therefore describe the motion of this molecule in a generalized *phase space*  $(\mathbf{r}, \mathbf{v}, \varepsilon)$ . It is sometimes more convenient to denote  $\Gamma = (\mathbf{v}, \varepsilon)$  for all variables except the spatial coordinates of the molecules. Phase space is then denoted simply by  $(\mathbf{r}, \Gamma)$ . An infinitesimal volume element  $(d\mathbf{r}, d\mathbf{v}, \varepsilon_k)$  in phase space is defined as the region in which all molecules have spatial coordinates between  $(\mathbf{r}, \mathbf{r}+d\mathbf{r})$ , velocity between  $(\mathbf{v}, \mathbf{v}+d\mathbf{v})$ , and internal energy  $\varepsilon_k$ . We could also write the volume element as  $(d\mathbf{r}, d\Gamma)$ , where  $d\Gamma$  satisfies

$$d\Gamma = d\mathbf{v}|_{\varepsilon=k} \text{ and} \quad (2.2)$$

$$\int d\Gamma = \sum_k \int d\mathbf{v},$$

with the summation over all energy states.

Strictly speaking, a deterministic description of a cometary coma requires specification of the positions of all particles in phase space. Due to the large numbers of particles ( $N > 10^{33}$ ) in the coma, however, the deterministic description is almost impossible. Fortunately, a dilute gas may be described statistically by its *distribution function*  $f$ . We introduce the index  $s = \text{H}_2\text{O}, \text{OH}, \text{O}, \text{H}, \dots$  to denote particular species. The distribution function for the neutral coma is therefore a matrix  $f(\mathbf{r}, \Gamma, t) = \{f_s(\mathbf{r}, \mathbf{v}, \varepsilon_k, t), s = \text{H}_2\text{O}, \text{OH}, \text{O}, \text{H}, \text{HCN}, \dots; k = 1, 2, \dots\}$ . The matrix is defined such that  $f_s(\mathbf{r}, \mathbf{v}, \varepsilon_k, t) d\mathbf{r} d\Gamma$  is the mean number of molecules of species  $s$  for which at time  $t$  the center of mass is located between  $\mathbf{r}$  and  $\mathbf{r} + d\mathbf{r}$ , the center of mass has a velocity between  $\mathbf{v}$  and  $\mathbf{v} + d\mathbf{v}$ , and the energy is  $\varepsilon_k$ . The *total* distribution function of a species  $s$  is the sum of its distribution functions over all energy states:

$$f_s(\mathbf{r}, \mathbf{v}, t) = \sum_k f_s(\mathbf{r}, \mathbf{v}, \varepsilon_k, t). \quad (2.3)$$

The *spatial number density* of species  $s$  is calculated from

$$n_s(\mathbf{r}, t) = \int f_s(\mathbf{r}, \Gamma, t) d\Gamma, \quad (2.4)$$

while its *velocity distribution* is defined as

$$V_s(\mathbf{r}, \mathbf{v}, t) = \frac{f_s(\mathbf{r}, \mathbf{v}, t)}{n_s(\mathbf{r}, t)}. \quad (2.5)$$

It is easily demonstrated that the velocity distribution is normalized to unity. It is often assumed that the velocity distributions are independent of the energy states. If this assumption fails, the above definition only describes the overall properties of the species. To determine the dependence of the velocity distribution and density on the energy states, we would have to define them for each energy state.

### 2.2.3. Coma parameters

The functional matrix  $\{f(\mathbf{r}, \mathbf{v}, \epsilon, t)\}$  provides a *complete* description of the *microscopic* state of a coma from which all *macroscopic* quantities of interest could be calculated. For convenience, we call these macroscopic properties the *coma parameters*. All coma parameters such as temperature, outflow velocity, *etc.*, can be defined in direct analogy with those in dilute gas theory (see, *e.g.*, Bird 1976). One group of coma parameters includes macroscopic descriptions of certain average properties at each spatial point in the coma. If  $Q_s(\mathbf{r}, \mathbf{v}, \epsilon, t)$  is a general function that represents a property of molecule, its average or macroscopic value is

$$\langle Q_s \rangle = \frac{1}{n_s(\mathbf{r}, t)} \int Q_s(\mathbf{r}, \Gamma, t) f_s(\mathbf{r}, \Gamma, t) d\Gamma. \quad (2.6)$$

For example, the *average velocity*  $\mathbf{u}_s(\mathbf{r}, t)$  of species  $s$  is

$$\mathbf{u}_s(\mathbf{r}, t) = \frac{1}{n_s(\mathbf{r}, t)} \int \mathbf{v} f_s(\mathbf{r}, \Gamma, t) d\Gamma. \quad (2.7)$$

Since the direction of  $\mathbf{u}_s$  is often radially away from the cometary nucleus, it is commonly called the *outflow velocity*. In this thesis whenever we refer to the outflow velocity of a species we mean the average velocity as defined in Eq. 2.7. It is useful to divide the velocity of a molecule into the sum of two components: the average velocity just defined, and any velocity component relative to it. This second component is called the *thermal velocity* of the molecule and is defined by

$$\mathbf{v}'_s = \mathbf{v} - \mathbf{u}_s. \quad (2.8)$$

To describe the average value of the thermal velocity we have to take into account the fact that its simple average is zero. A higher order of moments is therefore utilized to describe the thermal velocity. The temperature tensor is defined by

$$\underline{\underline{T}}_s = \frac{m}{k_B} \int \mathbf{v}'_s \mathbf{v}'_s f_s(\mathbf{v}, \Gamma, t) d\Gamma \quad (2.9)$$

where  $k_B$  is Boltzmann's constant and  $m_s$  is the mass of molecules. The *translational temperature* is defined as the average of the diagonal terms

$$T_s = \frac{1}{3} (T_{11} + T_{22} + T_{33})_s = \frac{m}{3k_B} \langle (v'_s)^2 \rangle. \quad (2.10)$$

The total energy of a molecule is the sum of the kinetic energy of its center of mass and the internal energy, *i.e.*,  $\epsilon_s = \frac{1}{2}mv^2 + \epsilon_{\text{int}}$ . The average of  $\epsilon_s$  is

$$\begin{aligned}
\langle \epsilon_s \rangle &= \frac{1}{n_s} \int \epsilon_s f_s(r, \Gamma, t) d\Gamma \\
&= \frac{1}{2} m u_s^2 + \frac{3}{2} k_B T_s + \langle \epsilon_{int}^s \rangle.
\end{aligned}
\tag{2.11}$$

The first term on the right side is the *stream energy*, the second term is the *thermal energy*, and the third term is the *average internal energy*.

A second group of coma parameters is related to the velocity. Whenever there is movement of particles in the comae, the related physical properties flow with them. In general, the *flux* of a physical quantity  $Q_s(\mathbf{r}, \Gamma, t)$  is defined by

$$n_s \langle Q_s \mathbf{v} \rangle = \int \mathbf{v} Q_s f_s(r, \Gamma, t) d\Gamma. \tag{2.12}$$

Upon substituting  $\mathbf{v} = \mathbf{u}_s + \mathbf{v}'$  into Eq. 2.12, the flux  $n_s \langle Q_s \mathbf{v} \rangle$  becomes

$$n_s \langle Q_s \mathbf{v} \rangle = n_s \langle Q_s \rangle \mathbf{u}_s + n_s \langle Q_s \mathbf{v}' \rangle. \tag{2.13}$$

$\langle Q_s \rangle \mathbf{u}_s$  is called the *stream flux* of the species  $s$  and  $\langle Q_s \mathbf{v}' \rangle$  is the *thermal flux* (the portion due to thermal motion). If a physical quantity  $Q_s$  is a scalar (e.g., mass, energy) then its flux is a vector. If  $Q_s$  is a vector (i.e., momentum) then its flux is a tensor. Flux plays an important role in the consideration of conservation equations.

A few important thermal flux vectors are given below.

- 1). Mass flux. Let  $Q_s = m$ , then the mass flux  $= n_s \langle m \mathbf{v} \rangle = n_s m \mathbf{u}_s$ .

Mass flux is a stream flux, that is, the thermal flux of mass is zero.

2). Energy flux. Energy is a scalar, therefore energy flux is a vector. The heat flux, the portion of the energy flux due to local thermal motion, is given by

$$\mathbf{q} = n_s \int \mathbf{v}' \left( \frac{1}{2} m v'^2 + \varepsilon_k \right) f_s(r, \Gamma, t) d\Gamma, \quad (2.14)$$

while the stream energy flux of a molecule is given by

$$n_s \langle \varepsilon_s \rangle \mathbf{u} = n_s \left( \frac{1}{2} m u^2 + \frac{3}{2} k_B T_s + \langle \varepsilon_{int}^s \rangle \right) \mathbf{u}_s, \quad (2.15)$$

where  $\langle \varepsilon_{int} \rangle$  is the mean internal energy.

3). Momentum flux. Momentum is a vector, so momentum flux must be a tensor. The thermal momentum flux of species  $s$  is represented by a stress tensor

$$\underline{\underline{P}}_s = \int m \mathbf{v}' \mathbf{v}' f_s(r, \Gamma, t) d\Gamma. \quad (2.16)$$

The scalar pressure  $p_s$  is usually defined as the average of the three diagonal components of the stress tensor, *i.e.*,

$$p_s = \frac{1}{3} (P_{11} + P_{22} + P_{33}) = \frac{1}{3} n_s m \langle (v')^2 \rangle. \quad (2.17)$$

Upon comparing the definitions of pressure  $p_s$  (Eq. 2.17) and translational temperature

$T_s$  (Eq. 2.10) we have

$$p_s = n_s k_B T_s, \quad (2.18)$$

which is the *perfect gas equation* of species  $s$ . Note that the temperature  $T$  is defined from the random average point of view while the pressure  $p$  is defined from the point of view of momentum transfer. They satisfy the perfect gas equation only because of the dilute gas assumption. For a dense gas the two definitions will lead to a different relation between the two parameters. It is often convenient to subtract the scalar pressure  $p$  from the stress tensor. The viscous stress tensor is defined by

$$\underline{\underline{\mu}} \equiv \mu_{ij} = -(P_{ij} - \delta_{ij} p),$$

where  $\delta_{ij}$  is the Kronecker delta function.

The above definitions of averages and fluxes are compatible with general gas dynamics. The major advantage of using coma parameters to describe the coma is that they are measurable, while the distribution function  $f(\mathbf{r}, \Gamma, t)$  defined in the last section is often not. Fortunately, a distribution function  $f$  can be determined from a few macroscopic parameters under proper condition. For example, for LTE the total distribution function  $f_s$  could be calculated from the density  $n_s$ , the outflow velocity  $\mathbf{u}_s$ , and the kinetic temperature  $T_s$ . The algebraic form of the distribution function  $f_s$  is

$$f_s(r, \mathbf{v}, t) = n_s(r, t) \left( \frac{m}{2\pi k T_s} \right)^{3/2} \exp \left( -\frac{m}{2\pi k T_s} (\mathbf{v} - \mathbf{u}_s(r, t))^2 \right). \quad (2.20)$$

Therefore, if we could measure  $\{\mathbf{u}_s, T_s, n_s; s = \text{H}_2\text{O}, \text{OH}, \text{O}, \text{H}_2, \text{H} \dots\}$  then in principle we would have knowledge of whole coma. Other physical properties could then be derived from those parameters.

### 2.3. Derivation of the Cometary Boltzmann Equation

We introduced distribution functions to provide a statistical description of the coma. In order to evaluate dynamic properties of the coma, we must know the relationships that  $f(\mathbf{r}, \Gamma, t)$  must satisfy. The *Boltzmann equation* have been derived to a dilute gas of single species. In this section we derive a Boltzmann-type equation that represents major physical processes inside the coma. For historical reasons we call the this new equation the *cometary Boltzmann equation*.

We return to our generalized phase space  $(\mathbf{r}, \Gamma) = (\mathbf{r}, \mathbf{v}, \epsilon)$  for species  $s$ . We focus on an infinitesimally small volume element  $(d\mathbf{r}, d\Gamma) = (d\mathbf{r}, d\mathbf{v}, \epsilon_k)$  during a time interval  $(t, t+dt)$ . All molecules in this volume element possess an internal energy  $\epsilon_k$ , and their centers of mass are between  $(\mathbf{r}, \mathbf{r}+d\mathbf{r})$  and move at velocity  $(\mathbf{v}, \mathbf{v}+d\mathbf{v})$ . At the beginning of the time interval, the total number of molecules in this phase element is  $f_s(\mathbf{r}, \Gamma, t)d\mathbf{r}d\mathbf{v}$ , and at the end of the time interval the number of molecules changes to  $f_s(\mathbf{r}, \Gamma, t+dt)d\mathbf{r}d\mathbf{v}$ . That is, during this time interval the number of molecules inside the volume element changes by

$$\frac{\partial f_s}{\partial t} d\mathbf{v} d\mathbf{r} dt, \quad (2.21)$$

where  $\partial f_s / \partial t$  is the rate of change per unit phase volume per unit time for species  $s$ .

This increase in the volume element could be due several processes, including:

- (1) convection of the center of mass of molecules in and out of  $(dr, d\mathbf{r})$ ,
- (2) production or destruction of species  $s$  within  $drd\mathbf{r}$ ,
- (3) the change of internal state due to radiative processes, and
- (4) collisions.

The conservation equation for the molecules of species  $s$  in this volume element during the time interval is written as

$$\begin{aligned} \text{Flow in} - \text{Flow out} + \text{Production} - \text{Destruction} \\ = \text{Change due to time.} \end{aligned} \quad (2.22)$$

We evaluate each term in the sections below.

### 2.3.1. Convection of the center of mass

Since each molecule in  $(dr, dv, \epsilon_k)$  moves at a velocity  $\mathbf{v}$ , many would exit through the spatial boundary  $dr$  of the phase element in time period  $(t, t+dt)$  while other molecules would move in. Similarly, external forces  $\mathbf{F}$  would accelerate molecules and therefore cause them to flow in or out of the velocity boundary  $dv$  of  $(dr, dv, \epsilon_k)$ . The net change in the phase element due to convection is given by (Bird 1976)

$$-\left[ \mathbf{v} \cdot \frac{\partial f_s}{\partial \mathbf{r}} + \frac{\mathbf{F}}{m} \cdot \frac{\partial f_s}{\partial \mathbf{v}} \right] dr dv dt. \quad (2.23)$$

### 2.3.2. Production and destruction

For a photodestruction lifetime of  $\tau_s$ , the fraction of molecules that disappears during time  $(t, t+dt)$  is  $dt/\tau_s$ . Because there is a total of  $f_s dr dv$  molecules inside the phase element, the total number of molecules destroyed inside volume element is  $(f_s/\tau_s) dr dv dt$ . The rate of change of species  $s$  inside the volume element  $(dr, dv)$  due to photodestruction is

$$D_s(\mathbf{r}, \mathbf{v}, \varepsilon_k, t) = \frac{f_s(\mathbf{r}, \mathbf{v}, \varepsilon_k, t)}{\tau_s}. \quad (2.24)$$

Similarly we denote  $B_s(\mathbf{r}, \mathbf{v}, \varepsilon_k, t) dr dv dt$  as the net change for the production of species  $s$  in the volume element during time period  $(t, t+dt)$ . For parent molecules ( $s = p$ ) subliming from the nuclear surface,  $B_p = 0$ . The production of daughter species is more complicated. Consider a daughter species  $d$  derived from parent molecule  $p$ . Suppose one parent possesses velocity  $\mathbf{v}_1$  and internal energy  $\varepsilon_m$ , the rate at which this molecule is destroyed is  $1/\tau_p$ . Following its photodestruction, two or more daughter products are created. There is a probability that one of the daughter product belongs to species  $s$  with internal energy  $\varepsilon_k$  and velocity  $\mathbf{v}$ . If  $P_{ps}(\mathbf{v}, \varepsilon_k; \mathbf{v}_1, \varepsilon_m) = P_{ps}(\Gamma; \Gamma_1)$  is this probability, the rate change due to production of species  $s$  is

$$\begin{aligned} B_s(\mathbf{r}, \mathbf{v}, \varepsilon_k, t) &= \sum_p \int \frac{P_{ps}(\Gamma; \Gamma_1) f_p(\mathbf{r}, \Gamma_1, t)}{\tau_p} d\Gamma_1 \quad \text{for } s = \text{daughter} \\ &= 0 \quad \text{if } s = \text{parent} \end{aligned} \quad (2.25)$$

### 2.3.3. Radiative processes

The absorption or emission of photons changes the internal energy state  $\epsilon_k$ , thus affecting the number of molecules in  $(dr, dv, \epsilon_k)$ . We denote  $P_{kj}^s$  as the radiative transition rate of species  $s$  from energy state  $k$  to energy state  $j$  due to solar radiation. This rate is evaluated with Einstein's coefficients as

$$P_{kj}^s = B_{kj}^s J_{kj}(\nu) + A_{kj}^s, \quad (2.26)$$

where  $A_{kj}^s$  are the spontaneous emission rate of species  $s$  from state  $k$  to state  $j$  and  $B_{kj}^s$  is the induced emission or absorption rate from state  $k$  to state  $j$ .  $J_{kj}(\nu)$  is the solar radiation intensity at frequency  $\nu$ . Conservation of momentum requires that a velocity component be added to the center of mass of the molecule after absorption or radiation occurs. It is usually the case that molecular absorption is in the IR spectral region, so this extra velocity is very small and can be neglected. The flux of molecules given by radiative rate of change  $R$  per unit phase volume per unit time is

$$R_s(r, \nu, \epsilon_k, t) = \sum_j \left[ P_{jk}^s f_s(r, \nu, \epsilon_j, t) - P_{kj}^s f_s(r, \nu, \epsilon_k, t) \right]. \quad (2.27)$$

### 2.3.4. Change due to collisions

We distinguish between two types of collisions. For those between molecules of the same species  $s$  we define  $J_s(f_s)drdvdt$  as the net number of molecules of species  $s$  flowing into the volume element  $(r, v, \epsilon_k)$  during time interval  $(t, t+dt)$ . For

collisions with molecules of other species  $j$  ( $j \neq s$ ) we define  $J_{sj}(f_s, f_j)d\mathbf{r}d\mathbf{v}d\mathbf{t}$  as the net number flowing into the volume element. Bird (1976) showed that  $J_s$  is

$$J_s(f_s) = \int d\Omega^* \int (f_s^* f_{sI}^* - f_s f_{sI}) \sigma v_{rel} d\Gamma_1, \quad (2.28)$$

where  $\sigma$  is the cross-section of the collision and  $\Omega$  is the spatial angle. We generalize the above equation to find  $J_{sj}$  :

$$J_{sj}(f_s f_j) = \int d\Omega^* \int (f_j^* f_s^* - f_j f_s) \sigma(\Gamma_s^*, \Gamma_j^*; \Gamma_s, \Gamma_j) v_{rel} d\Gamma_j. \quad (2.29)$$

### 2.3.5. Cometary Boltzmann equation

We have derived the individual changes to the distribution function due to each different physical process in the coma. Upon substituting all rate change terms from Eqs. 2.21 and 2.23-2.29 into the mass conservation Eq. 2.22 and rearranging terms, we obtain the *cometary Boltzmann equation*

$$\frac{\partial f_s}{\partial t} + \mathbf{v} \cdot \frac{\partial f_s}{\partial \mathbf{r}} + \frac{\mathbf{F}}{m} \cdot \frac{\partial f_s}{\partial \mathbf{v}} = B_s - D_s + R_s + J_s(f_s) + \sum_{j \neq s} J_{sj}(f_s f_j), \quad (2.30)$$

$$s, j = H_2O, OH, H, O, H_2, \dots$$

The only physical boundary of a cometary coma is the nuclear surface. On the assumption that LTE applies to gas molecules near the nuclear surface. The hemispherical Maxwell-Boltzmann distribution provides the boundary condition

$$\begin{aligned}
f_s(\mathbf{r}, \mathbf{v}, \mathbf{e}_k, t) &= 0, \quad \text{if } s = \text{radical and} \\
f_s(\mathbf{r}, \mathbf{v}, \mathbf{e}_k, t) &= n_s \left( \frac{2k_B T_s}{m_s} \right)^{\frac{3}{2}} \exp\left( -\frac{m_s}{2k_B T_s} v^2 \right) \frac{e^{-\mathbf{e}_k \cdot \mathbf{v} / (k_B T_s)}}{\sum_k e^{-\mathbf{e}_k \cdot \mathbf{v} / (k_B T_s)}}, \quad (2.31) \\
&\quad \text{if } s = \text{parent, } \mathbf{v} \cdot \mathbf{e}_r \geq 0,
\end{aligned}$$

where  $\mathbf{e}_r$  is a unit vector normal to the nuclear surface.

The cometary Boltzmann equation is actually a set of integral-differential equations in phase space. If initial and boundary values are known, in principle the distribution function  $f$  can be calculated.

#### 2.4. Direct Solutions of the Boltzmann Equation

The cometary Boltzmann equation contains differentiation over spatial and velocity domains and integration terms due to collisions. As a result, the actual solutions of the cometary Boltzmann equation for specific problems are far from trivial and is beyond the scope of this thesis. In principle, however, direct solutions of the cometary Boltzmann equation are possible. The general approach to obtaining numerical solutions is illustrated below. We rewrite the cometary Boltzmann equation as

$$\frac{\partial f}{\partial t} = -\hat{D}f + \hat{O}f + \hat{C}f \quad (2.32)$$

where  $f$  is the functional matrix  $\{f_i\}$ ,  $\hat{C}$  is the nonlinear collision operator,  $\hat{O}$  is a linear operator for production, destruction, and radiative processes, and  $\hat{D} = \mathbf{v} \cdot \partial / \partial \mathbf{r} + \mathbf{F} / m \cdot \partial / \partial \mathbf{v}$ . Assuming that the initial  $f(\mathbf{r}, \Gamma, 0)$  is known, the solution  $f(\mathbf{r}, \Gamma, \Delta t)$  could be calculated from Eq. 2.32 directly:

$$f(\mathbf{r}, \Gamma, \Delta t) = (1 - \Delta t \hat{D} + \Delta t \hat{O} + \Delta t \hat{C}) f(\mathbf{r}, \Gamma, 0). \quad (2.33)$$

By advancing the time step  $\Delta t$  in Eq. 2.33,  $f(\mathbf{r}, \Gamma, t)$  is found for all  $t$ .

Several numerical methods have been applied successfully for many years to solve the Boltzmann equation in simpler gas dynamic environments. Bird (1976) introduced the direct simulation Monte Carlo (DSMC) technique for the Boltzmann equation of a single gas without internal freedom. This method has been developed to an impressive level by Bird and others (see, *e.g.*, Bird 1976). In the DSMC method a large number of simulated molecules are followed simultaneously. Starting from a certain initial distribution, the method traces the movement of large numbers of molecules step by step in time. Other techniques have also been developed to solve the single species Boltzmann equation (see, *e.g.*, Muntz 1989 and references therein). However, the DSMC method is probably the most promising way to solve the cometary Boltzmann equation.

In many cases only the steady state solution is of interest. The stationary state solution for a cometary coma can be calculated by the time-step method of Eq. 2.33 because it is a special case of the general time-dependent solution. If the boundary conditions remain constant, sooner or later  $f(\mathbf{r}, \Gamma, t)$  converges to some stationary value.

In other words, time  $t_0$  could be found such that for any later time  $t$  the solution  $f(\mathbf{r}, \mathbf{v}, t)$  remains virtually the same as  $f(\mathbf{r}, \mathbf{v}, t_0)$ . There are, of course, more efficient methods to solve the stationary state cometary Boltzmann equation. For example, if external forces can be neglected and  $\partial f/\partial t=0$ , the cometary Boltzmann equation (Eq. 2.30) becomes

$$\mathbf{v} \cdot \frac{\partial f}{\partial \mathbf{r}} = \hat{O}f + \hat{C}f. \quad (2.34)$$

An iterative solution of Eq. 2.34 can be found if we rewrite it as

$$\mathbf{v} \cdot \frac{\partial f^{(i)}}{\partial \mathbf{r}} = \hat{O}f^{(i-1)} + \hat{C}f^{(i-1)}. \quad (2.35)$$

Now the collision operator acts only on  $f^{(i-1)}$  and new  $f^{(i)}$  could be obtained by integrating spatially from Eq. 2.35.

### CHAPTER 3

#### RELATIONSHIP OF THE COMETARY BOLTZMANN EQUATION TO OTHER GAS MODELS

In Chapter 2 we presented a dilute gas model and showed that the full description of a neutral coma requires the specification of one independent variable (the distribution function  $f$ ) in an eight-dimensional (8-D) space that includes: (a) the spatial coordinates (3-D), (b) the velocity space (3-D), (c) the internal energy state (1-D, discrete), and (d) the time. Subsequently, we derived the cometary Boltzmann equation and showed that its direct solution is possible. Unfortunately, the large number of independent variables and the complexity of collision integrals make the direct solution of the cometary Boltzmann equation not very efficient. However, the computational feasibility is not the major concern in this thesis. We introduce the dilute gas model because of its generality in representing physical principles and its applicability over the whole coma. With continuing advances in computer technology, and the possible introduction of efficient new algorithms, the numerical solutions of the cometary Boltzmann equation will be less a problem in the future than it is today. For this reason we defer direct solutions of cometary Boltzmann equation or the formulation of numerical algorithms to future studies and we turn our attention to other applications of the dilute gas model instead.

In order to make use of the cometary Boltzmann equation at this stage we could introduce certain simplifying assumptions. First, we may reduce the number of

independent variables. For example, the steady state assumption reduces the total number of independent variables to 7 and the assumption of spherically symmetric outflow reduces the number of spatial coordinates to 1. Second, even if an independent variable cannot be entirely eliminated, we could limit its scope. Thus it is natural to limit the discussion of internal energy states to only a few prominent ones and to neglect those that are rarely populated. Third, we may impose additional conditions in order to reduce the complexity of the collision integrals on the right side of cometary Boltzmann equation. An extreme example illustrated by early coma studies is to assume that the gas outflow is collisionless, thus eliminating the need to calculate collision integrals entirely. In general, these additional assumptions make the cometary Boltzmann equation more manageable but, unfortunately, they also limit its generality and reduce its applicability.

In this chapter we focus our discussions on the relationship of previous models with our dilute gas model. We show that the cometary Boltzmann equation can be used as a theoretical basis upon which other models can be derived. We draw road maps (*e.g.*, Fig. 3.1) that lead readers from the cometary Boltzmann equation to their favorite models and describe the simplifications or assumptions that were made along the way. In §3.1 we introduce a cometary transport equation and establish some preliminary mathematical results. These results are then used to derive the Haser model in §3.2 and the hydrodynamic models in §3.4. In §3.3 we show that molecular excitation models are simplified forms of the cometary Boltzmann equation and in §3.5 we present the relationship of Monte Carlo particle trajectory methods to the cometary Boltzmann

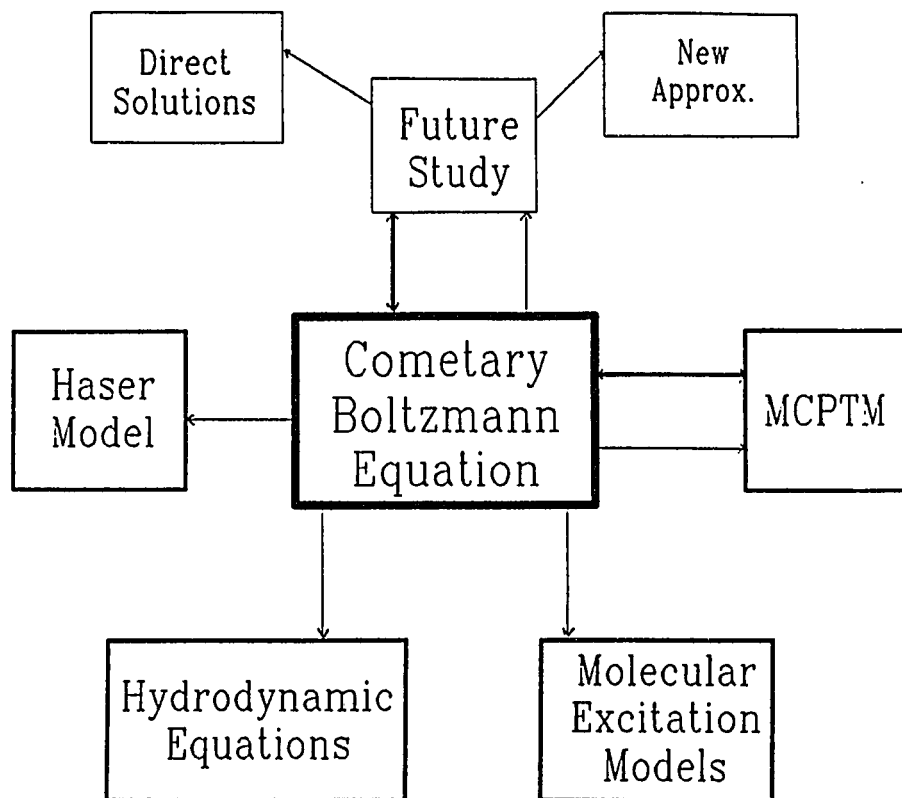


**Figure 3.1.** The central relationship of the cometary Boltzmann equation to gas dynamic models of the coma.

equation.

### 3.1. The Cometary Transport Equation

The cometary transport equation is the first mathematical result of the cometary Boltzmann equation and concerns the conservation of physical quantities. Assuming that a physical quantity  $Q_s$  is associated with a single molecule by function  $Q_s(\Gamma)$ , we multiply both sides of the cometary Boltzmann equation by  $Q_s$ :

$$Q_s \frac{\partial f_s}{\partial t} + Q_s v \cdot \frac{\partial f_s}{\partial r} + Q_s \frac{F}{m} \cdot \frac{\partial f_s}{\partial v} = Q_s \cdot B_s - Q_s \cdot D_s + Q_s \cdot R_s + Q_s \cdot J_s(f_s) + Q_s \cdot \sum_{j \neq s} J_{sj}. \quad (3.1)$$

We integrate Eq. 3.1 over  $\Gamma$  to obtain the conservation equation for  $\langle Q_s \rangle$ . With standard algebraic manipulation (see, *e.g.*, Bird 1976) on the left side of the equation, we obtain the *cometary transport equation* for  $Q_s$ :

$$\frac{\partial}{\partial t} (n_s \langle Q_s \rangle) + \nabla \cdot (n_s \langle Q_s v \rangle) - n_s \frac{F}{m} \cdot \left\langle \frac{\partial Q_s}{\partial v} \right\rangle = \Delta [B_s Q_s] - \Delta [D_s Q_s] + \Delta [R_s Q_s] + \Delta [J_s Q_s] + \sum_{j \neq s} \Delta [J_{sj} Q_s], \quad (3.2)$$

where  $n_s$  is the spatial number density,  $\langle Q_s \rangle$ ,  $\langle Q_s \mathbf{v} \rangle$ , *etc.* are average values. The notation  $\Delta[P]$  denotes the integration of  $P$  over velocity and energy space  $\Gamma = (\mathbf{r}, \epsilon)$  and is defined by

$$\Delta[P](\mathbf{r}, t) = \int P(\mathbf{r}, \Gamma, t) d\Gamma = \sum_k \int P(\mathbf{r}, \mathbf{v}, \epsilon_k, t) d\mathbf{v}. \quad (3.3)$$

For convenience, we refer to  $\Delta[P]$  as the *phase integration* of  $P$ . The cometary transport equation is a direct result of the cometary Boltzmann equation and is very important in the derivation of conservation equations for mass, momentum, and energy.

The phase integration of a physical quantity  $P(\mathbf{r}, \Gamma, t)$  maps  $P$  from the generalized phase space  $(\mathbf{r}, \Gamma)$  to the spatial domain  $(\mathbf{r})$ . Although considerable information is lost in the process, the resulting function  $\Delta[P]$  is much simpler to deal with. For this reason the cometary transport equation provides ways to simplify the cometary Boltzmann equation.

The phase integration of the rate changes defined in §2.3 are particularly simple. For example, upon integrating both sides of Eq. 2.27 we obtain the phase integration of the radiative rate  $R_s$ :

$$\Delta[R_s] = 0. \quad (3.4)$$

This result is easy to understand. Since  $R_s$  (molecules/unit phase space/sec) is the rate of change in phase space due to radiative processes, and radiative excitation or de-excitation changes only the internal energy states, not the total number of molecules in

spatial space, the integration of  $R_s$  over phase space (molecules  $\text{cm}^{-3} \text{sec}^{-1}$ ) is zero.

Similarly we perform phase integration for destruction and production terms. Integrating both sides of Eq. 2.24 over  $\Gamma$ , we obtain the phase integration of the destruction rate:

$$\Delta[D_s] = \int \frac{f_s}{\tau_s} d\Gamma = \frac{n_s}{\tau_s}. \quad (3.5)$$

Integrating Eq. 2.25 over  $\Gamma$  we have

$$\begin{aligned} \Delta[B_s] &= 0, \quad \text{for parent species } (s = p), \text{ and} \\ &= BR_p^d \cdot \frac{n_p}{\tau_p} \quad \text{for daughter species } (s = d), \end{aligned} \quad (3.6)$$

where  $BR_p^d$  is the branching ratio from parent  $p$  to daughter  $d$  and is given by

$$BR_p^d = \frac{1}{n_p} \int d\Gamma \int d\Gamma' P_{pd}(\Gamma; \Gamma') f_p(\mathbf{r}, \Gamma', t). \quad (3.7)$$

Since collisions do not change the total number of molecules, phase integration of the collision terms is zero. That is

$$\Delta[J_s] = 0, \quad \text{and} \quad \Delta[J_{sj}] = 0. \quad (3.8)$$

Equation 3.8 can be proved using the symmetry properties of the collision terms (see Bird 1976).

With the help of the cometary transport equation and the phase integrations, we now discuss previous coma models.

### 3.2. The Haser Formula and the Cometary Boltzmann Equation

The Haser or monokinetic model predicts the number density distributions of molecules by assuming isotropic, steady state outflow at uniform velocity with no collisions. These four assumptions are usually called the *Haser hypotheses* (Festou 1981). From these assumptions Haser (1957) derived the density distributions of parent and daughter species. The derivation of parent density distributions from the Haser hypotheses is fairly easy. For parent molecules  $p$  released from the surface of the nucleus at the evaporation rate  $E_p$  (molecules  $\text{cm}^{-2} \text{sec}^{-1}$ ), the total production rate  $Q_p$  (molecules  $\text{sec}^{-1}$ ) is

$$Q_p = 4\pi r_n^2 E_p \quad (3.9)$$

where  $r_n$  is the radius of the nucleus. If all molecules expand isotropically with the same velocity  $u_p$ , the density distribution is

$$n_p(r) = \frac{Q_p}{4\pi u_p r^2}. \quad (3.10)$$

Since parent molecules have finite lifetime  $\tau_p$  due to photodestruction by solar radiation, equation 3.10 should be modified by an exponential factor to adjust for losses:

$$n_p(r) = \frac{Q_p}{4\pi u_p r^2} e^{-\frac{r}{u_p \tau_p}}. \quad (3.11)$$

This is the Haser formula for parent molecules. Derivation of the number density distribution for daughter molecules is slightly more difficult. Assuming that daughter products flow radially outward with constant velocity  $u_d$ , Haser (1957) obtained

$$n_d(r) = \frac{Q_p}{4\pi u_d r^2} \frac{l_d}{l_d - l_p} \left[ \exp\left(-\frac{r}{l_p}\right) - \exp\left(-\frac{r}{l_d}\right) \right], \quad (3.12)$$

where  $l_p = u_p \tau_p$  and  $l_d = u_d \tau_d$  are scale-lengths and subscript  $d$  denotes daughter species. This equation is also called the Haser's *two-stage model* since it involves two scale-lengths. The Haser formulae (Eqs. 3.11-3.12) were important to the development of cometary models and are quoted widely in the literature. Even after the introduction of other models (*e.g.*, the hydrodynamic and Monte Carlo methods), the Haser formulae dominate data analyses. For example, following the last apparition of comet Halley, most analyses of coma gas observations involved use of the Haser formulae in one way or another.

We demonstrate here that Haser's formulae can also be derived from the

cometary transport equation upon applying Haser's hypotheses. We apply the four basic assumptions to the cometary Boltzmann equation. The steady state assumption eliminates the time-dependent term. The assumption of isotropic outflow with a single velocity means  $\mathbf{v} = u_s \mathbf{e}_r$ , where  $u_s$  is constant and  $\mathbf{e}_r$  is a radial unit vector. The external force  $\mathbf{F}$  must be zero to ensure constant velocity of the molecules. Finally, the assumption of no collisions reduces the collision terms on the right side of Eq. 3.2 to zero. Rewriting Eq. 3.2 in spherical coordinates with the origin at the nuclear center, we obtain

$$\frac{u_s}{r^2} \cdot \frac{d}{dr} (r^2 n_s \langle Q_s \rangle) = \Delta[B_s Q_s] - \Delta[D_s Q_s] + \Delta[R_s Q_s]. \quad (3.13)$$

For parent molecules ( $s = p$ ) and  $Q_s = 1$ ,  $\Delta[R_p] = \Delta[B_p] = 0$  and  $\Delta[D_p] = n_p / \tau_p$ . Equation 3.13 reduces to

$$\frac{u_p}{r^2} \frac{d}{dr} (r^2 n_p) = -\frac{n_p}{\tau_p}. \quad (3.14)$$

A boundary condition is obtained from the assumptions that the total production rate is  $Q_p$  and the outflow is isotropic:

$$4\pi u_p n_p r^2 |_{r=r_n} = Q_p. \quad (3.15)$$

Substituting  $X = n_p r^2$  and  $l_p = u_p \tau_p$ , Eq. 3.14 becomes

$$\frac{1}{X} \frac{dX}{dr} = -\frac{1}{l_p}. \quad (3.16)$$

Upon integrating Eq. 3.16 from  $r_n$  to  $r$ , we obtain the general solution

$$X = X(r_n) e^{-\frac{r-r_n}{l_p}}. \quad (3.17)$$

That is,

$$n_p(r) = n_p(r_n) \left( \frac{r_n}{r} \right)^2 \exp\left( -\frac{r-r_n}{l_p} \right). \quad (3.18)$$

After substituting the boundary condition in Eq. 3.15 into Eq. 3.18, we obtain

$$n_p(r) = \frac{Q_p}{4\pi u_p r^2} \exp\left( -\frac{r-r_n}{u_p \tau_p} \right). \quad (3.19)$$

Since  $r_n \ll l_p = u_p \tau_p$ , equation 3.19 is essentially the same as the Haser formula for a parent species (Eq. 3.11).

We apply the same procedure to daughter products ( $s = d$ ). The production rate  $\Delta[B_d] = BR_p^d (n_p / \tau_p)$ , where  $BR_p^d$  is the branching ratio. The destruction rate  $\Delta[D_d] =$

$n_d/\tau_d$ . When  $Q_s = 1$  Eq. 3.15 becomes

$$\frac{n_d}{r^2} \frac{d}{dr} (r^2 n_d) = BR_p^d \frac{n_p}{\tau_p} - \frac{n_d}{\tau_d} \quad (3.20)$$

with the boundary condition

$$n_d(r)|_{r=r_n} = 0. \quad (3.21)$$

Substituting Eq. 3.19 into Eq. 3.20 and solving for the boundary condition in Eq. 3.21, we obtain

$$n_d = \frac{Q_p}{4\pi u_d r^2} \frac{l_d}{l_d - l_p^d} \left[ \exp\left(-\frac{r-r_n}{l_p}\right) - \exp\left(-\frac{r-r_n}{l_d}\right) \right], \quad (3.22)$$

where  $l_d = u_d \tau_d$  and  $l_p^d = u_p \tau_p / BR_p^d$ . Equation 3.22 is equivalent to Haser's two-stage model (Eq. 3.12) if we assume  $BR_p^d = 1$ . Thus we have derived Haser's formulae for the number densities of parent and daughter species directly from the cometary Boltzmann equation. To express it more explicitly, *the Haser formulae are solutions to the cometary Boltzmann equation for the traditional Haser model assumptions* (see Fig. 3.2).

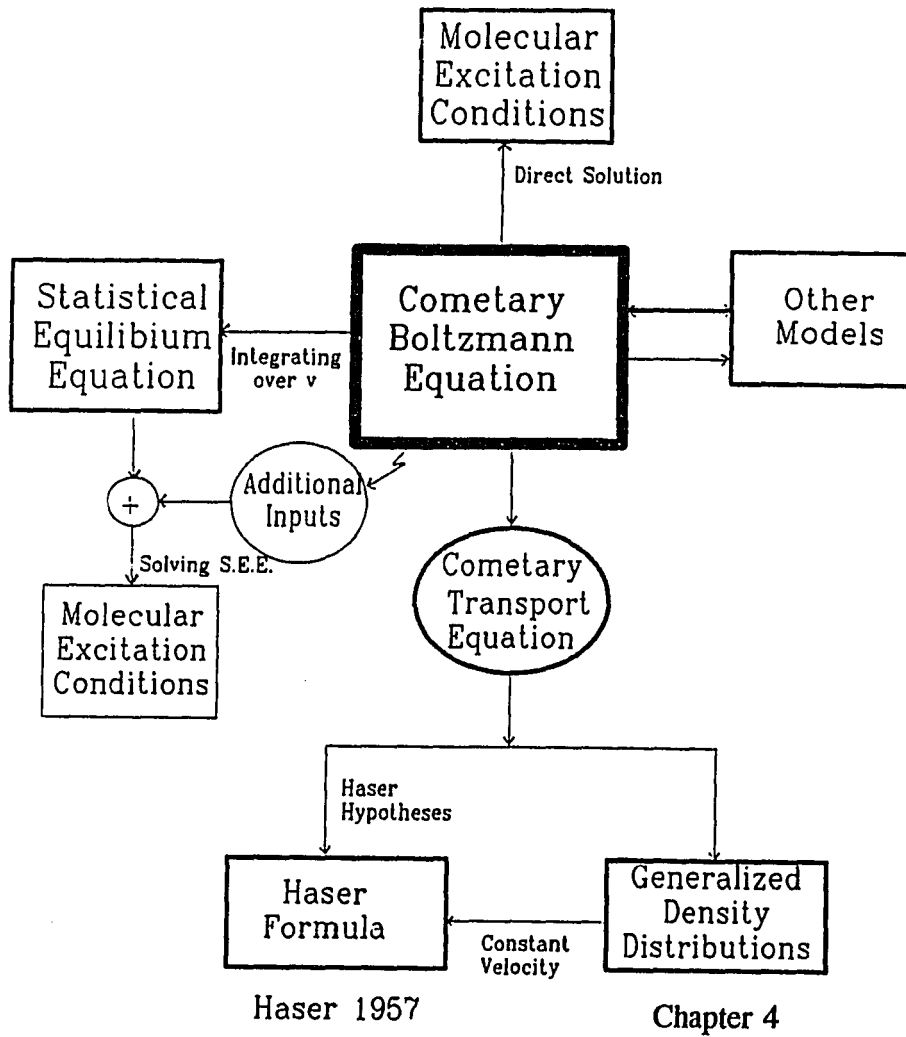


**Figure 3.2.** Relationships between the cometary Boltzmann equation, the Haser model, and molecular excitation models. The Haser formula for number density may be derived from the cometary transport equation for the Haser model assumptions of collisionless, isotropic outflow at constant velocity.

### 3.3. Molecular Excitation Conditions and the Cometary Boltzmann Equation

Figure 3.2 also demonstrates the relationship of the cometary Boltzmann equation to molecular excitation models. These models are used to study excitation conditions in the coma by calculating the relative populations of energy levels of molecules. If a direct solution of the cometary Boltzmann equation can be found, we need only integrate the resulting distribution function  $f_s(\mathbf{r}, \mathbf{v}, \epsilon_k, t)$  over velocity space  $\mathbf{v}$  to find the relative population of energy level  $k$ . *Therefore, molecular excitation models are actually simplified forms of our Boltzmann equation* (Fig. 3.2).

Molecular excitation models have been developed for CO (Chin and Weaver 1984), linear molecules such as HCN (Crovisier 1987), and more complicated molecules such as H<sub>2</sub>O (Bockelée-Morvan 1987) and H<sub>2</sub>CO (Reuter *et al.* 1989). These models use instead the statistical equilibrium equation to determine the relative populations of energy levels. For species  $s$  the relative population  $n_s^i$  of energy level  $i$  satisfies

$$\frac{dn_s^i}{dt} = \left[ -\sum_{j,k} n_s^i C_{sj}^{ik} + \sum_{j,k} n_s^k C_{sj}^{ki} \right] + \left[ -\sum_k n_s^i P_s^{ik} + \sum_k n_s^k P_s^{ki} \right]. \quad (3.23)$$

The first bracket on the right side includes collisions terms, where  $C_{sj}^{ik}$  is the collisional excitation rate (sec<sup>-1</sup>) of species  $s$  from energy state  $i$  to state  $k$  by species  $j$ . The second bracketed terms represent radiative transitions that include both radiative excitation and spontaneous decay.  $P_s^{ik}$  is the transition rate (sec<sup>-1</sup>) of species  $s$  from energy state  $i$  to  $k$ . This equation is usually coupled with density and temperature output from other

models and is solved numerically to obtain the relative populations. It is readily demonstrated that Eq. 3.17 is derived from the cometary Boltzmann equation by integrating both sides of Eq. 2.30 over velocity space  $\mathbf{v}$  (Fig. 3.2), the collision terms of the cometary Boltzmann equation generate the first bracket and radiative terms create the second bracket.

### 3.4. Hydrodynamic Equations and the Cometary Boltzmann Equation

In this section we demonstrate that the cometary hydrodynamic equations are also special cases of the cometary Boltzmann equation under the assumption of LTE. The derivation follows that in Bird (1976) or Lifshitz and Pitaevskii (1981). For simplicity, we consider the case of a single gas coma so that the terms  $J_{sj}(f_s f_j)$  and the subscript  $s$  in Eq. 2.30 may be ignored. A multi-species hydrodynamic model can be derived similarly from the cometary Boltzmann equation by including the collision terms  $J_{sj}$ .

#### 3.4.1. Derivation of the hydrodynamic equations of the coma

Intermolecular collisions of the same species do not alter either the number of colliding particles or their total energy and momentum. It is therefore clear that the collision part of the change satisfies the condition (Lifshitz and Pitaevskii, 1981)

$$\Delta[J_s] = 0, \quad \Delta[\varepsilon J_s] = 0, \quad \text{and} \quad \Delta[mvJ_s] = 0, \quad (3.24)$$

where  $\varepsilon = \frac{1}{2} mv^2 + \varepsilon_{int}$  is the total energy of a molecule. In addition, the following relations follow directly from Eq. 2.27:

$$\Delta[R_s] = 0 \quad \text{and} \quad \Delta[R_s \mathbf{v}] = 0. \quad (3.25)$$

The hydrodynamic equations are derived below from the cometary transport equation (Eq. 3.2) using Eqs. 3.24-3.25.

(1). *Mass conservation equation.* Substituting  $Q = m$  into the cometary transport equation and utilizing relations such as  $\langle \mathbf{v} \rangle = \mathbf{u}$ ,  $\Delta[J] = 0$  and  $\Delta[R] = 0$ , we obtain

$$\frac{\partial \rho}{\partial t} + \nabla \cdot (\rho \mathbf{u}) = -\frac{\rho}{\tau}, \quad (3.26)$$

where  $\rho = nm$  is the mass density of the species.

(2). *Momentum conservation equation.* Substituting  $Q = m\mathbf{v}$  into the cometary transport equation, we have

$$\frac{\partial \rho \mathbf{u}}{\partial t} + \nabla \cdot (\rho \langle \mathbf{v} \mathbf{v} \rangle) - \frac{\rho \mathbf{F}}{m} = -\frac{\rho \mathbf{u}}{\tau}. \quad (3.27)$$

Noting that  $\rho \langle \mathbf{v} \mathbf{v} \rangle = \rho \langle (\mathbf{u} + \mathbf{v}')(\mathbf{u} + \mathbf{v}') \rangle = \rho \mathbf{u} \mathbf{u} + \rho \langle \mathbf{v}' \mathbf{v}' \rangle = \rho \mathbf{u} \mathbf{u} + p \underline{\underline{I}} + \underline{\underline{\mu}}$ , where  $p$  is the scalar pressure (Eq. 2.17) and  $\underline{\underline{\mu}}$  is the viscous stress tensor (Eq. 2.19), we obtain the momentum conservation equation

$$\frac{\partial \rho \mathbf{u}}{\partial t} + \nabla \cdot (\rho \mathbf{u} \mathbf{u}) = -\nabla \cdot p + \nabla \cdot \underline{\underline{\mu}} + \rho \frac{\mathbf{F}}{m} - \frac{\rho \mathbf{u}}{\tau}. \quad (3.28)$$

(3). *Energy conservation equation.* Substituting  $Q = \varepsilon = \frac{1}{2}m\mathbf{v}^2 + \varepsilon_{int}$  into the cometary transport equation, we have

$$\frac{\partial}{\partial t}(n\langle\varepsilon\rangle) + \nabla \cdot (n\langle\varepsilon\mathbf{v}\rangle) - n\mathbf{u} \cdot \mathbf{F} = -\frac{n\langle\varepsilon\rangle}{\tau} + \Delta[Re]. \quad (3.29)$$

$\langle\varepsilon\rangle$  is given by Eq. 2.11 and  $\langle\varepsilon\mathbf{v}\rangle = \langle\varepsilon\rangle\mathbf{u} + \langle\varepsilon\mathbf{v}'\rangle$ .  $\langle\varepsilon\mathbf{v}'\rangle$  is calculated from

$$\begin{aligned} \langle\varepsilon\mathbf{v}'\rangle &= \left\langle \left( \frac{1}{2}m(\mathbf{u}+\mathbf{v}')^2 + \varepsilon_{int} \right) \mathbf{v}' \right\rangle \\ &= \left\langle \left( \frac{1}{2}m(\mathbf{v}')^2 + \varepsilon_{int} \right) \mathbf{v}' \right\rangle + \mathbf{u} \langle m\mathbf{v}'\mathbf{v}' \rangle. \end{aligned} \quad (3.30)$$

The first term on the right side of Eq. 3.30 is the thermal flux  $\mathbf{q}$  (Eq. 2.14) while  $\langle m\mathbf{v}'\mathbf{v}' \rangle =$  stress tensor  $\underline{P} =$  viscous tensor  $\underline{\mu} + p\underline{I}$  (Eqs. 2.16 and 2.19). In other words,

$$\langle\varepsilon\mathbf{v}\rangle = \langle\varepsilon\rangle\mathbf{u} + \mathbf{q} + \mathbf{u} \cdot \underline{\mu} + p \cdot \mathbf{u}. \quad (3.31)$$

Substituting Eq. 3.31 into Eq. 3.29 we obtain

$$\begin{aligned} \frac{\partial}{\partial t} n \langle \epsilon \rangle + \nabla \cdot (n \mathbf{u} \langle \epsilon \rangle + \mathbf{q} + p \mathbf{u}) = \\ n \mathbf{u} \cdot \mathbf{F} + \nabla \cdot (\underline{\underline{\mu}} \cdot \mathbf{u}) - \frac{n \langle \epsilon \rangle}{\tau} + \Delta [R \epsilon]. \end{aligned} \quad (3.32)$$

Eq. 3.32 is rewritten using the mass and momentum conservation equations:

$$n \frac{\partial}{\partial t} \langle \epsilon \rangle + n \mathbf{u} \cdot \nabla \langle \epsilon \rangle = -p \nabla \cdot \mathbf{u} + \underline{\underline{\mu}} \cdot \nabla \mathbf{u} - \nabla \cdot \mathbf{q} + \Delta [R \epsilon], \quad (3.33)$$

where  $\langle \epsilon \rangle = \frac{1}{2} m u^2 + \frac{1}{2} 3 k_B T + \langle \epsilon_{int} \rangle$  (Eq. 2.11) and  $\Delta [R \epsilon]$  is the rate of energy transfer ( $\text{erg cm}^{-3} \text{ sec}^{-1}$ ) due to radiative processes. Multi-species hydrodynamic equations can be derived from the cometary transport equation by similar procedures. The resulting equations are essentially similar to that for a single species, but momentum and energy transfer terms are added to the momentum and energy conservation equations, respectively, in order to take into account inter-species interactions.

So far we have derived one mass conservation equation, three momentum conservation equations, one energy equation and the perfect gas equation  $p = n k_B T$  for a total of 6 equations. Among the unknowns are six thermodynamic properties: pressure  $p$ , temperature  $T$ , density  $n$ , outflow velocity  $\mathbf{u}$  (3 components), internal energy  $\langle \epsilon_{int} \rangle$ , energy transfer rate  $\Delta [R \epsilon]$ , thermal flux  $\mathbf{q}$  and the viscous tensor  $\underline{\underline{\mu}}$ . The

available equations therefore do not constitute a determinate set, so additional relationships or assumptions must be introduced. The most frequently used assumption is that inter-molecular collisions occur frequently such that all particles at any spatial point remain in *LTE*. Under this assumption the internal energy  $\varepsilon_{int}$  becomes a function of temperature  $T$  and may be calculated from the classical Boltzmann energy distribution. The radiative heating (or cooling) is calculated from the Einstein coefficients. This leaves the heat flux  $\mathbf{q}$  and the viscous tensor  $\underline{\underline{\mu}}$  as extra variables.

### 3.4.2. Euler equations

In the Euler formulation, the heat flux  $\mathbf{q}$  and the viscous tensor  $\underline{\underline{\mu}}$  are assumed to be zero. This leads to six equations with six variables ( $p, T, n, \mathbf{u}$ ). This determinate set of equations is usually called the *Euler equations* of inviscid flow.

### 3.4.3. Navier-Stokes equations

In the Navier-Stokes formulation the heat flux  $\mathbf{q}$  and the viscous tensor  $\underline{\underline{\mu}}$  are represented by simplified expressions containing the thermodynamic parameters ( $p, T, n, \mathbf{u}$ ). The heat flux is

$$\mathbf{q} = -\kappa\nabla T, \quad (3.34)$$

where  $\kappa$  is the coefficient of thermal conductivity and is a function of temperature  $T$ .

The viscous stress tensor  $\underline{\underline{\mu}}$  is (Landau and Lifshitz 1959)

$$\underline{\underline{\mu}} = \mu_s \left[ \nabla \mathbf{u} + (\nabla \mathbf{u})^T - \frac{2}{3}(\nabla \cdot \mathbf{u})\mathbf{I} \right] \quad (3.35)$$

where  $\mu_s = \mu_s(T)$  is the viscosity of the fluid (a scalar),  $()^T$  is the transport operator and  $\underline{1}$  is the unit tensor. With these additional relationships we have a closed set of equations called the *Navier-Stokes equations*. Thus, *both the cometary Euler and Navier-Stokes equations are simplified forms of the cometary Boltzmann equation* (Fig. 3.3).

In a hydrodynamic model the single dependent variable of the cometary Boltzmann equation,  $f(\mathbf{r}, \mathbf{v}, \epsilon, t)$ , is replaced by a set of new variables, such as temperature, outflow velocity, pressure, *etc.*, in the spatial and time domains. The phase space (velocity + internal energy) of the cometary Boltzmann equation is eliminated by virtue of the LTE assumption. As a result, the validity of hydrodynamic models is highly dependent on LTE conditions.

The Euler equations are hyperbolic in form and describe advection and compression of the gaseous fluid. They are applicable when the properties of the fluid are highly localized by particle-particle collisions. If the mean free path  $\lambda$  over which a particle travels between collisions is no longer small, we must take into account the transport of momentum and energy through the fluid by diffusion. The Navier-Stokes equations include simplified diffusion terms. These terms smooth the momentum and temperature field in the fluid and make the hydrodynamic equations parabolic. Both  $\kappa$  and  $\mu_s$  depend on the rate at which particles experience collisions, and also on the local temperature and density of the fluid, so the transport terms may be non-linear.

The Navier-Stokes equations are not often used in coma models because cometary scientists consider the thermal conductivity and viscous terms to be

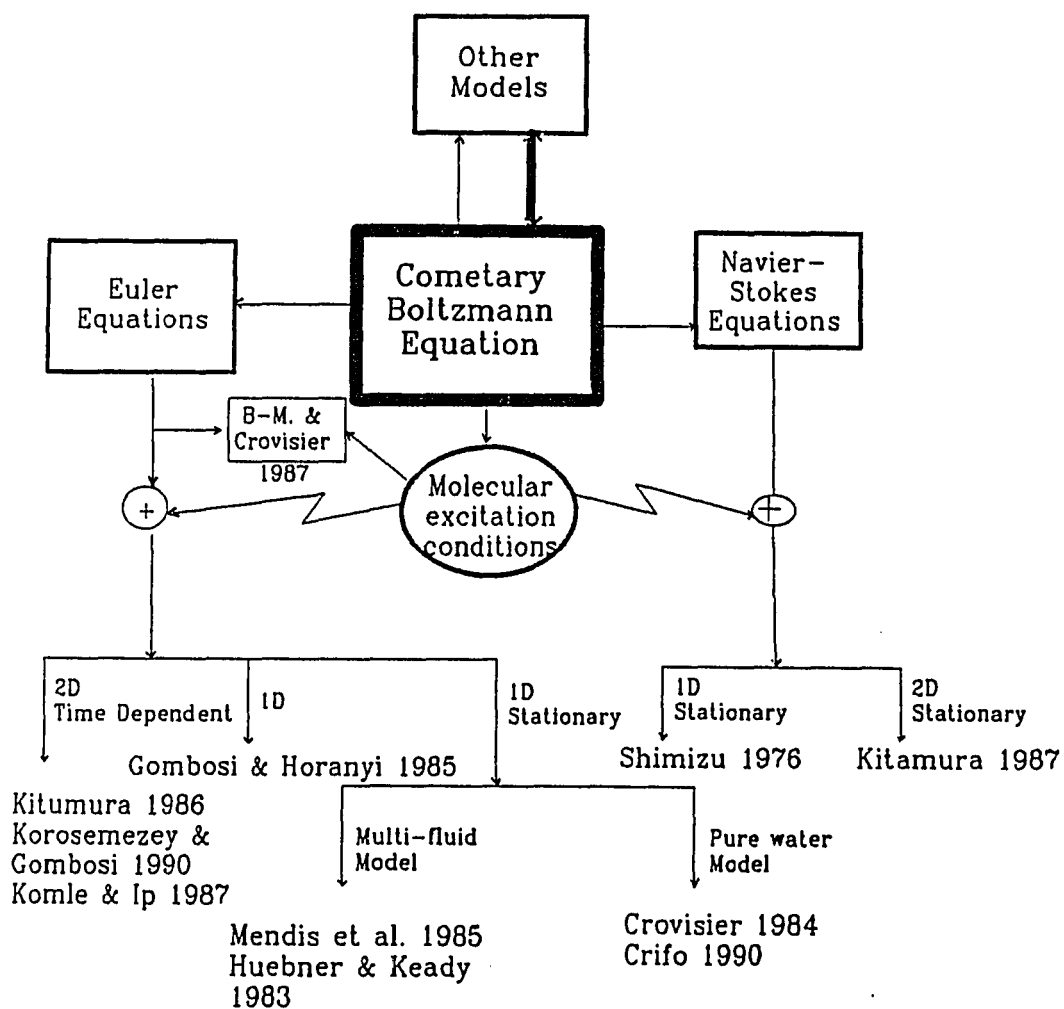


**Figure 3.3.** Relationships between the cometary Boltzmann equation and hydrodynamic models of the coma. The cometary Boltzmann equation, augmented with additional assumptions and procedures, provides a theoretical framework for deriving all current hydrodynamic models of the coma.

unimportant. Shimizu (1976) included the thermal conductivity term in his study of temperature profiles and Kitamura (1986, 1987) included both the thermal conductivity and viscous terms in his two-dimensional models. However, Kitamura's expressions for  $\kappa$  and  $\mu_b$  were considered to be incorrect by Crifo (1989) who discussed the discrepancy and gave the temperature dependence of  $\mu_s$  under cometary conditions. A more general formulation of the temperature dependence of  $\kappa$  and  $\mu_s$  was discussed by Chapman and Cowling (1970).

#### 3.4.4. Semi-LTE formulation

Detailed analyses have shown that LTE cannot be satisfied over the whole coma (see, *e.g.*, Weaver and Mumma 1984 and Bockelée-Morvan 1987 for a discussion of disequilibrium in the coma). Without LTE radiative energy transfer  $\Delta[R_\varepsilon]$  cannot be easily calculated and the Euler or Navier-Stokes equations alone do not form a determinate set. To accommodate non-LTE conditions, cometary scientists assume that molecular velocities satisfy a Maxwellian velocity distribution, but energy level populations may no longer adhere to a Boltzmann distribution. Thus semi-LTE formulation relaxes the more stringent LTE condition but it demands more calculation due to the introduction of extra dimensions in energy space. Shimizu (1976) and Crovisier (1984) both approximated non-LTE conditions in the coma by estimating the order of magnitude of non-LTE energy transfer rate. They replaced the  $\langle \varepsilon_{\text{int}} \rangle$  and  $\Delta[R_\varepsilon]$  terms in the Euler or Navier-Stokes equations with simplified semi-empirical formulae. This approach reduced the amount of computing time but is useful only when accuracy is not the primary concern. Bockelée-Morvan and Crovisier (1987b) expanded

the semi-LTE method by calculating the energy terms from molecular excitation models.

#### 3.4.5. *An overview of cometary hydrodynamic models*

A summary of current hydrodynamic models is given by Fig. 3.3. There are a large number of publications that apply hydrodynamic equations to the coma; we selected only representative models to illustrate their relationship to the cometary Boltzmann equation. The basic equations used in all these models are either Euler or Navier-Stokes hydrodynamic equations, subject to modifications for non-LTE conditions. Differences between these models include geometric considerations (one or two dimensions), time-dependency (steady state or time-variant models), the number of species included (single or multi-species), and the number of physical processes represented (radiative cooling/heating, photochemical reactions, *etc.*).

### 3.5. Monte Carlo Particle Trajectory Methods

The approach used in Monte Carlo particle trajectory methods (MCPTM) is totally different from that of a dilute gas model. The dilute gas model uses analytic expressions to represent relevant physical processes, while the MCPTM simulates the physical movement of individual molecules in order to build up a statistical solution. However, *the general cometary MCPTM is essentially a statistical method for solving the cometary Boltzmann equation* (see Fig. 3.4). This underlying relationship was first realized by Haviland (1965) for the simple, single gas Boltzmann equation. To illustrate this connection, we take the steady state case and rewrite the cometary Boltzmann equation in the following iterative form:

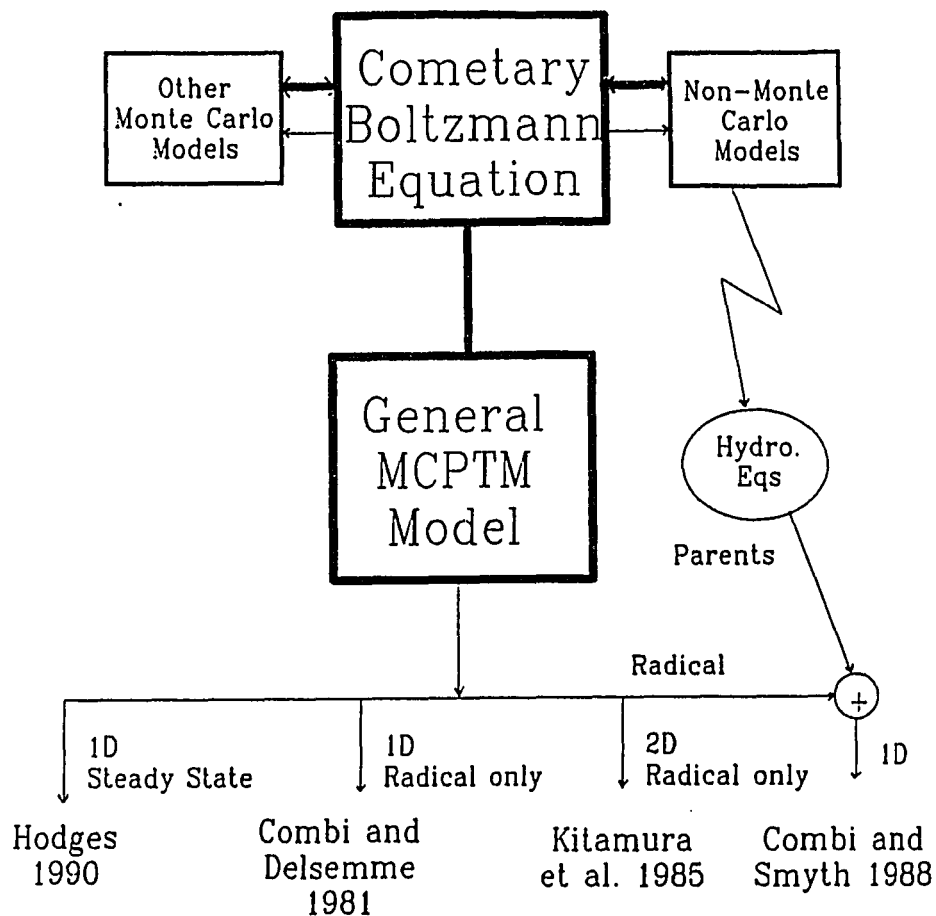


**Figure 3.4.** Relationship between the cometary Boltzmann equation and Monte Carlo particle trajectory methods (MCPTM's). All current models are considered different implementations of a general MCPTM which is a statistical procedure for solving the cometary Boltzmann equation.

$$\begin{aligned}
\mathbf{v} \cdot \frac{\partial f_s^{(i)}}{\partial \mathbf{r}} = & B_s - D_s + R_s + \sum_{j \neq s} J_{sj} (f_s^{(i)} f_j^{(i-1)}) \\
& + \iint \sigma v_{rel} d\Omega dv_l [f_s^{(i)} f_{sl}^{(i-1)} - f_s^{(i-1)} f_{sl}^{(i)}],
\end{aligned} \tag{3.36}$$

where  $f^{(i)}$  and  $f^{(i-1)}$  are the results of successive iterations.

A Monte Carlo particle trajectory model simulates each term of Eq. 3.36 by following the trajectories of large numbers of test particles in a space filled with molecules whose distribution is given by  $f^{(i-1)}$ . For example, the left side of Eq. 3.36 represents continuity in phase space and is reproduced by permitting the test particles to move in straight lines between collisions (or, if there exist external forces, test particles move according to Newtonian laws of physics). The production ( $B_s$ ) and destruction ( $D_s$ ) of parent molecules are simulated by their ejection from the nuclear surface and their subsequent photodestruction. Daughter products emerge from the photodestruction of parents and are eventually lost to photodestruction. The collision terms in Eq. 3.36 are simulated by calculating the trajectories of test particles according to collision dynamics. After following all these physical processes rigorously, the statistics are gathered and a new distribution function  $f^{(i)}$  is calculated.

### 3.5.1. A general MCPTM procedure

Up to now, all existing cometary MCPTM's (Combi and Smyth 1988, Hodges 1990) are specific implementations of Monte Carlo simulation procedures. With the

help of Eq. 3.36 we are able to outline below a general algorithm for the Monte Carlo particle trajectory methods.

*Step 1.* Initialize distribution functions  $f^{(i-1)} = \{f_s^{(i-1)}; s = \text{H}_2\text{O}, \text{OH}, \dots\}$ . It needs not be a solution of the Boltzmann equation, but it must be a valid distribution function.  $f^{(i-1)}$  represents our initial guess to the solution.

*Step 2.* Substitute  $f^{(i-1)}$  into Eq. 3.36 and solve it statistically to obtain the new distribution function  $f^{(i)}$  using the Monte Carlo sampling method outlined below:

*Step 2.1.* Generate a parent molecule (test particle) from the nuclear surface.

*Step 2.2.* Move the test particle through the space filled with gas whose distribution is  $f^{(i-1)}$ . The movement is performed in such a way that all terms in Eq. 3.36 are simulated.

*Step 2.3.* Repeat Steps 2.1 and 2.2 until a large number of test particles of species  $s$  has been traced.

*Step 2.4.* Calculate  $f_s^{(i)}$  from the trajectories of the test particles. Note that  $f_s^{(i)}$  itself may not be the solution of Eq. 3.36, but  $f_s^{(i)}$  and  $f^{(i-1)}$  satisfy the relationship of Eq. 3.36.

*Step 2.5.* Repeat steps 2.1-2.4 for all species to obtain  $f^{(i)}$ .

*Step 3.* If the solution  $f^{(i)}$  converges, *i.e.*,  $|f^{(i)} - f^{(i-1)}| < \delta$  where  $\delta$  is a pre-determined error, then  $f^{(i)}$  is a solution of the cometary Boltzmann equation. Otherwise, we assign  $f^{(i)}$  to  $f^{(i-1)}$  and go back to Step 2.

### 3.5.2. *The MCPTM for a collisionless coma*

The initial distribution function  $f^{(i-1)}$  is used only for the calculation of collisions. For collisionless outflow the collision terms on the right side of Eq. 3.36 disappear and  $f^{(i-1)}$  has no influence over the determination of  $f^{(i)}$ . Therefore, there is no need to initialize  $f^{(i-1)}$ . A new distribution function  $f^{(i)}$  found from the algorithm automatically satisfies the collisionless cometary Boltzmann equation and no iteration over index  $i$  is needed. Examples of a collisionless Monte Carlo model are Combi and Delsemme (1980) and Bockelée-Morvan and Gérard (1984).

### 3.5.3. *The time-dependent MCPTM*

The above procedure can also be applied to the time-dependent form of the cometary Boltzmann equation. If collisions are not negligible, however, for the time-dependent model  $f^{(i-1)}(\mathbf{r}, \mathbf{v}, t)$  must be stored for each time step in order to calculate  $f^{(i)}$ . This requirement may prove to be very expensive for current computers. In addition, the simulation of collision terms is very difficult when  $f^{(i-1)}$  is time-dependent. Therefore, MCPTM methods serve best either for steady state models or collisionless models.

## CHAPTER 4

### NEUTRAL GAS DENSITY DISTRIBUTIONS

#### 4.1. Introduction

In most of this chapter we limit our attention to the number density distribution of neutral molecules in cometary comae. The density distribution is probably the oldest and, until recently, the most emphasized subject in coma models. It received so much attention because the interpretation of gaseous observations requires detailed knowledge of the outflow distribution in the coma. Traditionally, the density distributions of neutral gases are given by the Haser formulae (Eqs. 3.11-3.12), which played a pivotal role in the development of cometary models and are quoted widely in the literature. However, the Haser model assumes steady state and spherically symmetric outflow at uniform velocity without collisions. These conditions are rarely applicable to a real coma. It is known that the expansion velocity is non-uniform (Lämmerzahl *et al.* 1987) and that the outflow may be anisotropic (Weaver *et al.* 1986) and time dependent (Larson *et al.* 1990). These properties of comets limit the applicability of the Haser formulae. Curiously, few efforts have been made to relax these limitations. Festou (1981) reexamined the applicability of the Haser formulae and identified three regions according to the radius  $r_c$  of the collision zone. Inside the collision zone ( $r < r_c$ ) Festou modified the Haser formula to include a Maxwellian dispersion in radial velocity (see his Eq. 8). In the collisionless outer coma ( $r > r_c$ ) Festou re-derived the Haser formula, but in the transition region surrounding  $r_c$  he provided only an integral for the

density distribution. Festou's concern about Haser's hypotheses is valid and his modified formulae address some of them, but we demonstrate below that the Haser formulae do not have to be constrained either by Haser's collisionless hypothesis or by Festou's restrictions concerning the collision zone.

## 4.2. Density Distributions for Non-Uniform Velocity

### 4.2.1. The continuity equation

Both Haser (1957) and Festou (1981) derived Haser's formulae directly from considerations of outflow geometry. Other methods are available. For example, by adopting the Haser hypotheses in §3.2 we derived the Haser formulae from the cometary Boltzmann equation. Since our cometary Boltzmann equation is not constrained by Haser's assumptions, we may derive more general number density distributions directly from the cometary Boltzmann equation and its cousin, the cometary transport equation.

The mass continuity equation is a special case of the transport equation. Starting from Eq. 3.2 and letting the  $Q_s = 1$ , we have

$$\begin{aligned} \frac{\partial n_s}{\partial t} + \nabla \cdot (n \langle v \rangle) &= \Delta[B_s] - \Delta[D_s] \\ &+ \Delta[R_s] + \Delta[J_s] + \sum_{j \neq s} \Delta[J_{sj}]. \end{aligned} \tag{4.1}$$

where  $\Delta[Q]$  is the phase integration of  $Q$  and is defined by Eq. 3.3. From Eqs. 3.4 and 3.8 we know that phase integration of the radiative and collision terms is zero. Also,  $\langle \mathbf{v} \rangle = \mathbf{u}$  is the outflow velocity. Substituting these into Eq. 4.1 we have

$$\frac{\partial n_s}{\partial t} + \nabla \cdot (n_s \mathbf{u}_s) = \Delta[B_s] - \Delta[D_s]. \quad (4.2)$$

The physical meaning of the right side of this equation is obvious.  $\Delta[B_s]$  is the production rate (molecules  $\text{cm}^{-3} \text{sec}^{-1}$ ) of species  $s$  and  $\Delta[D_s]$  is its destruction rate. Equation 4.2 is very general and does not depend upon the rate of collisions, the collisionless assumption, or the size of collision zone.

#### 4.2.2. Parent molecules

Of all of Haser's assumptions, the steady state assumption may be reasonably satisfied depending on the behavior of the comet itself and the type of observation being made. A slow change in gas production over periods of days will not invalidate the steady state assumption, although rapid outbursts could lead to time-dependent behavior of molecules (see, *e.g.*, Larson *et al.* 1990). Spherically symmetric outflow is not realistic in the inner coma but intermolecular collisions and diffusion eventually isotropize the outer coma. Therefore, we focus our attention on the assumption of uniform outflow velocity. This assumption is not valid because of two reasons. First, collisions introduce local thermal velocities in the coma so that not all molecules move in the same direction or with the same velocity at any given time. Second, even the average velocity may change with spatial location. Theoretical models confirmed by

*in situ* observations demonstrate that the average outflow velocity is not constant in the coma. For example, hydrodynamic calculations (see §4.4) predict constant outflow velocity only in the inner coma ( $r < 10^3$  km), but the velocity increases steadily in the region surrounding  $r_c$  (typically  $10^3 - 10^5$  km) where most observations apply. Lämmerzahl *et al.* (1986) found that the outflow velocity in comet P/Halley increased from  $0.8 \text{ km sec}^{-1}$  at  $r = 10^3$  km to  $1.08 \text{ km sec}^{-1}$  at  $3.0 \times 10^4$  km, a change of almost 30%.

Here we derive more general density distribution functions inside the coma. We still assume steady state and spherical symmetry, but we drop the assumptions of uniform velocity and no collisions. For a parent species ( $s = p$ ) the production rate  $\Delta[B_p] = 0$  except on the nuclear surface and the destruction rate  $\Delta[D_p] = n_p/\tau_p$ . Eq. 4.6 becomes

$$\frac{1}{r^2} \frac{d}{dr} (r^2 n_p u_p) = -\frac{n_p}{\tau_p}. \quad (4.3)$$

Assuming  $X(r) = r^2 n_p(r) u_p(r)$ , Eq. 4.3 becomes

$$\frac{1}{X(r)} \frac{dX(r)}{dr} = -\frac{1}{u_p(r) \tau_p}. \quad (4.4)$$

Integrating Eq. 4.4 from  $r_n$  to  $r$ , we obtain

$$X(r) = X(r_n) \exp \left[ - \int_{r_n}^r \frac{dr'}{u_p(r') \tau_p} \right]. \quad (4.5)$$

That is:

$$n_p(r) = (n_p r^2 u_p)_{r=r_n} \left[ \frac{1}{u(r) r^2} \right] \exp \left[ - \int_{r_n}^r \frac{dr'}{u_p(r') \tau_p} \right]. \quad (4.6)$$

The boundary condition is the same as in the Haser model and is given by Eq. 3.9.

Substituting into Eq. 4.6 we obtain the solution

$$n_p(r) = \frac{Q_p}{4\pi r^2 u_p(r)} \exp \left[ - \int_{r_n}^r \frac{dr}{u_p(r) \tau_p} \right]. \quad (4.7)$$

This is the *generalized* number density distribution for parent molecules with non-uniform velocity. Note that only the average outflow velocity appears in the formula and the number density distribution is therefore independent of velocity dispersion. Our density distribution in Eq. 4.7 includes the Haser formula as a special case: for  $u_p(r) = \text{constant}$  Eq. 4.7 reduces to the Haser formula for parent molecules (Eq. 3.11).

### 4.2.3. The scale-length

The scale-length  $l_p$  and photodestruction lifetime  $\tau_p$  of a parent species are related parameters. Because of the limited lifetime of molecules, most parent molecules exist inside a finite region not very far from the nucleus. For spherically symmetric outflow this region is characterized by a distance called the scale-length. When the outflow velocity is constant and directed radially the scale-length is conveniently defined as  $l_p = u_p \tau_p$ . When  $u_p = u_p(r) \neq \text{constant}$ , however, more consideration should be given. Note that in the case of constant velocity,  $l_p$  is the distance at which a flux of molecules is reduced to  $e^{-1}$  of its original value at the nuclear surface. We therefore generalize the scale-length as

$$\int_{r_n}^r \frac{dr}{u \tau_p} = 1. \quad (4.8)$$

This formula suggests that  $l_p$  may not be equal to  $\langle u_p \rangle \tau_p$  when  $u_p$  is not constant.

### 4.2.4. Daughter products

Similarly, we generalize the number density distribution for daughter products. For a daughter product  $s = d$ ,  $\Delta[B_d] = BR_p^d n_p / \tau_d$ , where  $BR_p^d$  is the branching ratio, and  $\Delta[D_d] = n_d / \tau_d$  (from Eq. 3.5-3.6). Under the assumptions of steady state and spherical symmetry the continuity equation (Eq. 4.2) becomes

$$\frac{1}{r^2} \frac{d}{dr} (r^2 u_d n_d) = \frac{n_p}{\tau_p} - \frac{n_d}{\tau_d}, \quad (4.9)$$

where  $\tau_p^d = \tau_p/BR_p^d$  and  $u_d$  is the outflow velocity of daughter  $d$ . Substituting Eq. 4.7 into Eq. 4.9 and solving the resulting equation, we obtain

$$n_d = \frac{Q_p}{4\pi u_d r^2} e^{-\int_{r_n}^r \frac{dr}{u_d \tau_d}} \int_{r_n}^r \frac{dr'}{u_p \tau_p} \exp\left[\int_{r_n}^{r'} \left(\frac{1}{u_p \tau_p} - \frac{1}{u_d \tau_d}\right) dr''\right]. \quad (4.10)$$

This formula is complicated in form and we do not expect to use it without simplifications. However, we can infer some properties directly from the formula. For example, from inspection of Eq. 4.10 we see that 1) the number density of daughter products in a coma is directly proportional to the production rate of the parents, 2) the number density of the daughter products depends on the average outflow velocities of both parent and daughter molecules, and 3) the number density of daughter products does not depend directly on local thermal motion. When  $u_p = \text{constant}$  and  $u_d = \text{constant}$ , this equation reduces to Haser's two-stage formula (Eq. 3.12).

### 4.3. Time Dependence and Anisotropy

Up to now spherical symmetry and steady outflow have been assumed in order to derive the density formulae. In this section we explore the possibility of extending the density formulae to include effects of anisotropy and time-dependence. A general solution for time-dependent, anisotropic outflow needs more sophisticated models since many complicated physical phenomena may occur. However, a simplified formula is possible if our intention is only to relax *some* conditions.

#### 4.3.1. Time-dependence of the distribution functions

The production rate of a parent species varies slowly with rotation of the cometary nucleus. One predicted property of molecular outflow from hydrodynamic models is that the average outflow velocity curves vary slowly with production rate. For example, a two order of magnitude difference in the gas production rate results only in a 20% difference in the outflow velocity for  $r < 10^4$  km, and a factor of 2 difference in the outer coma (see §4.4). We write the production rate as  $Q(t) = Q_0 + Q_f(t)$ . If  $Q_f(t)$  is small compared to the constant  $Q_0$ , then the outflow velocity  $u_p(r, t)$  changes little with  $t$ . In other words, *the average velocity  $u_p(r)$  is independent of time* under certain conditions. Assuming  $u_p(r)$  is independent of time and the outflow is spherically symmetric, the continuity equation for parent molecules is

$$\frac{\partial n_p}{\partial t} + \frac{1}{r^2} \frac{\partial}{\partial r} (r^2 n_p u_p) = -\frac{n_p}{\tau_p}. \quad (4.11)$$

We express the production rate  $Q_p(t)$  and number density  $n_p(r, t)$  in terms of the Fourier integrals

$$Q_p(t) = \frac{1}{\sqrt{2\pi}} \int Q_p(\omega) e^{i\omega t} d\omega \quad (4.12)$$

and

$$n_p(r,t) = \frac{1}{\sqrt{2\pi}} \int m_p(r,\omega) e^{i\omega t} d\omega. \quad (4.13)$$

Substituting Eqs. 4.12 - 4.13 into Eq. 4.11, we obtain

$$\frac{1}{r^2} \frac{d}{dr} [r^2 m_p(r,\omega) u_p] = - \left( \frac{1}{\tau_p} + i\omega \right) m_p(r,\omega). \quad (4.14)$$

This equation is similar to Eq. 4.3 and its solution is

$$m_p(r,\omega) = \frac{Q_p(\omega)}{4\pi u_p(r) r^2} \exp \left[ - \int_{r_n}^r \frac{dr'}{u_p} \left( \frac{1}{\tau_p} + i\omega \right) \right]. \quad (4.15)$$

Substituting Eq. 4.15 back into 4.13, we obtain

$$n_p(r,t) = \frac{Q_p \left( t - \int_{r_n}^r \frac{dr}{u_p(r)} \right)}{4\pi u_p(r) r^2} \exp \left( - \int_{r_n}^r \frac{dr}{u_p(r) \tau_p} \right). \quad (4.16)$$

This is the time-dependent density formula for parent molecules under the assumption that  $u_p(r)$  is time-independent.

It is instructive to write down the time-dependent number density function for

constant outflow velocity. Equation 4.16 becomes

$$n_p(r,t) = \frac{Q_p \left( t - \frac{r-r_n}{u_p} \right)}{4\pi u_p r^2} \exp\left( -\frac{r-r_n}{u_p v_p} \right). \quad (4.17)$$

This formula has been used without derivation by several authors (see *e.g.*, Hsieh *et al.* 1987, Magee-Sauer *et al.* 1988).

#### 4.3.2. The anisotropy factor

It was believed that outflow in the coma should be asymmetric due to non-uniform heating by solar radiation of volatile materials and the possible formation of a dust mantle on the nuclear surface. This expectation is supported by observations (see *e.g.*, Ip 1985 for a review). Unfortunately, the details of asymmetric gas outflow are not well known and a rigorous study of three-dimensional outflow requires mathematically and numerically complex modeling of the cometary Boltzmann equation and detailed knowledge of surface properties on the cometary nucleus. Kitamura (1986, 1987), Kömle and Ip (1987), and Korosmezey and Gombosi (1990) took the first step toward multi-dimensional modelling by studying axisymmetric outflow in the coma. An important result from these preliminary analyses is the formation of a jet cone from an initially narrow gas jet. Near the nuclear surface a narrow jet expands both laterally and radially with comparable velocities, mainly because of the pressure gradients in both directions. The lateral expansion quickly subsides after  $r > 3r_n$ , however, where  $r_n$  is

the radius of the nucleus, while the radial outflow velocity continues to increase. At larger  $r$  the radial velocity becomes an order of magnitude larger than lateral velocity. The result is the formation of a relatively stable jet propagating radially outward (Korosmezey and Gombosi 1990). In view of this predicted behavior we therefore adopt the following approximation: *At each point in the coma the average outflow velocity has a radial component and negligible non-radial components.* With this assumption the continuity equation for parent molecules becomes

$$\frac{1}{r^2} \frac{d}{dr} (r^2 u_r n_p) = -\frac{n_p}{\tau_p}. \quad (4.18)$$

The boundary equation is

$$n(r_n, \theta, \phi) = \frac{Q_p G(\theta, \phi)}{4\pi u_p(r_n) r_n^2}, \quad (4.19)$$

where  $G(\theta, \phi)$  is an *anisotropy factor* defined such that it is  $4\pi$  when integrated over all directions. Equations 4.18 - 4.19 are solved using similar procedures to those in §4.2.2. The solution is

$$n_p(r, \theta, \phi) = \frac{Q_p}{4\pi u_p(r, \theta, \pi) r^2} \exp\left[-\int_{r_n}^r \frac{dr}{u_r \tau_p}\right] G(\theta, \phi). \quad (4.20)$$

We will find it convenient later to rewrite the anisotropy factor as  $\alpha + \beta G(\theta, \phi)$  where the ratio  $\alpha/\beta$  represents the relative contributions of isotropic and asymmetric outflow components.

Equation 4.20 may be modified to include other characteristics of the outflow in the coma. For example, the relatively small lateral outflow velocity components are taken into account by adding a slowly varying  $r$ -dependence to a modified asymmetry factor  $G(r, \theta, \phi)$ , where

$$\int_0^{2\pi} d\phi \int_0^\pi \sin(\theta) d\theta G(r, \theta, \phi) = 4\pi$$

*and* (4.21)

$$\lim_{r \rightarrow \infty} G(r, \theta, \phi) = 1.$$

The last condition represents isotropization processes that certainly are at work.

#### 4.4. The Outflow of H<sub>2</sub>O

Before we proceed to the spectral outflow model in next chapter, it is useful to summarize here some numerical results obtained from the hydrodynamic equations of the coma. We assume that the dominant parent molecule in the coma is H<sub>2</sub>O and that the hydrodynamic equations written by Crovisier (1984) apply. However, we replace the photolytic heating term in the energy equation by the semi-empirical formula

interpolated by Bockelee-Morvan and Crovisier (1987b).

#### *4.4.1. Outflow velocity*

The major property of the outflow velocity profile of H<sub>2</sub>O in Figs. 4.1a and 4.1b is its  $r$ -dependence, particularly its monotonous increase with  $r$ . In the inner coma the high pressure gradient quickly accelerates the gas to a supersonic value of  $\approx 0.8$  km sec<sup>-1</sup> within 10<sup>2</sup> kilometers. Then the pressure gradient largely subsides and the outflow velocity becomes nearly constant until photolytic heating by hot H-atoms released during photodestruction of H<sub>2</sub>O accelerates H<sub>2</sub>O at  $r = 10^4$  km. The outflow velocity may increase to 2 km sec<sup>-1</sup> in the outer coma (see Fig. 4.1) if the gas production rate is high enough.

Most hydrodynamic models predict a plateau region from approximately 100 - 5000 km in the velocity curve (Fig. 4.1). Although models differ in their detailed implementation of energy terms, most predict a velocity of  $\approx 0.8$  km sec<sup>-1</sup> in this region. Recently, Crifo (1990) modeled the effects of water clustering and concluded that heat release during H<sub>2</sub>O recondensation may provide extra energy that would significantly increase the outflow velocity and eliminate the plateau region from the velocity curve (Figs. 4.1a and 4.1b).

#### *4.4.2. Temperature*

The kinetic temperature of H<sub>2</sub>O in cometary comae changes rapidly with radial distance (Figs. 4.2a and 4.2b). In the inner coma the rapid expansion and subsequent adiabatic cooling of the gas significantly reduces the coma temperature to about 10 °K at a distance of a few dozen kilometers. This region is of considerable theoretical

interest since the low temperature may cause recondensation of H<sub>2</sub>O (Kitamura and Yamamoto 1985). The low temperature is also the basis for Crifo's (1990) H<sub>2</sub>O cluster model. In the region between 10<sup>2</sup> to 5 x 10<sup>4</sup> km radiative and photolytic heating causes the temperature to increase again. If the gas production rate is high enough ( $Q > 10^{29}$  molecules sec<sup>-1</sup>) the temperature may rise as high as 200 °K before collisional decoupling of molecules reduces it again.

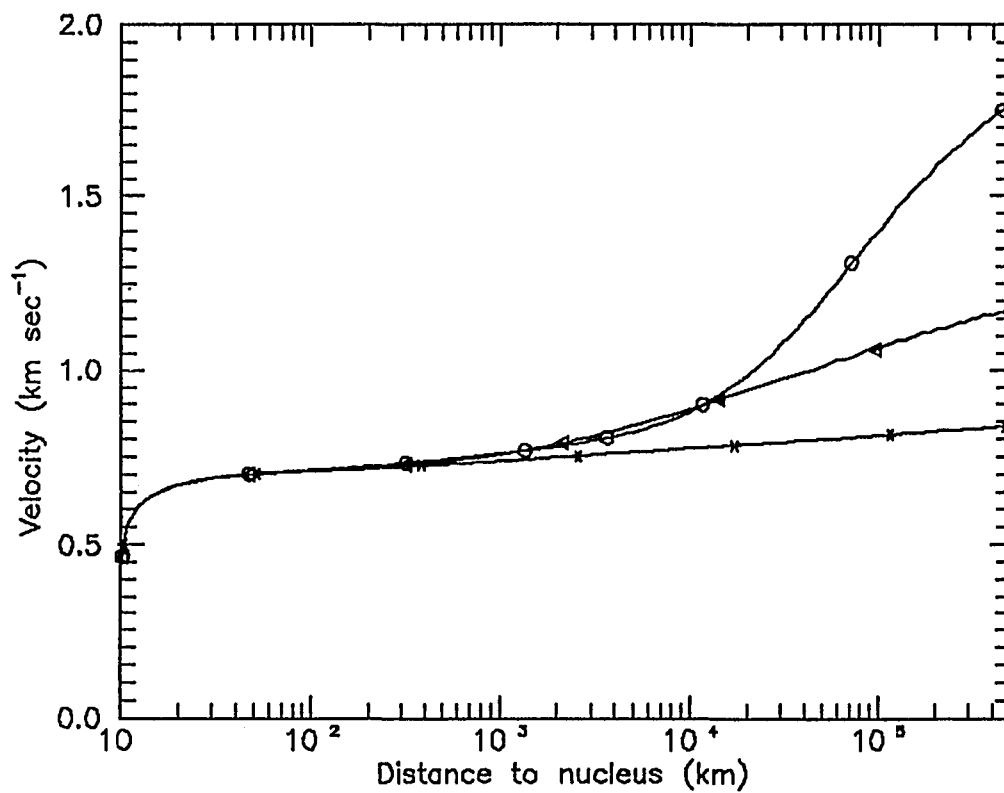


Figure 4.1a. The effect of production rate  $Q_p$  on the  $H_2O$  outflow velocity. The outflow velocity is calculated from spherically symmetric hydrodynamic equations; the heliocentric distance of the comet is 1 AU. The velocity curves are:  $10^{28}$  molecules  $sec^{-1}$  (curve with stars),  $10^{29}$  molecules  $sec^{-1}$  (curve with triangles) and  $10^{30}$  molecules  $sec^{-1}$  (curve with circles). In general, the outflow velocity increases with the production rate.

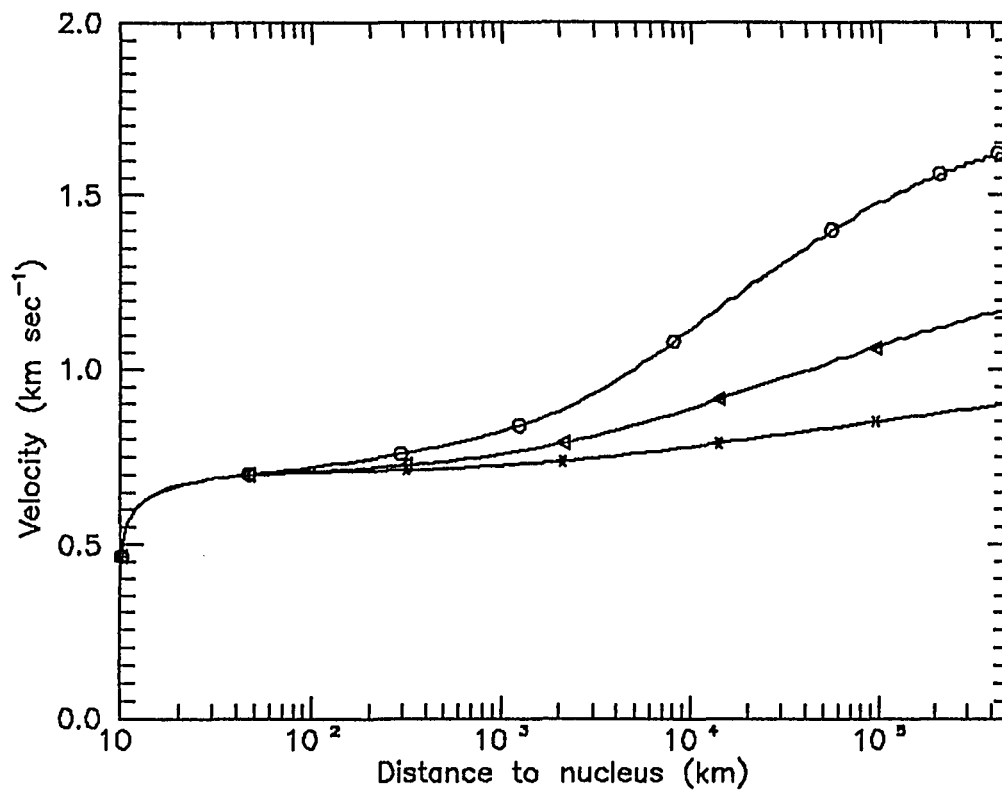


Figure 4.1b. The effect of heliocentric distance  $R_h$  on the  $H_2O$  outflow velocity. The production rate of  $H_2O$  is maintained at  $10^{29}$  molecules  $sec^{-1}$ . The heliocentric distances are: 2.0 AU (curve with stars), 1 AU (curve with triangles) and 0.5 AU (curve with circles). In general, the outflow velocity increases as the comet approaches the sun.

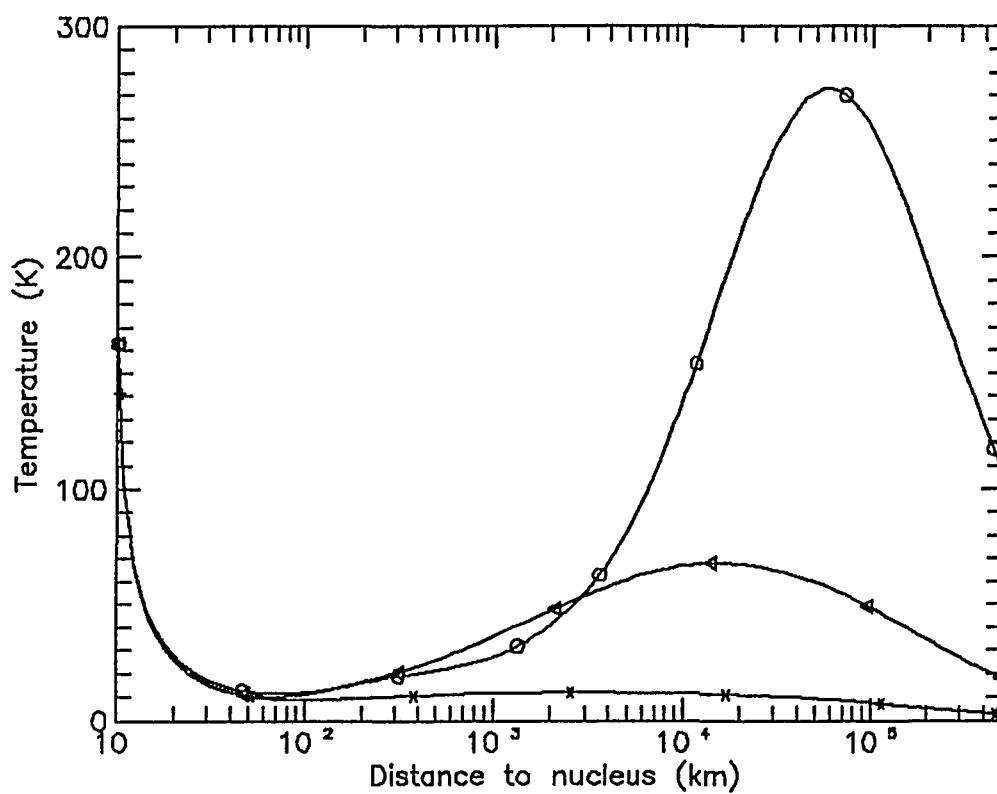


Figure 4.2a. The effect of production rate  $Q_p$  on the temperature profiles of  $H_2O$  molecules. The temperature is calculated from spherically symmetric hydrodynamic equations; the heliocentric distance of the comet is 1 AU. The velocity curves are:  $10^{28}$  molecules  $sec^{-1}$  (curve with stars),  $10^{29}$  molecules  $sec^{-1}$  (curve with triangles) and  $10^{30}$  molecules  $sec^{-1}$  (curve with circles). In general, the kinematic temperature increases with the production rate.

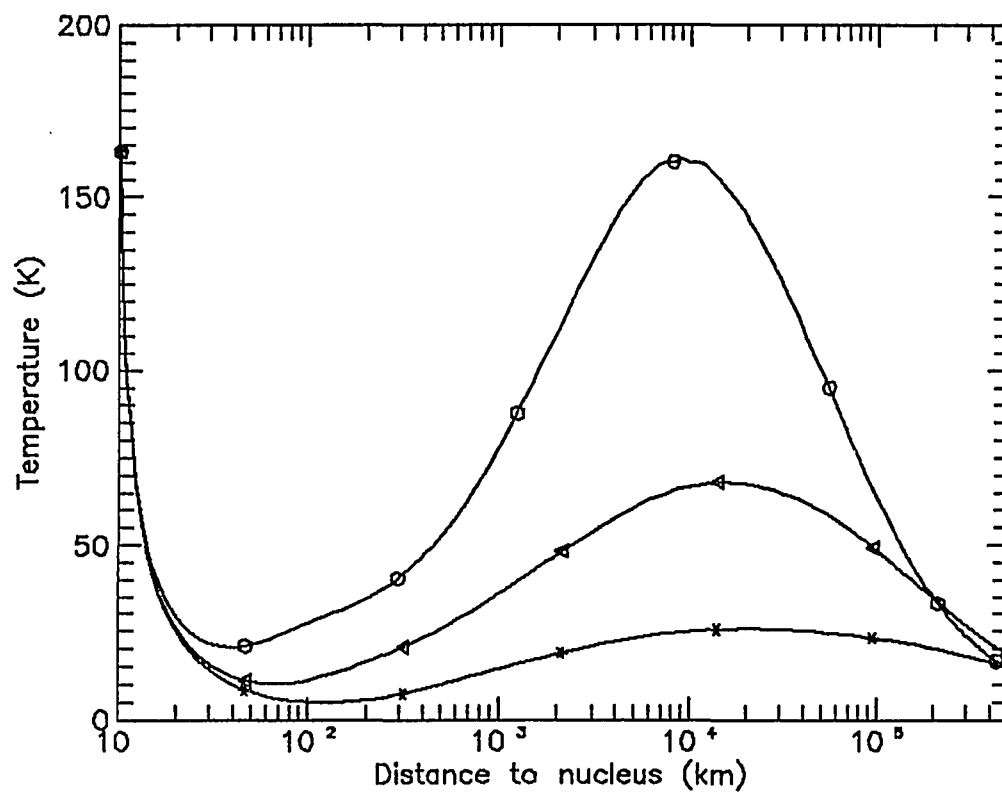


Fig. 4.2b: The effect of heliocentric distance  $R_h$  on temperature profiles of  $H_2O$  molecules. The production rate of  $H_2O$  is maintains at  $10^{29}$  molecules  $sec^{-1}$ . The heliocentric distances are: 2.0 AU (curve with stars), 1 AU (curve with triangles) and 0.5 AU (curve with circles). In general, the kinematic temperature increases as the comet approaches the sun.

## CHAPTER 5

### A SPECTRAL OUTFLOW MODEL

#### 5.1. Introduction

In this chapter we address the issue of exploiting the full information content of velocity-resolved spectra of parent molecules in cometary comae. Available models are inadequate due both to rapid progress in remote spectroscopic techniques and to previous emphasis on the interpretation of spectra of daughter species. Early outflow models were developed to deduce kinematic parameters of the neutral gas from radio line profiles of OH, the only coma species for which sufficient spectral resolution *and* signal-to-noise ratio (SNR) could be achieved. Despois *et al.* (1981) analyzed OH line profiles in comet C/West (1976 VI) and C/Kohler (1977 XIV). They estimated that the expansion velocity of OH was  $\approx 1.5 \text{ km sec}^{-1}$  and suggested that the parent distribution was anisotropic. Bockelée-Morvan and Gérard (1984) analyzed radio OH lines in C/Meier (1978 XXI), C/Bradfield (1979 X), and C/Austin (1982 g) using the Monte Carlo vectorial method (Combi and Delsemme 1980, Festou 1981). Their estimates of the OH outflow velocity were very dependent on assumptions concerning the parent outflow distribution. They suggested that the parent and OH outflow velocities were in the range 0.6 - 1.4 and 0.7 - 1.4  $\text{km sec}^{-1}$ , respectively. Anisotropy in the parent distribution was invoked to account for asymmetry in the observed OH spectral line profiles. More recent kinematic analyses of radio OH line profiles were performed by Tacconi-Garman (1989), Tacconi-Garman *et al.* (1990), and Bockelée-Morvan *et al.*

(1990). Tacconi-Garman *et al.* found convincing evidence for time-variable anisotropy in the parent distribution extending to a radial distance of  $5 \times 10^5$  km and they also retrieved expansion velocities ranging from 0.4 - 1.8 km sec<sup>-1</sup>. Bockelée-Morvan *et al.*'s model did not include anisotropy as a retrievable parameter but they noted that some of their OH data clearly showed evidence of asymmetric outflow. Thus, velocity-resolved line profiles of OH are certainly influenced by the neutral gas outflow but retrieval of the velocity field and density distribution of the parent species from these data remains a difficult task with high model-dependent uncertainties. The fundamental problem is that OH line profile analyses must consider the density distributions of both H<sub>2</sub>O and OH. The density distribution and velocity field of H<sub>2</sub>O are influenced by many coma processes that are themselves the subject of considerable observational and theoretical work and a significant, additional complication with OH is its movement in the coma following photodissociation of H<sub>2</sub>O. The Monte Carlo particle trajectory method (Combi and Delsemme 1980) and the vectorial method (Festou 1981) are important tools for describing the OH component, but simplifications are invariably required in the combined OH/H<sub>2</sub>O model in order to achieve reasonable computing times. In practice it seems that the H<sub>2</sub>O outflow component of OH kinematic models is subjected to the most simplification (*e.g.*, assumed to be a Haser model) which means that the retrieved kinematic parameters for H<sub>2</sub>O may not accurately describe actual conditions in the coma.

The obvious way to reduce these model-dependent uncertainties is to use spectra

of parent molecules. This is a much more recent possibility because detecting parent molecules has itself been a major challenge to cometary astronomers. High resolution spectra suitable for kinematic analyses are now available for two parent molecules, H<sub>2</sub>O and HCN. The H<sub>2</sub>O spectra were used to measure the expansion velocity (Larson *et al.* 1987), spatial anisotropy (Weaver *et al.* 1987) and temporal variability (Larson *et al.* 1990) in the neutral gas outflow, and the HCN data were used to estimate the expansion velocity (Schloerb *et al.* 1987a). Some of the assumptions used in these and other kinematic analyses need to be reconsidered, however. For example, many authors assume that the outflow velocity is constant and equal to one half of the observed line width. Combi (1989) used his dusty-gas-dynamic/Monte Carlo model to demonstrate the inadequacy of this approximation for the analysis of radio HCN lines, but its failing is more general than that. The inference of kinematic conditions in the coma from spectral line profiles is actually quite complex because the few observables that are available for interpretation (*e.g.*, line width, line center, line shape) are influenced by multiple coma parameters (*e.g.*, outflow distribution, outflow velocity, kinematic temperature) and viewing conditions (*e.g.*, FOV, phase angle, instrumental effects). Since all remote spectroscopic observations integrate along the comet-Earth line of sight (LOS), a model is needed to reconstruct the velocity field and three-dimensional density distribution in the outflow.

In this chapter we therefore present a systematic study of how conditions in the coma affect parent molecule spectral line profiles. In §5.2 we review line broadening mechanisms and other conditions in the coma that affect the shape of spectral lines and

in §5.3 we describe our spectral model incorporating these dynamic processes. In §5.4 we review the simplifying assumptions and Monte Carlo computational procedures that are necessary to make practical use of the model and in §5.5 we present synthetic spectra to illustrate the effect of various coma processes on observed spectral lines. In Chapter 6 we apply this insight to the interpretation of velocity-resolved H<sub>2</sub>O line profiles observed in comets P/Halley and Wilson (1987 VII) (see also Larson *et al.* 1991).

## 5.2. Line Broadening Mechanisms

Spectral line profiles have finite widths because of the motion of molecules in the coma, the finite lifetimes of excited radiative states, and the instrumentation used to record them. Instrumental broadening is not fundamental in terms of cometary physics, of course, but we include it here because the effects are often inevitable. We review each line broadening process below.

### 5.2.1. Doppler broadening.

Molecules moving at velocity  $v$  emit photons with Doppler-shifted frequencies  $\nu = \nu_0(1 - v/c)$  where  $c$  is the speed of light and  $\nu_0$  is the transition's rest frequency. Since an observed spectral line is the superposition of all Doppler-shifted emission in the spectrometer's FOV, molecular motion in the coma affects the width, shape, and position of an observed spectral line. Only velocity components along the LOS are preserved in an observed line profile, however; knowledge of the other components must be deduced from a three-dimensional outflow model fit to the data. Parent

molecules acquire motion in the coma because of two processes: adiabatic expansion of gas released from the nucleus and collisions with gas and dust in the high density region of the inner coma. In typical comae the velocity dispersion due to expansion is  $\Delta v \approx 2 \text{ km sec}^{-1}$  so the degree of line broadening for isotropic outflow is on the order of  $\Delta v/\nu_0 = \Delta v/c \approx 7 \times 10^{-6}$ . Velocity dispersion acquired in collisions is estimated from a Maxwellian distribution of width  $\Delta v_D = [2kT/m]^{1/2}$ . For  $\text{H}_2\text{O}$  at  $100 \text{ }^\circ\text{K}$  the "thermal" contribution to the observed line width is  $\Delta v_D/c \approx 2.0 \times 10^{-6}$ . Daughter molecules may have additional velocity components due to kinetic energy acquired from photodissociation.

### 5.2.2. Natural width.

The finite lifetimes of energy levels give rise to a natural line width. The natural line profile is the Lorentz function

$$F(\nu) = \frac{\left(\frac{\gamma}{4\pi}\right)^2}{(\nu - \nu_0)^2 + \left(\frac{\gamma}{4\pi}\right)^2} \quad (5.1)$$

in which  $\gamma$  is the spontaneous decay rate between energy levels. A typical decay rate in the  $\nu_3$  band of  $\text{H}_2\text{O}$  at  $2.65 \text{ } \mu\text{m}$  is  $\gamma \approx 10 \text{ s}^{-1}$  and its contribution to the relative line width is therefore on the order of  $\Delta\nu/\nu_0 = \gamma/2\pi\nu_0 \approx 10^{-14}$ . The lifetime of an energy level may be shortened by collisions, thus broadening the natural line profile.

Collisional broadening is also represented by a Lorentz profile with width parameter  $\Gamma = \gamma + 2\gamma_{col}$ . The collision rate with other particles is  $\gamma_{col} = n\sigma\bar{v}$  where  $\sigma$  is the collision cross-section,  $\bar{v}$  is the relative collision velocity, and  $n$  is the number density of the colliding particles. In a pure H<sub>2</sub>O coma  $\sigma \approx 10^{-16} \text{ cm}^2$  and  $\bar{v} = [16kT/\pi m]^{1/2}$ . Assuming a Haser model for the H<sub>2</sub>O density distribution (production rate  $Q_{\text{H}_2\text{O}} = 1 \times 10^{30} \text{ sec}^{-1}$ , outflow velocity  $v_{\text{H}_2\text{O}} = 1 \text{ km sec}^{-1}$ , and scale-length  $\ell_{\text{H}_2\text{O}} = 8.3 \times 10^4 \text{ km}$ ) the collision rate becomes  $\gamma_{col} = 10^3 r^{-2} \exp(-r/\ell)$ . The collision rate near the nuclear surface ( $\gamma_{col} \approx 10 \text{ sec}^{-1}$  at  $r = 10 \text{ km}$ ) is comparable to the natural rate of decay, but it decreases rapidly with  $r$ . Thus, the natural line width even when augmented by collisions in the near-nuclear region is negligibly small compared to Doppler broadening.

### 5.2.3. Instrumental broadening.

Spectral lines formed in cometary comae are usually modified by the instruments used to observe them. Typical effects include increased line width and changes to the line shape. The observed cometary line profile  $F_{obs}(\nu)$  is related to the source line profile  $F(\nu)$  by the convolution

$$F_{obs}(\nu) = \int F(\nu') I(\nu - \nu') d\nu' \quad (5.2)$$

in which  $I(\nu)$  is the instrument response function. If the width of  $I(\nu)$  is much larger than that of  $F(\nu)$ , no information concerning the source profile can be recovered. In the important range where the widths of  $I(\nu)$  and  $F(\nu)$  are comparable, however,  $F(\nu)$

may be retrieved from Eq. 5.2 by deconvolution techniques if  $I(\nu)$  is a well defined analytic function that closely represents actual spectrometer performance at the telescope. In general, deconvolution is not a substitute for better experiments but it is the only way to extract maximum information from measurements that cannot be repeated, as is usually the case with comet observations.

The relative contributions to the line width for the processes identified above are summarized in Table 5.1. The dominant sources of line broadening in the coma are due to LOS components of the radial expansion velocity and velocity acquired in collisions. Another major, and possibly dominant, influence on the observed line shape is the spectrometer itself. Line profile analyses are therefore dependent upon the acquisition of spectra at the highest possible resolution and SNR consistent with cometary

Table 5.1. Contributions to Cometary Spectral Line Widths

Line Broadening Process	Line Width (km sec <sup>-1</sup> FWHM)	Treatment
Radial velocity	≈2.0	Outflow model
Collisions	≈0.6	Outflow model
Natural width	≈0.0	None required
Spectrometer ILS	<0.2	None required
	0.2 - 5.0	Deconvolution
	>5.0	New instrument

flux levels and available observing time. Use of our outflow model presumes that the

observed line profiles are free of instrumental effects either because the instrumental line shape (ILS) was very narrow relative to the cometary line or because artifacts of the ILS were removed by numerical deconvolution procedures.

### 5.3. The Physical Model

The frequency distribution in a cometary line profile is effectively a histogram of velocity components along the LOS. In this section we develop the mathematical correspondence between the shape of a spectral line and the thermal and kinematic properties of a cometary atmosphere. We use the cometocentric coordinate system illustrated in Fig. 5.1. The comet-Earth LOS is along the Z-direction and the Sun is in the X-Z plane. A point in the coma at spherical coordinate  $\mathbf{r} = (r, \theta, \phi)$  is surrounded by the volume element  $d^3\mathbf{r} = r^2 \sin(\theta) dr d\theta d\phi$ . The circular FOV integrates emission from a cylindrical volume of the coma along the LOS.

#### 5.3.1. Distribution function.

We assume that the motion of a molecular gas is independent of its energy level and is represented by its (total) distribution function  $f(\mathbf{r}, \mathbf{v}, t)$ , defined as the sum of distribution functions over all energy states  $k$ :

$$f(\mathbf{r}, \mathbf{v}, t) = \sum_k f(\mathbf{r}, \mathbf{v}, \epsilon_k, t). \quad (5.3)$$

Therefore the number density is

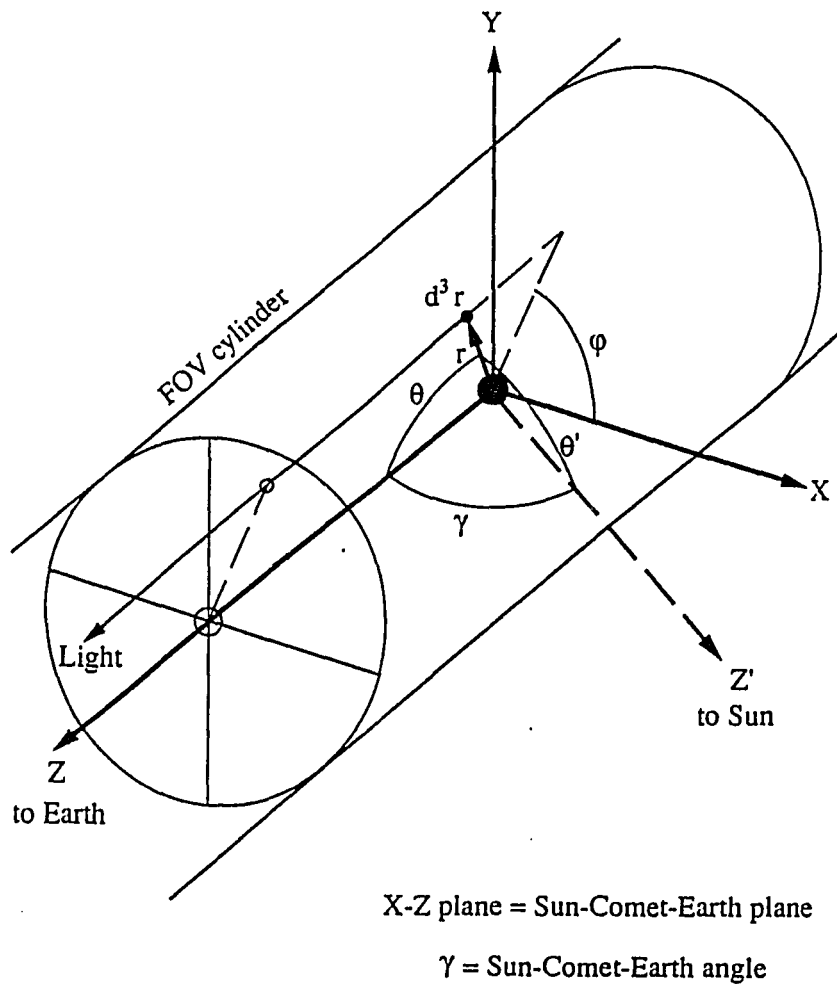


**Figure 5.1.** The cometocentric coordinate system for interpreting Earth-based observations. The Sun, comet, and Earth are in the X-Z plane. Light emitted from the volume element  $d^3r$  at spherical coordinate  $(r, \theta, \phi)$  can reach the Earth-based observer only if the element is within the cylindrical volume defined by the circular FOV *and* the emitted photons travel parallel to the comet-Earth LOS.

$$n(\mathbf{r}, t) = \int f(\mathbf{r}, \mathbf{v}, t) d^3\mathbf{v} \quad (5.4)$$

and the average outflow velocity is

$$\mathbf{u}(\mathbf{r}, t) = \frac{1}{n(\mathbf{r}, t)} \int \mathbf{v} f(\mathbf{r}, \mathbf{v}, t) d^3\mathbf{v}. \quad (5.5)$$

In principle,  $f(\mathbf{r}, \mathbf{v}, t)$  can be calculated by solving the cometary Boltzmann equation. Due to the lack of efficient algorithms, however, we will not use this approach in this chapter. Instead, we start from the basic concepts of the dilute gas model and rely on additional assumptions to develop them for practical use. We first assume that the steady state applies, thus eliminating the time  $t$  from all expressions. Temporal variations in gas production are commonly observed, however; see Larson *et al.* (1990) and references therein for descriptions of the time varying behavior of H<sub>2</sub>O and other species in comet P/Halley. Our approach in this chapter is to ignore temporal variations in gas production that occur on time scales much longer than the integration time in a recorded spectrum ( $\approx 10^2$  min) and to consider short term brightness variations as a type of noise that may distort the observed line profile and limit its interpretation. The second simplification concerns treatment of the multiple components of velocity in the outflow. Since  $f(\mathbf{r}, \mathbf{v})$  is proportional to density  $n(\mathbf{r})$  we express  $f(\mathbf{r}, \mathbf{v})$  as the product of a density term and a local velocity distribution

$$f(\mathbf{r}, \mathbf{v}) = n(\mathbf{r}) V_L(\mathbf{r}, \mathbf{v}). \quad (5.6)$$

where  $V_L$  is normalized to unity. If LTE applies, the thermal velocity distribution  $V_L(r, \mathbf{v})$  is the Maxwellian distribution

$$V_L(r, \mathbf{v}) = \left[ \frac{m}{2\pi kT} \right]^{\frac{3}{2}} \exp \left[ -\frac{m}{2\pi kT} (\mathbf{v} - \mathbf{u})^2 \right]. \quad (5.7)$$

where  $T$  is the local temperature and  $\mathbf{u}$  is the outflow velocity. The thermal velocity component of a molecule is defined as  $\mathbf{v}_L = \mathbf{v} - \mathbf{u}$  and the observable velocity distribution along the LOS (Z-axis) is

$$f(r, v_z) = \int f(r, \mathbf{v}) dv_x dv_y = n(r) V_L(r, v_z). \quad (5.8)$$

### 5.3.2. Excitation.

The excitation of parent molecule spectra is due to two processes: radiative excitation by solar IR photons and collisional excitation by other particles. The radiative excitation rate is assumed to be constant throughout the coma. Collisional excitation and de-excitation depends upon the collision rate which is a function of the local density of particles. We express molecular excitation in terms of a *g-factor*  $g(r)$  (photons molecule<sup>-1</sup> sec<sup>-1</sup>) which is the probability per unit time that a molecule will emit a photon. The *g-factor* is generally a function of  $r$  due to its dependence on collisions.

### 5.3.3. Radiative losses.

The specific intensity of spectral line emission originating in the coma at  $d^3r$  is given by

$$dI_\nu(\mathbf{r}) = \frac{h\nu_0}{4\pi} g(\mathbf{r}) f(\mathbf{r}, \nu_z) d^3r. \quad (5.9)$$

This flux must traverse other parts of the coma before it is received by telescopes on Earth. The line transfer equation is

$$\frac{d(dI_\nu(\mathbf{r}))}{ds} = -n(\mathbf{r}) \alpha_\nu dI_\nu(\mathbf{r}) \quad (5.10)$$

where  $\alpha_\nu$  is the scattering cross-section per molecule. The stimulated emission term is very small and has been ignored. The flux received at Earth is

$$dI_\nu(\text{Earth}) = dI_\nu(\mathbf{r}) \exp[-\tau(\mathbf{r})] = \frac{h\nu_0}{4\pi} g(\mathbf{r}) f(\mathbf{r}, \nu_z) \exp[-\tau(\mathbf{r})] d^3r \quad (5.11)$$

where  $\tau(\mathbf{r}) = \int \alpha_\nu n(\mathbf{r}) ds$  is the optical depth along the LOS from the volume element  $d^3r$  to Earth.

#### 5.3.4. The spectral line shape.

We integrate the flux received at Earth in Eq. 5.11 over the FOV to obtain the observed spectral line profile

$$F(v_z) = A \int_{FOV} g(\mathbf{r}) n(\mathbf{r}) V_L(\mathbf{r}, v_z) \exp[-\tau(\mathbf{r})] d^3\mathbf{r} \quad (5.12)$$

in which  $A$  is a normalization constant and Eq. 5.8 was used for  $f(\mathbf{r}, v_z)$ . We have also expressed the line profile in terms of the observable cometocentric velocity  $v_z$  rather than the radiative frequency  $\nu$  such that  $v_z = 0$  at  $\nu_0$  (*i.e.*,  $v_z$  and  $\nu$  may be used interchangeably). If LTE holds in the FOV then Eq. 5.12 becomes upon substitution from Eq. 5.7:

$$F(v_z) = A \int_{FOV} g(\mathbf{r}) \exp[-\tau(\mathbf{r})] n(\mathbf{r}) \left[ \frac{m}{2\pi kT} \right]^{\frac{1}{2}} \exp\left[ -\frac{m}{2\pi kT} (v_z - u_z)^2 \right] d^3\mathbf{r}. \quad (5.13)$$

Equations 5.12 and 5.13 are the foundation of our neutral gas outflow model for synthesizing molecular line spectra. Equation 5.13 depends explicitly on fundamental coma parameters such as the kinetic temperature, the outflow velocity, and, most importantly, the density distribution function. If these are known throughout the coma then Eq. 5.13 offers a direct way to synthesize cometary spectral line profiles. Rigorous evaluation of Eq. 5.13 requires the following steps: (1) establish gas dynamic equations for the coma; (2) adopt a set of plausible boundary conditions for fixed coma

parameters such as gas production rates and photochemical lifetimes; (3) solve the equations for  $n(r)$ ,  $u(r)$ , and  $T(r)$ ; (4) calculate the g-factor  $g(r)$ ; (5) Integrate over the radiative transfer equation to find  $\tau(r)$ ; and (6) use Eq. 5.13 to synthesize the line profile point by point. However, the computing time for this sequence is unrealistically high because of the need to solve three-dimensional gas dynamic equations at each iteration. We therefore implemented the following procedures and simplifying assumptions in order to make practical use of Eqs. 5.12 and 5.13.

## 5.4. Computational Procedures

### 5.4.1. *The choice of density distribution*

In Chapter 4 we proposed a density formula (Eq. 4.17) for anisotropic outflow. We will use Eq. 4.17 as the density distribution in order to include anisotropy and yet retain computational simplicity. In addition, we assume that the outflow velocity is only r-dependent, *i.e.*,  $u = u(r)$ . Depending upon boundary conditions, axisymmetric calculations predict that the value of  $u_r$  may differ by up to 20% in different directions in the outflow (Kitamura 1987). We defer consideration of this effect in order to limit the number of adjustable parameters only to those with the largest influence on observed line profiles in our present model.

### 5.4.2. *The excitation rate and optical depth effects*

Since the gas density is generally low in cometary comae, molecular excitation is due primarily to resonant fluorescence. Only in the inner coma is the gas density high enough to cause significant excitation by collisions. Detailed studies of excitation

conditions at IR wavelengths in spherically symmetric comae have been conducted by several groups (see *e.g.*, Weaver and Mumma 1984, Bockelée-Morvan 1987). Validation of these models is limited by numerous factors, including lack of detailed knowledge concerning collisional coupling between different rotational states. Moreover, three-dimensional models of excitation conditions in comets do not exist. The common practice among modelers is to assume that fluorescence excitation dominates to the extent that excitation is constant throughout the coma, a condition that probably is justified when the gas production rate is relatively low. If the production rate is high this assumption may be valid only in the outer coma.

A related factor in excitation models is the optical depth. The column densities of species whose abundances are low (*e.g.*, HCN, CO, CO<sub>2</sub>, and daughter products) are sufficiently small that the coma may be considered optically thin. The rotational lines of H<sub>2</sub>O, the most abundant volatile, are generally considered to be optically thick in the inner coma (Crovisier 1984, Bockelée-Morvan 1987), but optically thin conditions are considered valid for the near-IR rotation-vibration lines of H<sub>2</sub>O that are of immediate interest to us (Crovisier 1984).

In summary, we assume that excitation is constant throughout the coma and that optically thin conditions apply to near-IR H<sub>2</sub>O lines.

#### 5.4.3. Monte Carlo evaluation

With the above assumptions and simplifications Eq. 5.12 becomes

$$F(v_2) = A \int_{FOV} \frac{Q}{4\pi u(r)} \exp\left[-\int_{r_0}^r \frac{dr}{u(r)\tau}\right] G(\theta, \phi) V_L(r, v_2) \sin(\theta) dr d\theta d\phi. \quad (5.14)$$

An efficient way to evaluate this three-dimensional expression is by Monte Carlo sampling methods. If  $N$  points are selected randomly in a multi-dimensional volume  $V$ , then the integral of a function  $f$  over this volume is estimated by

$$\int f dV = \frac{V}{N} \sum_i f_i \pm \frac{V\sigma}{\sqrt{N}}. \quad (5.15)$$

The error is determined by the number of samples  $N$  and the variance  $\sigma$ . From the many methods available to reduce the variance (see *e.g.*, Kalos and Whitlock 1986) we implemented *importance sampling* in our model. *Importance sampling* states that for

$$q = \int \dots \int B(x_1, x_2, \dots, x_n) dH(x_1, x_2, \dots, x_n), \quad (5.16)$$

where  $H$  is some probability distribution function, if  $(x_1^i, x_2^i, \dots, x_n^i)$  is sampled from  $H$  then  $q$  is estimated from

$$q \sim \frac{1}{N} \sum_i B(x_1^i, x_2^i, \dots, x_n^i) \quad (5.17)$$

with error proportional to  $N^{-1/2}$ . Equation 5.17 provides an efficient way to evaluate Eq.

5.14 if proper  $B$  and  $H$  can be found. If we define

$$\begin{aligned} B(r, \theta, \phi) &= G(\theta, \phi) V_L(r, v_z), \text{ inside the FOV} \\ &= 0, \text{ outside the FOV} \end{aligned} \quad (5.18)$$

and

$$H(r, \theta, \phi) = \left[ 1 - \exp\left(-\int_{r_0}^r \frac{dr}{u(r)\tau}\right) \right] \frac{1 - \cos(\theta)}{2} \frac{\phi}{2\pi} \quad (5.19)$$

then we have

$$dH(r, \theta, \phi) = \frac{1}{4\pi u(r)\tau} \exp\left(-\int_{r_0}^r \frac{dr}{u(r)\tau}\right) dr \sin(\theta) d\theta d\phi, \quad (5.20)$$

and Eq. 5.14 may be written as

$$F(v) = A' \int_{FOV} B dH \quad (5.21)$$

where  $A'$  is a normalization factor. It is easily verified that  $H(r, \theta, \phi)$  is a probability distribution function over the whole spatial space. The spatial coordinates are therefore

sampled as

$$\begin{aligned}\cos(\theta) &= 1 - 2R_1, \\ \phi &= 2\pi R_2, \text{ and} \\ \int_{r_0}^r \frac{dr}{u(r)\tau} &= -\ln(1 - R_3)\end{aligned}\tag{5.22}$$

where  $R_1$ ,  $R_2$ , and  $R_3$  are random numbers uniformly distributed over the range (0,1). Different seeds are used for  $R_1$  and  $R_2$  to insure that they are not correlated. The sampled coordinate is discarded if it is not in the specified FOV.

In theoretical work a single integration of Eq. 5.14 usually suffices to demonstrate a point. For spectral analyses, however, many of the input parameters are unknown or poorly constrained and a spectral model must be used in an iterative mode in order to find "best fit" coma parameters. Our sequence for analyzing an observed spectral line profile is summarized below and illustrated in Fig. 5.2.

*1. Select parameters for a baseline model.* Specific choices include heliocentric and geocentric distances, FOV, production rate, anisotropy factors, outflow velocity, and kinetic temperature. These parameters could be calculated from hydrodynamic equations, fixed by observations, or be just educated guesses.

*2. Sample the spatial coordinates according to Eq. 5.22.* If excitation is not

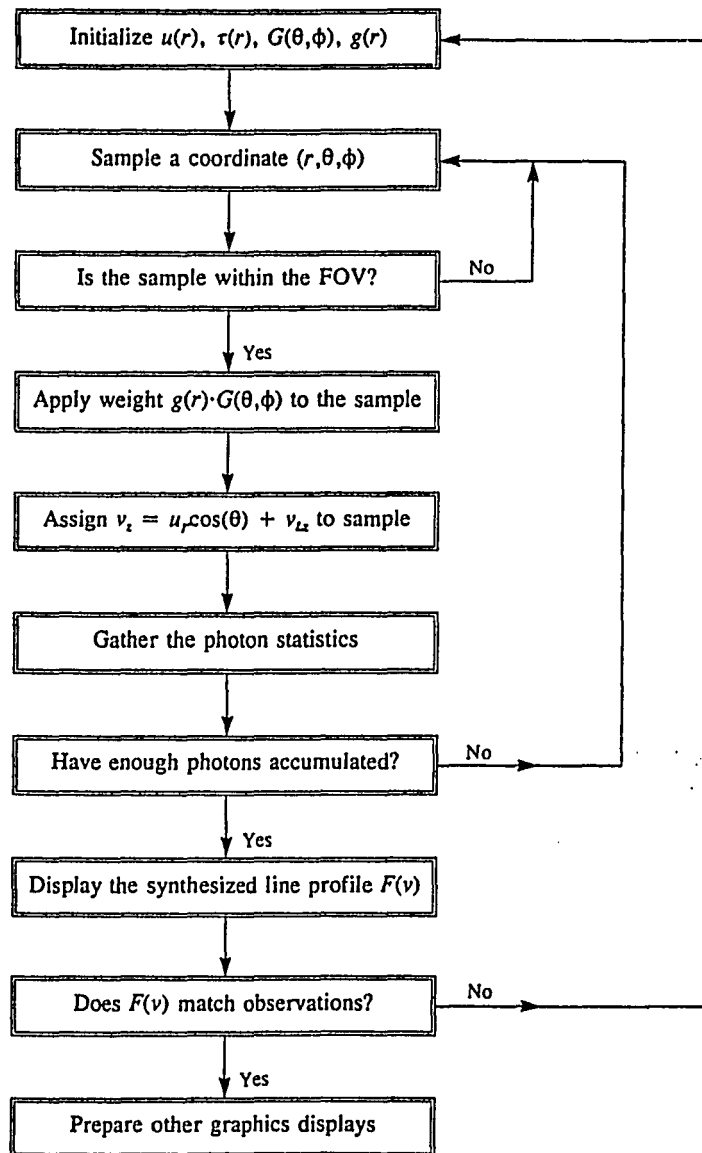


**Figure 5.2.** Block diagram of the spectral outflow model computer program. The cycle time is sufficiently fast that the operator may interact with the program in real time.

constant throughout the coma, the photon emitted at the sampled location would be weighted by an appropriate factor.

3. *Check the FOV.* If the sample at coordinate  $(r, \theta, \phi)$  is not within the FOV it is discarded and Step 2 is repeated.

4. *Apply the anisotropy factor.* The sample is weighted by the factor  $G(\theta, \phi)$ .

5. *Sample the local thermal velocity.* If LTE applies, for example, the local thermal velocity is sampled from a Maxwellian distribution. The Doppler shift is equal to the velocity along the LOS.

6. *Gather the statistics.* The velocity histogram is recorded over the interval  $\pm v_{max}$  which we divided into 100 cells. Each sampled photon is binned according to its Doppler shift along the LOS with weights determined in Steps 2 and 4.

7. *Synthesize the line profile.* Repeat Steps 2 through 6 until enough photons have accumulated in the cells to make the error small.

8. *Compare the histogram with the observed line profile.* If the match is unsatisfactory go back to Step 1 and adjust the model's baseline parameters.

9. *Prepare graphics displays.* Use the fitted three-dimensional density distribution to construct various displays (*e.g.*, a two-dimensional column density map) for direct comparison with non-spectral measurements and calculations.

#### 5.4.4. Uniqueness of Fit

No matter how sophisticated or accurate a model calculation is, its utility for interpretive work is limited because observed cometary line profiles average information along the LOS through the coma, thus setting up uniqueness questions. Resolution of

such problems depends upon awareness of the relative influence of different coma processes on the formation of spectral lines. In the next section, we use our model to illustrate these effects.

## 5.5. Molecular Spectral Line Shapes

The first applications of our model are described in the following chapter. In this section we use the model in a tutorial mode to illustrate the influence of various conditions in the coma on the formation of cometary spectral line profiles. In all cases we ignore instrumental effects. We begin with short descriptions of different gas dynamic models since this choice effectively determines the characteristics of line profiles synthesized with the kinematic model.

### 5.5.1. Comparison of monokinetic and hydrodynamic line profiles

The *monokinetic model* generally assumes collisionless outflow with constant expansion velocity and it ignores the coma temperature. Although these assumptions are frequently criticized as unrealistic, the model remains in widespread use because of its simplicity. Typical monokinetic (or Haser) line shapes are included in Figs. 5.3-5.5. These profiles are distinguished by double peaks, very sharp sides, and symmetry about the rest frequency  $\nu_0$ . *It is significant that no cometary spectral line has ever been observed with all of these characteristics.*

The *hydrodynamic model* recognizes the role of collisions in the coma and describes their consequences with coupled fluidmechanic/photochemical equations. Monokinetic and hydrodynamic line profiles are compared in Fig. 5.3. The smoother

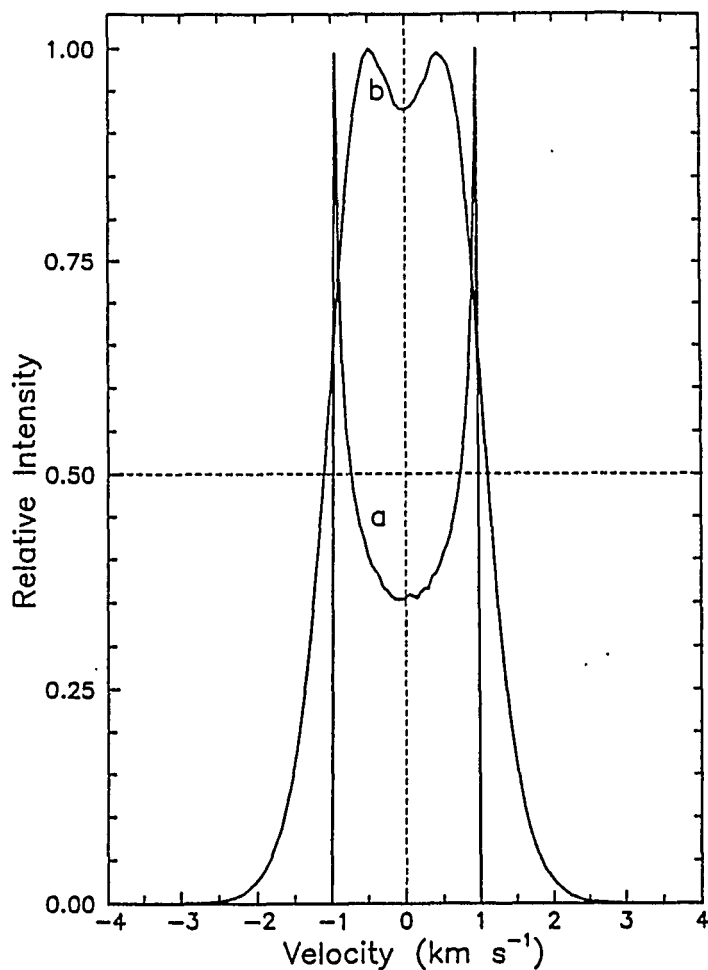


**Figure 5.3.** Comparison of typical monokinetic (*a*) and hydrodynamic (*b*) cometary lines. Both profiles are calculated for isotropic outflow and a circular FOV of radius  $1 \times 10^4$  km. The dramatically different appearance of these profiles is due to different treatment of velocity and temperature in the coma. The radial dependence of velocity and kinetic temperature in the hydrodynamic model are calculated from hydrodynamic equations of the coma for  $Q_{\text{H}_2\text{O}} = 1 \times 10^{30}$  molecules  $\text{sec}^{-1}$  at  $R_n = 1$  AU. The constant expansion velocity in the monokinetic profile is  $1 \text{ km sec}^{-1}$ . The kinetic temperature is not represented in monokinetic profiles.

appearance of the hydrodynamic profile is due to two kinematic properties not represented in the monokinetic model: radial variations in the expansion velocity and velocity dispersion due to collisions. All observed, velocity-resolved cometary lines have high velocity wings similar to the hydrodynamic profile.

For all models we assume a rather active comet ( $Q_{\text{H}_2\text{O}} = 1 \times 10^{30} \text{ sec}^{-1}$ ) in order to stress differences between them. Unless otherwise noted the FOV has a radius of  $1.2 \times 10^4 \text{ km}$  and the heliocentric and geocentric distances are 1 AU. The uniform outflow velocity in the monokinetic model is  $1 \text{ km sec}^{-1}$ . For hydrodynamic line profiles the radial dependence of temperature and velocity is calculated from the hydrodynamic equations in Crovisier (1984) with the treatment of photolytic heating given by Bockelée-Morvan and Crovisier (1987b).

### 5.5.2. Influence of the outflow velocity

The neutral gas expansion velocity is a fundamental coma parameter. It is assumed to be constant in the Haser model, but much evidence demonstrates that the velocity is higher than previous theoretical estimates (*cf.* Delsemme 1982) and that it varies significantly with radial distance, heliocentric distance, and gas production rate. In typical hydrodynamic calculations the outflow velocity rises rapidly to  $\approx 0.8 \text{ km sec}^{-1}$  near the nucleus due to the pressure gradient, stays reasonably constant at  $\approx 1 \text{ km sec}^{-1}$  to  $r \approx 10^3 \text{ km}$ , and increases again in the outer coma. *In situ* velocity measurements in comet P/Halley from *Giotto* (Lämmerzahl *et al.* 1987) confirmed the general predictions of the hydrodynamic model for the region from  $1 \times 10^3$  to  $4 \times 10^4 \text{ km}$ . The outflow velocity is therefore an observable of considerable significance to coma models and a

retrieved velocity curve would clearly be much more useful than just an average value. A particular goal of this work is to demonstrate that kinematic analyses of cometary line profiles can lead to such insight into the outflow velocity, especially in the outer coma where theory becomes inexact and for comets other than Halley where spacecraft measurements will not be available.

Monokinetic lines respond in a particularly simple way to changes in the outflow velocity; illustrative examples are presented in Fig. 5.4. The width of these profiles (the full width measured at the half maximum intensity points relative to the double peaks) is equal to twice the outflow velocity.

The influence of the outflow velocity on hydrodynamic lines is more complicated. The high velocity wings in the hydrodynamic profile in Fig. 5.3 are due in part to larger velocities in the outer coma while its width is proportional to some average measure of the outflow velocity, such as the "plateau region" in typical hydrodynamic velocity curves (*e.g.*, Bockelée-Morvan and Crovisier 1987b). The hydrodynamic profile's width and shape will therefore change according to radial variations in the expansion velocity. In principle, the velocity curve could be retrieved from an observed spectral line if all other coma parameters were known. It is interesting that the widths of the two profiles in Fig. 5.3 are equal to within  $\approx 10\%$  in spite of their different shapes and theoretical basis. Their similarity suggests that model-independent estimates of the outflow velocity may be simply and directly extracted from the observed widths of spectral lines. This relationship has been used in many kinematic analyses, in fact, but we demonstrate below that other coma

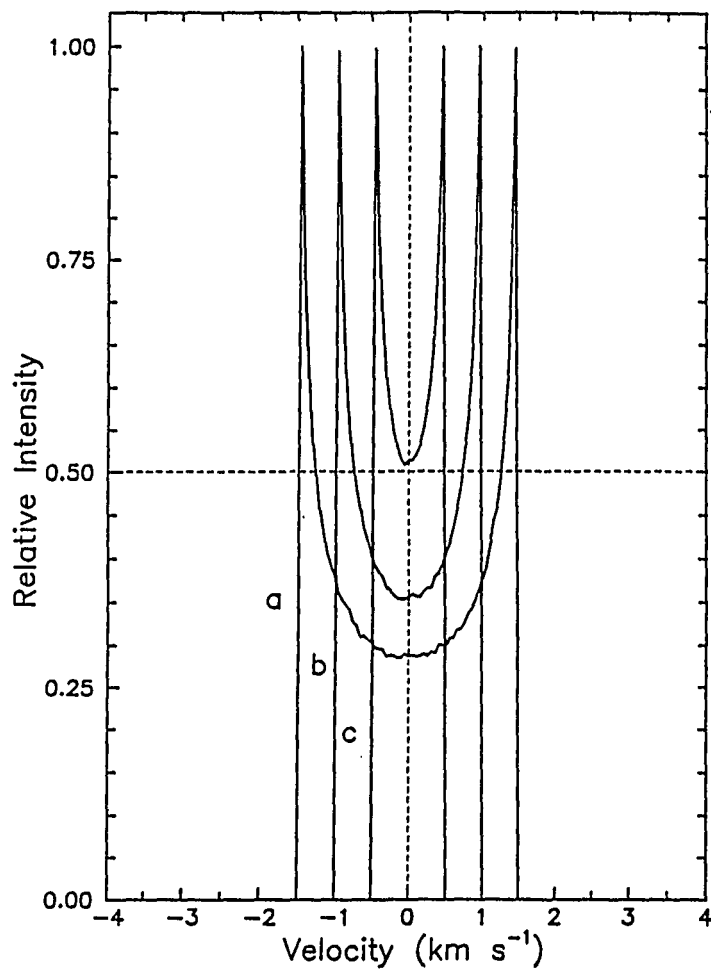


**Figure 5.4.** Illustration of the effect of different expansion velocities on monokinetic profiles. The values are 1.5, 1.0, and 0.5 km sec<sup>-1</sup> for curves *a*, *b*, and *c*, respectively. The line width equals twice the assumed constant expansion velocity.

parameters affect the line width, thus invalidating this type of velocity measurement.

### 5.5.3. Influence of the FOV

For the viewing geometry in Fig. 5.1 the spectrometer's FOV accepts radiation from all molecules moving near the comet-Earth LOS (except those blocked by the nucleus or shielded by optical depth effects) but only a fraction of those with velocity components orthogonal to this axis. The instrumental FOV is therefore an optical velocity filter that affects the shape of recorded spectral lines in important ways. If the size of the FOV is smaller than the scale-length against photodestruction, for example, the velocity histogram will be biased by molecules moving near the LOS. Many of these molecules will have large velocity components  $v_z = u_r \cos(\theta)$  and most will remain in the FOV until they photodissociate. This selection gives rise to the double peaks at high velocities in the monokinetic profiles in Figs. 5.3-5.5, while their abrupt cut-off at  $v_{max} = \pm u_r$  is due to the assumed constant value of the expansion velocity. As the size of the FOV increases (see examples in Fig. 5.5) the double peaks become less pronounced as velocity components from more molecules traveling away from the LOS are included in the central part of the velocity histogram. The width of the monokinetic profile does not change with FOV, however, since that depends only upon  $u_r$ . In observations of the whole coma the monokinetic profile becomes a rectangular function of width  $2u_r$ .

The shape of the hydrodynamic profile is much less sensitive to the FOV (see examples in Fig. 5.6) because dispersion in the velocity field allows significant

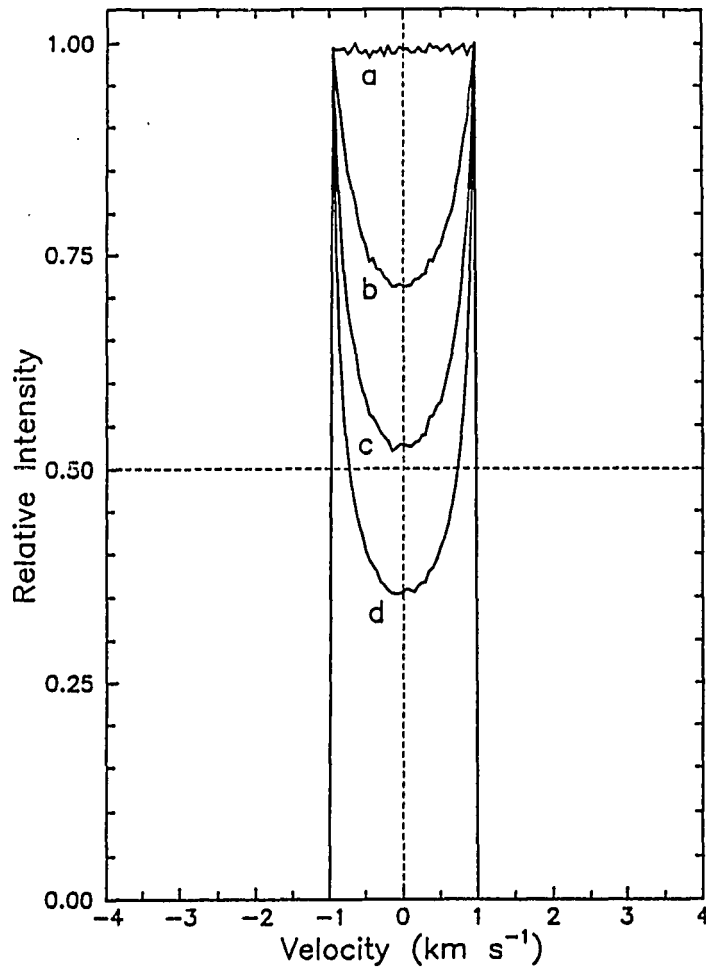


**Figure 5.5.** Illustration of the effect of the FOV on monokinetic line profiles. The rectangular function in curve *a* is the limiting case for observations of the whole coma. The radii of the circular FOV for the other examples are: *b*,  $1 \times 10^5$  km; *c*,  $4 \times 10^4$  km; and *d*,  $1 \times 10^4$  km. The FOV has no effect on the width of monokinetic profiles although the shape changes dramatically.

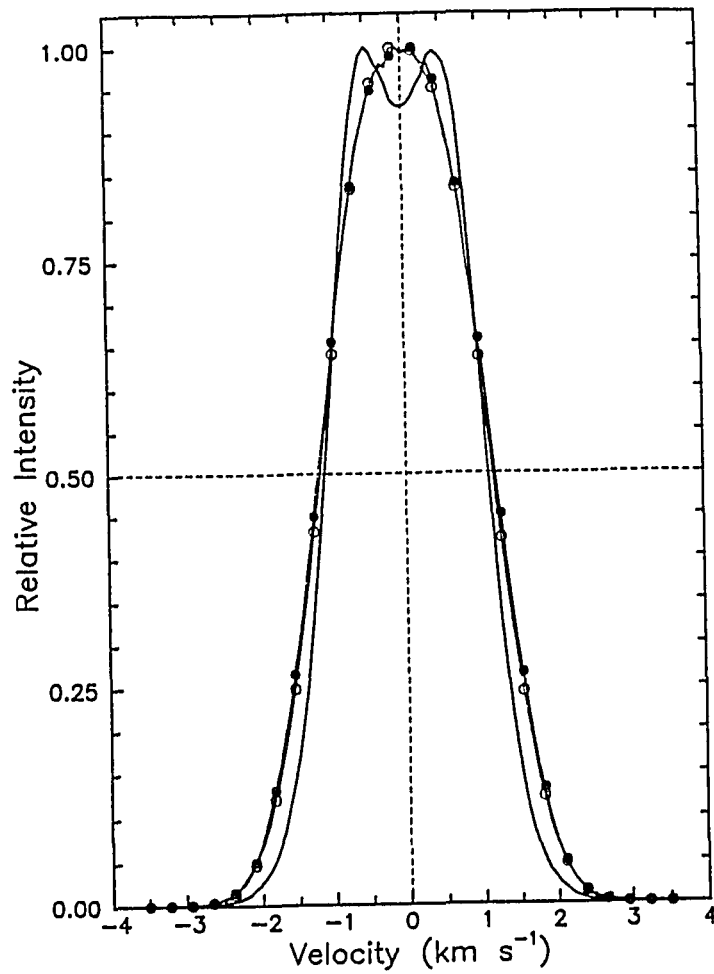


**Figure 5.6.** Illustration of the effect of the FOV on hydrodynamic line profiles. *Solid curve without symbols:* radius of  $1 \times 10^4$  km. *Curve with open symbols:* radius equal to the scalelength of  $\text{H}_2\text{O}$ . *Curve with solid symbols:* observations of the whole coma. Both the width and shape of the hydrodynamic profile depend upon the FOV although the changes are not very large.

contribution to the central portion of the velocity histogram even when the FOV is small compared to the scale-length against photodestruction. As the dimension of the FOV approaches the scale-length the hydrodynamic line broadens slightly (<10%) and loses its double peaks. Additional changes are negligible when the FOV is further enlarged to include the whole coma.

#### *5.5.4. Influence of anisotropic outflow*

Observations leave no doubt that asymmetric outflow exists in comets, consistent with vaporization models of cometary nuclei that predict outflow predominantly in the sunward direction. Consequently, the Sun-comet-Earth (or phase) angle will influence cometary spectral lines independent of conditions in the coma itself. We control the outflow distribution in our model with the weight factor  $G(\theta, \phi)$ . For symmetric distributions  $G(\theta, \phi) = 1$ , the average of all velocity components along the LOS is zero and no frequency shift appears in the line profile. If  $G(\theta, \phi)$  concentrates the outflow towards Earth, however, a net blue-shift is impressed on the spectral line. Conversely, if  $G(\theta, \phi)$  specifies an outflow distribution away from Earth, a net red-shift would be observed. No parameter in our model other than  $G(\theta, \phi)$  is capable of producing a line shift. The absolute positions of cometary spectral lines are therefore important signatures of asymmetric outflow, but there are additional consequences. In Fig. 5.7 we present hydrodynamic line profiles synthesized with various non-uniform outflow distributions into the Sun-facing hemisphere for a phase angle of  $60^\circ$ . Changes relative to the isotropic hydrodynamic line profile include velocity shifts from the transition's rest frequency, decreases in width up to 50%, and the appearance of asymmetry in the

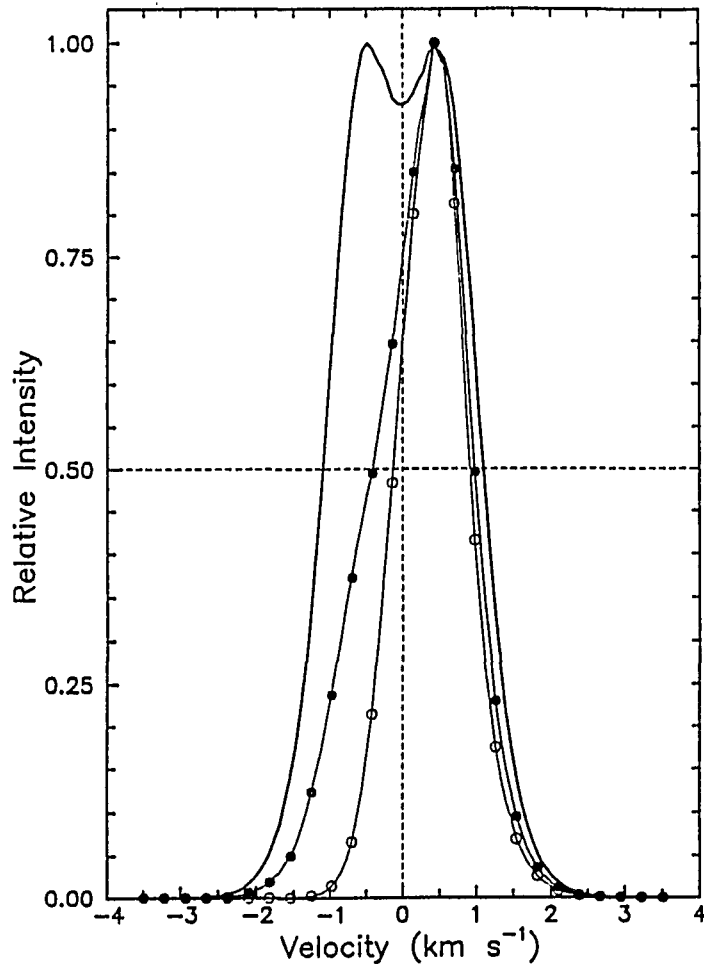


**Figure 5.7.** Illustration of the effect of asymmetric outflow on hydrodynamic line profiles. The Sun-comet-Earth angle in each example is  $60^\circ$ . The curve without symbols for isotropic outflow ( $\alpha = 1$ ,  $\beta = 0$ ) establishes a reference profile for the two anisotropic distributions. *Curve with solid symbols:*  $\alpha = 0.3$ ,  $\beta = 1.0$ ,  $\cos^2(\theta)$  distribution centered along the comet-Sun axis. *Curve with open symbols:*  $\alpha = 0$ ,  $\beta = 1$ ,  $\cos^2(\theta)$  distribution. The most obvious signatures of anisotropic outflow are line shifts from rest values and reduced line widths. The line shift is an excellent indication of anisotropy. The line width may be affected by kinematic parameters other than anisotropy, but a very small value would be diagnostic of outflow in narrow jets.

line shape. These differences are due entirely to the reduced number of molecules flowing into the nightside hemisphere, hence fewer negative velocity components contribute to the velocity histogram. Other asymmetric spatial distributions would affect the position, width, and shape of cometary spectral lines in different ways than are illustrated in Fig. 5.7. For comets with thick refractory mantles, such as Halley apparently had, the outflow may include and even be dominated by jets, an important special case of asymmetric outflow. The strong directional properties and limited velocity dispersion in jets will lead to very narrow, Doppler-shifted spectral line profiles. In principle, therefore, reasonably detailed descriptions of anisotropy in the coma can be retrieved from observed line profiles if other parameters are tightly constrained. Since asymmetric outflow affects the widths of cometary spectral lines, however, a measurement of only the outflow velocity or the spatial distribution from an observed line profile is not safe even as an estimate. *The velocity field and density distribution are coupled parameters whose retrieval requires a comprehensive kinematic model.*

#### *5.5.5. Influence of the kinetic temperature*

The hydrodynamic profile has a built-in radial temperature dependence so collisional broadening is already present in the examples in Figs. 5.3, 5.6, and 5.7. If this feature is turned off (*i.e.*,  $T = 0$  °K, see Fig. 5.8) the hydrodynamic line acquires the pronounced double peaks and much sharper edges that are reminiscent of the monokinetic profile in Fig. 5.3. A comparison of the two profiles in Fig. 5.8 demonstrates that the smoothing effect of collisional broadening has more influence on

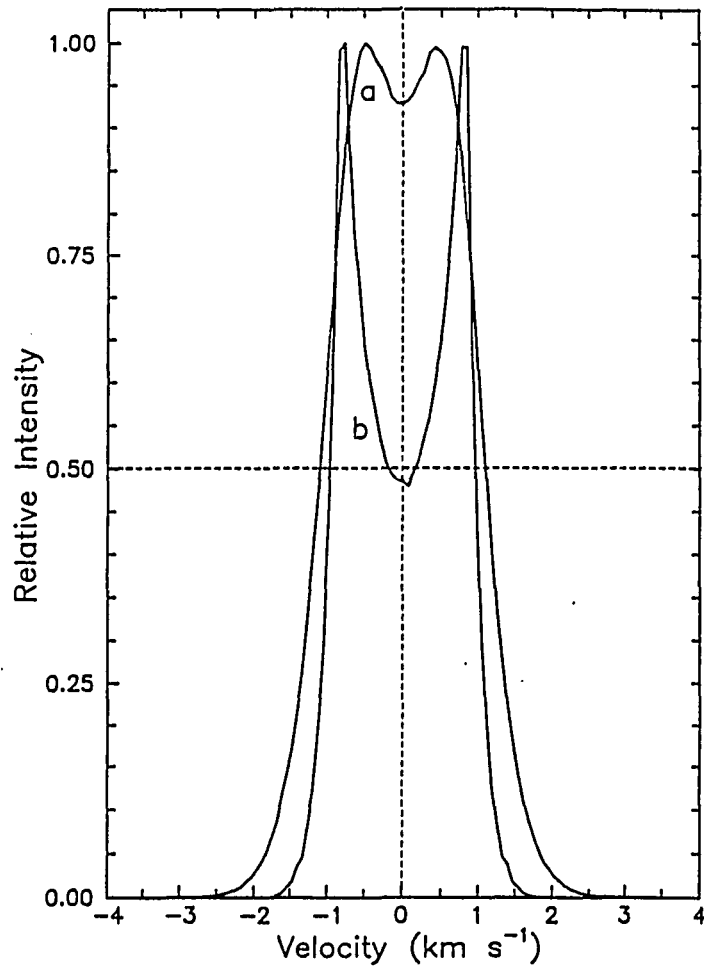


**Figure 5.8.** Effect of the coma kinetic temperature on hydrodynamic line profiles. *Curve a*: the normal hydrodynamic line profile in which the temperature is obtained from solving hydrodynamic equations of the coma. *Curve b*: hydrodynamic line profiles in which the temperature is forced to 0 °K. Although the widths of these profiles are unchanged, their significantly different shapes illustrate the important smoothing effect of collisions in the inner coma. The hydrodynamic line in (*b*) does not revert completely to the monokinetic profile because of radial variations in the expansion velocity.

the hydrodynamic line shape than radial variations in the expansion velocity.

We added thermal broadening to the monokinetic model with a Maxwellian velocity distribution for constant coma temperature  $T_c$ . Examples of thermally-broadened monokinetic line profiles are included in Fig. 5.9. Substantial smoothing occurs. The double peaks disappear, the profiles become slightly wider, and they acquire high velocity wings. The net result of adding velocity dispersion in this manner to monokinetic profiles is to render them similar in appearance to hydrodynamic lines. Although the effect of collisional broadening appears to blur the distinction between monokinetic and hydrodynamic line profiles, the hydrodynamic treatment of the radial dependence of velocity and temperature in the coma is still preferable to assumed constant values that have much less interpretive value.

## 5.6. Summary

Velocity-resolved molecular line profiles contain much information concerning physical characteristics of cometary comae but two conditions must be met in order to extract it: knowledge of the influence of individual coma processes on the formation of molecular line profiles and a spectral outflow model to synthesize spectral lines for comparison with observations. We addressed both requirements in this chapter. The basic mechanism that forms cometary spectral lines is very simple, *i.e.*, a superposition of Doppler-shifted velocity components, but the observed velocity field is dependent upon multiple processes in the coma (expansion velocity, collisions, gas production at the surface, recondensation of  $H_2O$ , *etc.*) and the viewing geometry during observations.

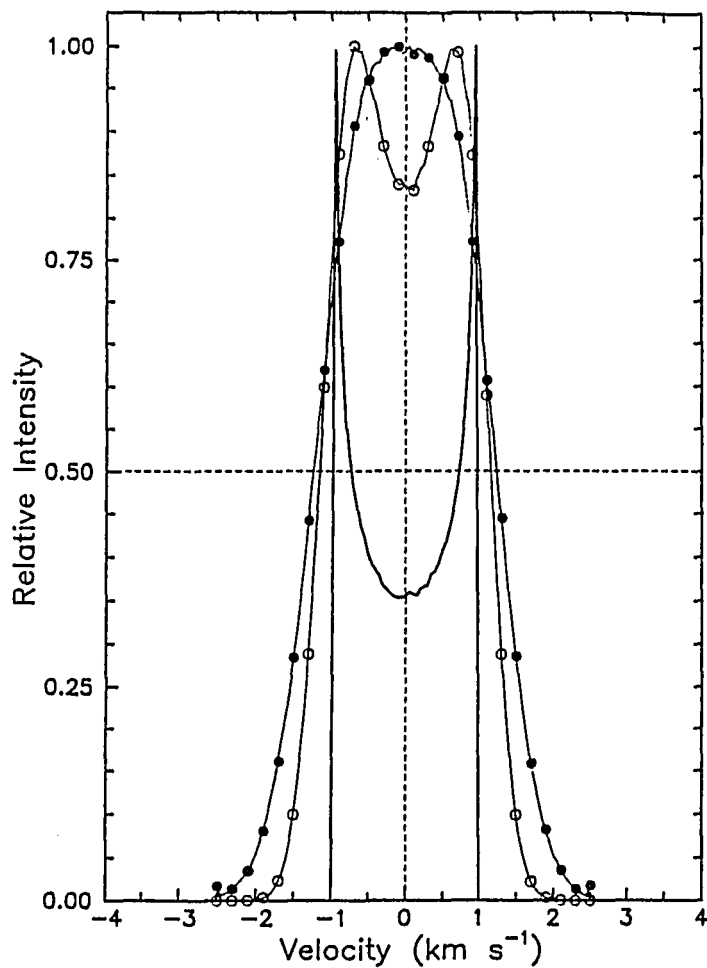


**Figure 5.9.** Effect of adding collisional broadening to monokinetic line profiles. *Curve without symbols:* traditional monokinetic profile at  $T_c = 0$  °K. *Curve with open symbols:*  $T_c = 100$  °K. *Curve with solid symbols:*  $T_c = 300$  °K. The line widths increase only slightly with temperature but the line shapes change dramatically with the velocity dispersion acquired by collisions.

In this chapter we demonstrated that it is possible to treat each of these conditions analytically and in the next chapter we use this model to generate detailed descriptions of the comae of comets Halley and Wilson. Some of the generalized results of our parameter study are summarized below.

### 5.6.1. Cometary spectral line shapes

The sharp, double-peaked profiles associated with Haser-type outflow contrast dramatically with observed cometary lines that are generally smooth with Gaussian-like shapes (see *e.g.*, Chapter 6 or Schloerb *et al.* 1987a). The presence of double peaks in a cometary spectral line is readily understood as a consequence of the size of the FOV used in the observations. The FOV acts as an optical velocity filter that preferentially selects molecules in a cylindrical volume along the LOS through the coma. For spherically symmetric outflow the FOV samples an equal number of molecules approaching and receding from Earth, hence the characteristic double peaks in the Haser profiles in Fig. 5.4 and their vestigial presence in the hydrodynamic profile in Fig. 5.6. No observed cometary spectral line shows comparable double-peak structure, however. In our parameter study we identified three factors that could generate smooth cometary line shapes. One is local thermal motion characterized by the coma kinetic temperature  $T_c$ . As illustrated in Fig. 5.9 even the exaggerated double peaks of the Haser profile may disappear when kinetic temperature is included in the model. A degree of line profile smoothing also results from radial variations in the expansion velocity, particularly in the tendency of hydrodynamic velocity curves to add high velocity wings to spectral line profiles. Asymmetric outflow could also make a

line profile appear smoother by reducing the number of velocity components contributing to one of the high velocity peaks. Another possible smoothing mechanism that we did not explore in this chapter is velocity dispersion due to small lateral components in the expanding gas. Since most observed lines are single-peaked, the influence of one or more of these smoothing processes is indicated. Since the coma kinetic temperature is cool ( $T_c \leq 60$  °K, see *e.g.*, Bockelée-Morvan and Crovisier 1987a, Weaver *et al.* 1987), insufficient smoothing is available from kinetic temperature alone. It therefore appears that multiple processes influence the shape of cometary spectral lines: the FOV which introduces velocity structure (unless the whole coma is observed) and some combination of thermal motion, radial expansion, and spatial anisotropy that smooths the profile to a Gaussian-like shape.

### 5.6.2. Cometary spectral line widths

In the preceding section we noted that the coma kinetic temperature can significantly alter the shape of a cometary spectral line, but examination of Figs. 5.8 and 9 reveals that the line width is not affected very much ( $\approx 10\%$ ). Our parameter study indicates that asymmetric outflow and the expansion velocity have much more influence on line width than does kinetic temperature. Moreover, these two conditions have opposite effects on the line width: the width increases with the expansion velocity (see Fig. 5.4) but it decreases for anisotropic outflow (see Fig. 5.7). Thus, if the width of an observed line is very large the most likely explanation is high outflow velocity, while a very narrow observed line implies pronounced asymmetry in the outflow. Intermediate cases require more judgement in the use of the outflow model but,

fortunately, anisotropy has another spectral signature (line shift) that allows these two competing line broadening mechanisms to be distinguished.

### *5.6.3. Cometary spectral line positions*

Observed cometary spectral lines are frequently shifted from their rest frequencies after subtraction of geocentric and topocentric velocity components. The generally small ( $<1 \text{ km sec}^{-1}$ ) red or blue cometocentric line shifts are diagnostic of asymmetric outflow into the coma. No other parameter in our model produces line shifts although there may be processes in the coma not represented in our current model (*e.g.*, optical depth effects) that could also contribute to a line shift. The sign and magnitude of these cometocentric line shifts are determined by several conditions in the coma including the type of asymmetric outflow (*e.g.*, jets), its direction relative to the LOS, and the expansion velocity. A meaningful interpretation of an observed line shift therefore requires an outflow model that treats all of these factors realistically.

### *5.6.4. Relevance of the Haser model*

Since the Haser outflow model is frequently used to analyze spectral data we included monokinetic line profiles in our parameter study, but the results serve primarily to illustrate the limitations of this model. None of the distinguishing features of monokinetic line profiles (double peaks, sharp sides, unshifted positions) are supported with high resolution spectroscopic observations of comets. This failing alone invalidates its basic assumption of spherically symmetric outflow at uniform expansion velocity. An additional shortcoming of the monokinetic model is its neglect of local thermal motion. The coma kinetic temperature has a significant smoothing effect on the

formation of cometary spectral lines that is not represented in monokinetic models.

#### 5.6.5. Comparison of this work to other models

We divide interpretations of velocity-resolved cometary spectral line profiles into three categories. The first group includes results based on an assumed unique relationship between a particular line profile parameter and a specific kinematic parameter of the coma. The most notable example of this association is the intuitive assumption used by many authors that the outflow velocity is equal to one half of the observed line width (see *e.g.*, analyses in Despois *et al.* 1981, Larson *et al.* 1987, Schloerb *et al.* 1987a). The second group comprises results obtained by using gas dynamic models to produce some kind of spectral line profile as output for comparison with observations. An example is Combi's (1989) use of his dusty-gas-dynamic/Monte Carlo model to match the width of radio HCN lines. The third group of kinematic analyses uses spectral outflow models to estimate coma parameters through various fitting procedures. This method was used by Bockelée-Morvan and Gérard (1984), Tacconi-Garman (1989), and Bockelée-Morvan *et al.* (1990) and it is also the approach used in this study. We restrict subsequent discussion to this last group because of its primary emphasis on the interpretation of observed spectral lines.

We summarize in Table 5.2 the major characteristics of the relatively few spectral outflow models that have actually been applied to observational data. We include Combi's (1989) gas dynamic model for comparison because it was used to fit some aspects of radio HCN spectral lines. These models differ in many ways, the most obvious being whether they apply to parent or daughter molecules. Until recently, radio

Table 5.2. Summary of Spectral Outflow Models of Cometary Comae

	Bockelee-Morvan and Gerard 1984	Combi 1989	Tacconi-Garman 1989	Bockelee-Morvan <i>et al.</i> 1990	This thesis
<b>TYPE OF MODEL</b>	MCPT*	MCPT/gas dynamic	MCPT	Haser	Analytic/MC sampling
<b>COMA DESCRIPTION</b>					
Species	OH	HCN	OH	OH	H <sub>2</sub> O
Outflow distribution	Asymmetric (cones)	Spherically symmetric	Asymmetric (day/night)	Spherically symmetric	Quasi-3D
Parent outflow velocity	Constant	Non-uniform	Constant	Constant	Non-uniform
Parent thermal velocity	Yes	Yes	Yes	No	Yes
Daughter velocity	Vectorial	N/A	Vectorial	Vectorial	N/A
<b>FITTING PROCEDURE</b>					
Criterion	Reproduce line shape by iterative parameter adjustment	Reproduce line width	Reproduce line shape by iterative parameter adjustment	Fit trapezoid to line shape by least squares fit	Reproduce line shape by iterative parameter adjustment
Calculation method	MCPT/statistical average	MCPT/statistical average	MCPT/statistical average	Trapezoid	Integration by Monte Carlo sampling
<b>RETRIEVABLE PARAMETERS</b>					
Velocity	Yes (single value)	Yes (single value)	Yes (single value)	Yes (single value)	Yes (radial profile)
Temperature	No	No	No	No	Yes
Anisotropy	Yes	No	Yes (day/night only)	No	Yes

\*Monte Carlo particle trajectory method

observations of OH were the only data suitable for kinematic analyses, hence the dominance of OH spectral outflow models in Table 5.2 in spite of their greater complexity. Only two entries in Table 5.2, including this study, deal with parent molecule spectra. Another important distinction between the models in Table 5.2 is the way in which gas dynamic principles are implemented. The complex nature of daughter product outflow models reveals itself, for example, in the simplifying assumptions used to characterize the parent molecular outflow. For example, all of the OH models in Table 5.2 assume constant H<sub>2</sub>O outflow velocity. Our parent molecule outflow model not only accommodates non-uniform outflow velocity, as also does Combi's, but our method is unique among the entries in Table 5.2 in its ability to retrieve a *radial velocity profile* from observations (Chapter 6) rather than a single average value. The models in Table 5.2 also differ significantly in their ability to represent spatial anisotropy in the density distribution. The possibilities range from none (Combi 1989, Bockelée-Morvan *et al.* 1990) to our quasi-3D treatment. The consequences are that some models (*e.g.*, Bockelée-Morvan and Gérard 1984, Tacconi-Garman 1989, this work) can synthesize a variety of line shapes while others are restricted to specific types (trapezoids, Bockelée-Morvan *et al.* 1990; Gaussian-like profiles, Combi 1989). In general, our outflow model represents a combination of mathematical simplicity, versatility, and realism for exploiting the full information content of velocity-resolved parent molecule spectra.

## CHAPTER 6

### APPLICATION TO OBSERVATIONS

#### 6.1. Introduction

One of the primary goals in remote spectral studies of comets is to increase knowledge of the chemical composition of cometary matter through the identification of new molecular species. Another important objective is to use known constituents to characterize physical conditions in the coma. Specific tasks include the determination of production rates, photochemical lifetimes, expansion velocities, kinetic temperatures, and spatial distributions. The kinematic properties of the coma, particularly those associated with parent molecules, were poorly constrained by observations prior to comet Halley's last apparition. The most direct tracers of outflow in the coma are parent molecules, of course, but just detecting them remains one of the major challenges of cometary astronomy. Kinematic conditions may also be deduced from studies of daughter molecules but the interpretations are necessarily more complex and the retrieved parameters are more sensitive to the approximations and uncertainties in the model. In either case, kinematic studies impose stringent demands on the type and quality of spectroscopic data necessary to support them. Ideally, spectra with both high spectral and high spatial resolution are desirable in order to use the positions and shapes of spectral lines as remote signatures of physical conditions in the coma. Such data do not yet exist, but observations with sufficient spectral resolution for kinematic analyses have now been acquired for radio lines of OH and HCN and IR transitions in H<sub>2</sub>O. In

this paper we use velocity-resolved ( $\lambda/\Delta\lambda$  up to  $3 \times 10^5$ ) spectral line profiles of  $\text{H}_2\text{O}$  to deduce the spatial distribution and velocity field of the neutral gas in comets P/Halley and Wilson (1987 VII). The results extend previous kinematic analyses of these spectra (Larson *et al.* 1987, 1989; hereafter L87 and L89, respectively) through more elaborate treatment of the data and use of the anisotropic outflow model described in the preceding chapter. We synthesized cometary spectral line profiles with this model in order to reproduce the positions, widths, and shapes of the observed  $\text{H}_2\text{O}$  lines. The kinematic parameters in these fits are compared to *in situ* measurements made from the *Giotto* and *Vega* spacecraft, to values derived from other Earth-based observations, and to predictions of outflow models developed by other authors.

## 6.2. Observations and Data Analysis

High resolution spectra of  $\text{H}_2\text{O}$  in comets (the  $\nu_3$  band at  $2.65 \mu\text{m}$ ) were recorded at the NASA *Kuiper Airborne Observatory (KAO)* with the University of Arizona Fourier transform spectrometer (FTS) (Davis *et al.* 1980) on the three occasions summarized in Table 6.1. Examples of the cometary  $\text{H}_2\text{O}$  spectra are included in Fig. 6.1; additional details concerning the observations and their calibrations may be found in L87 and L89. The four distinct numerical operations used in our analysis are reviewed below.

### 6.2.1. Line Profile Averaging

We calculated an average  $\text{H}_2\text{O}$  line profile for each of the three observed cometary spectra using the measured absolute positions of the individual  $\text{H}_2\text{O}$  lines as

**Table 6.1.** Airborne IR observations of H<sub>2</sub>O in comets.

Comet	Date	Resolution (km sec <sup>-1</sup> )	$\Delta^1$ (AU)	R <sub>h</sub> (AU)	FOV (10 <sup>4</sup> km)	Q <sub>p</sub> (10 <sup>29</sup> sec <sup>-1</sup> )
Halley	1985 Dec 24.1	3.2	1.0	1.13	3.0	2.2
Halley	1986 Mar 22.7	3.2	0.74	1.03	2.2	9.1
Wilson	1987 Apr 12.7	3.2	0.94	1.21	2.8	2.6

<sup>1</sup> $\Delta$ : heliocentric distance.

fiducial marks for coadding their profiles and the observed line intensities as weights. The single H<sub>2</sub>O profile representing each comet observation therefore has a higher signal-to-noise ratio (SNR) than any individual line, an important consideration for revealing subtle details and for the successful application of deconvolution techniques. Implicit in this procedure is the assumption that all observed cometary H<sub>2</sub>O transitions have the same line shape. This is a reasonable prospect if the observed line shapes are equally affected by radiative and collisional processes in the coma. The weighted averages are dominated by the four lines at 3749.3, 3779.5, 3801.4, and 3807.0 cm<sup>-1</sup> that involve only the lowest lying ortho (1<sub>10</sub> and 1<sub>01</sub>) and para (0<sub>00</sub>) energy levels. In fluorescence equilibrium only the ortho 1<sub>01</sub> and para 0<sub>00</sub> levels would be populated because of rotational relaxation and, consequently, only the lines at 3779.5 and 3801.4 cm<sup>-1</sup> would have been observed. Since the natural line widths for spontaneous decay to these levels are very small ( $\Delta\nu/\nu \approx 10^{-14}$ ) compared to the Doppler width acquired from motion in the coma ( $\Delta\nu/\nu \approx 3 \times 10^{-6}$ ), IR fluorescence should not generate different

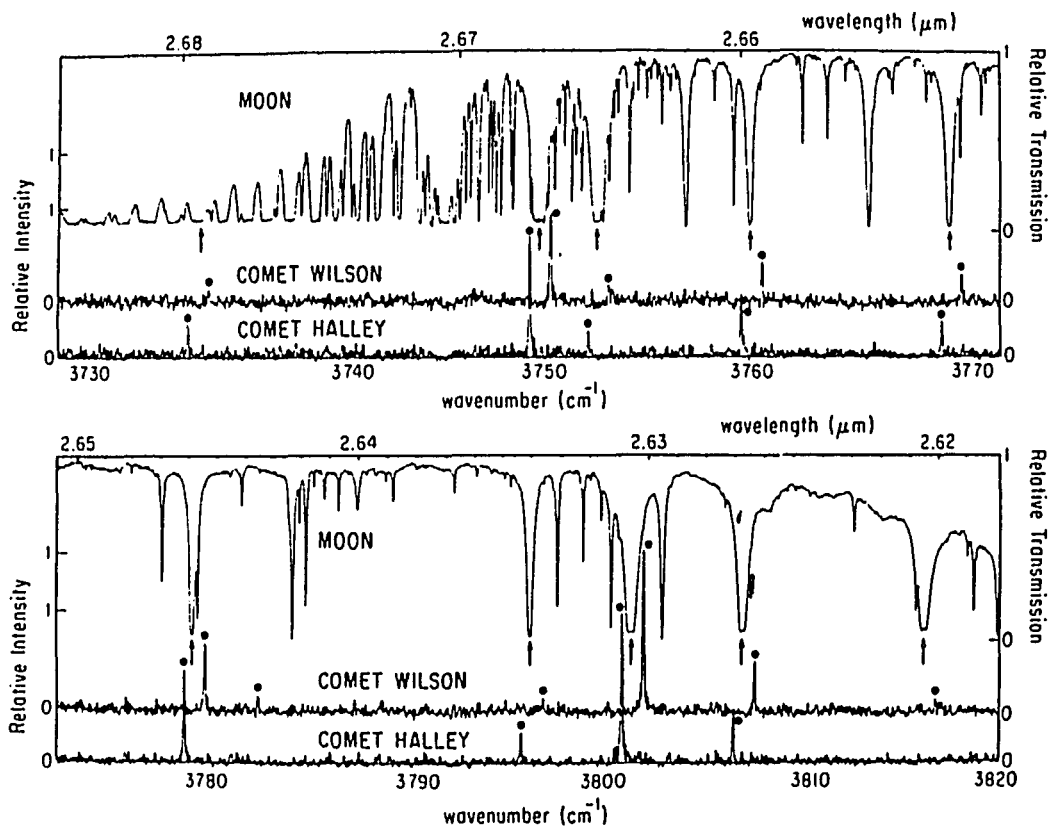


Figure 6.1. Solid symbols mark the cometary  $\text{H}_2\text{O}$  lines and arrows in the lunar comparison spectrum identify the corresponding  $\text{H}_2\text{O}$  transitions in Earth's atmosphere. The wide separation of cometary and telluric lines is due to the comets' large geocentric radial velocities ( $35 \text{ km sec}^{-1}$  for Halley,  $-44 \text{ km sec}^{-1}$  for Wilson). The small number of cometary  $\text{H}_2\text{O}$  lines, relative to the large number of telluric absorption lines (due to thermal excitation at  $\sim 220 \text{ }^\circ\text{K}$ ) indicates rotational relaxation in the coma.

observed line shapes. The number and relative intensities of the H<sub>2</sub>O lines observed in comet P/Halley do not represent pure fluorescence equilibrium (Weaver *et al.* 1987, Bockelée-Morvan and Crovisier 1987a), however, so it is necessary to examine whether collisional excitation could affect the line shape. In the collision zone the relative energy level populations are established by a Boltzmann distribution for temperatures that could vary between 20-200 °K with radial distance. Calculations demonstrate that throughout this region the relative populations of the three levels listed above are high (Bockelée-Morvan 1987). Lines involving these levels will therefore have similar thermal profiles ( $\Delta\nu/\nu < 2 \times 10^{-6}$  for  $T < 200$  °K) that are narrower than the Doppler widths ( $\Delta\nu/\nu \approx 3 \times 10^{-6}$ ) acquired from velocity dispersion in the coma. Thus, we do not expect different shapes among the observed H<sub>2</sub>O lines for collisional excitation either. As a check we superimposed the strong H<sub>2</sub>O line profiles in each spectrum to look visually for line shape differences, but none were found within the noise levels.

The cometary H<sub>2</sub>O lines were observed through the wings of telluric H<sub>2</sub>O lines. Variable atmospheric transmission across each cometary line could therefore alter its shape and position according to the strength of the corresponding transition in absorption in Earth's atmosphere. The effects would be small in our comet spectra because the large geocentric Doppler shifts (see Table 6.1) placed the cometary lines on the far wings of telluric lines (see Fig. 2 in L87). The telluric H<sub>2</sub>O lines were resolved in the lunar spectra ( $R \leq 0.04$  cm<sup>-1</sup>) and the cometary lines were either resolved or very close to it. We therefore searched for line profile variations due to atmospheric transmission by ratioing the cometary observations with lunar comparison spectra and remeasuring

the positions and widths of individual H<sub>2</sub>O lines. No systematic differences between the observed and ratioed cometary H<sub>2</sub>O line profiles were found. We used only the observed cometary H<sub>2</sub>O lines in our analysis because the ratio calculation adds a small amount of noise to the comet data without providing any compensating advantage.

### 6.2.2. Deconvolution

We used the maximum entropy algorithm (see *e.g.*, Gull and Skilling 1984) to retrieve the cometary line profile  $F(\nu)$  from

$$F_{obs}(\nu) = \int F(\nu') I(\nu - \nu') d\nu' \quad (6.1)$$

where  $F_{obs}(\nu)$  is the observed (averaged) H<sub>2</sub>O line profile,  $I(\nu)$  is the instrumental line shape (ILS) for the FTS, and  $\nu$  is wavenumber (cm<sup>-1</sup>). This method requires minimum assumptions concerning the shape  $F(\nu)$  of the cometary line but the ability to retrieve  $F(\nu)$  in any deconvolution method is very dependent upon knowledge of the ILS *under experimental conditions*. One strength of the Fourier method is its predictable ILS:  $I(\nu) = \sin(\nu)/\nu \equiv \text{sinc}(\nu)$  (unapodized). It cannot be assumed that a real FTS will necessarily generate this theoretical profile, however, because factors in its design, alignment, and operating environment could lead to distortions. We assess the fidelity of the ILS of our FTS in several ways. First, prior to a flight program we record emission line profiles using hollow cathode lamps to check on spectrometer performance (see Figs. 18, 21 and 25 in Davis *et al.* [1980] for typical examples of line shapes at  $R < 0.1 \text{ cm}^{-1}$  in laboratory tests and during engineering flights on the *KAO*). Second,

the ILS is displayed directly in our preperihelion observations of comet P/Halley. The observed cometary H<sub>2</sub>O line profile in Fig. 6.2 (solid curve without symbols) is essentially unresolved and therefore displays the ILS in actual astronomical data. The ILS representing theoretical instrumental response at the achieved spectral resolution of 0.04 cm<sup>-1</sup> is included in Fig. 6.2 for comparison (curve with open symbols). The close similarity between the observed and calculated profiles demonstrates the fidelity with which this FTS can record astronomical data over periods of several hours in the presence of mechanical vibrations, electromagnetic interference, and high acoustic noise levels that are part of the airborne environment. Finally, following our airborne observations of comets Halley and Wilson we conducted laboratory tests to confirm the reproducibility of the ILS and the accuracy of its absolute wavelength calibration. The FTS was used daily for several weeks to record numerous Ne emission line spectra. Two operators acquired and processed data independently. The absolute Ne line positions from each series of spectra were compared with absolute wavelength standards to search for systematic differences that could be attributed to the FTS, its operator, or to data processing procedures. None were found, a demonstration that is important to using the cometocentric velocity measurements in L87 and L89 as observational constraints to the outflow distributions presented in this paper.

### *6.2.3. Spectrum Synthesis*

We used our spectral outflow model to synthesize cometary spectral line profiles that provided "best fits" to the deconvolved H<sub>2</sub>O lines. We explored spatial distributions ranging from single jets to superpositions of different outflow patterns

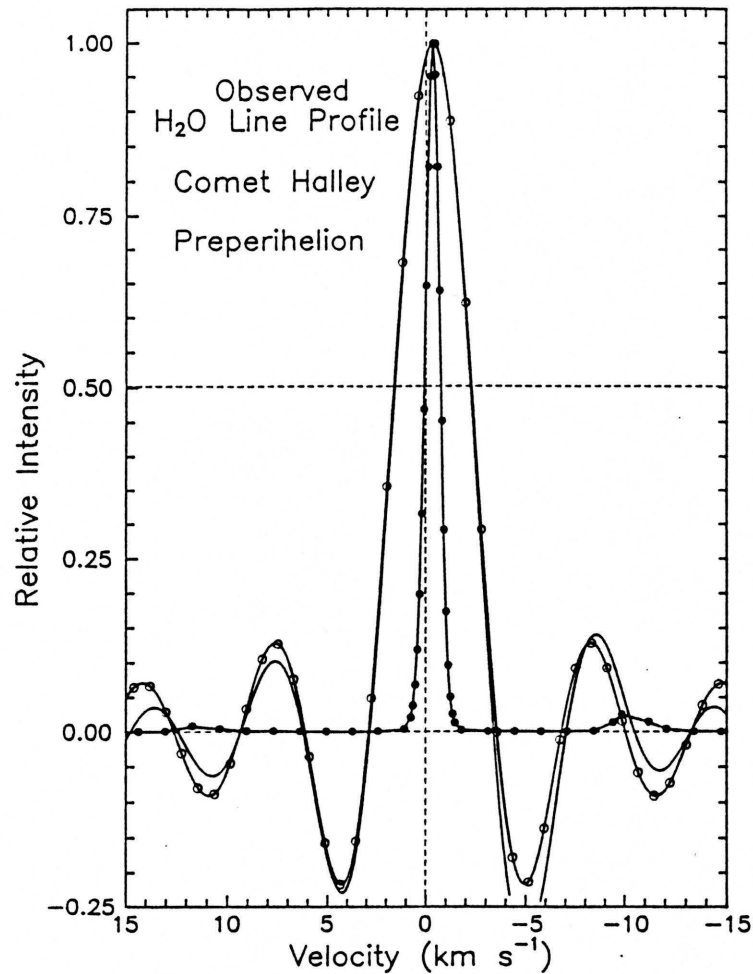


**Figure 6.2.** The H<sub>2</sub>O line profile in comet P/Halley preperihelion. *Curve without symbols:* the observed "average" line profile obtained by coadding the individual lines in the spectrum in Fig. 6.1. *Curve with open symbols:* the theoretical instrumental line shape (unapodized) for the FTS (only the first 4 side lobes on either side of the main peak are shown). The presence of similar side lobes in the observed profile indicates that the lines were unresolved. *Curve with solid symbols:* the deconvolved cometary line profile from which artifacts of the instrumental line shape have been removed.

(e.g., multiple jets, non-uniform outflow into cones and hemispheres, and isotropic outflow). We used functions  $\cos^n \theta$  rather than geometric cones to simulate non-uniform outflow components in the model. High values of  $n$  (15 to 25) generate narrow, jet-like features while lower values give various degrees of non-uniform outflow into a hemisphere (see Fig. 6.3). Other parameters in the model were fixed by the observing conditions (see Table 6.1) and hydrodynamic equations of the coma. Thus, the only adjustable parameters were the number and type of outflow components if we used the "standard" set of hydrodynamic equations in the spectral outflow model to calculate the radial dependence of density, outflow velocity, and kinetic temperature. When the model failed to match the observations for all conceivable spatial distributions, we adjusted the outflow velocity profile empirically to improve the fit. No other coma parameter affects the width of synthesized line profiles as much for reasonable departures from calculated values. For this reason we did not alter the temperature profile from hydrodynamic calculations. The kinetic temperature varies with  $r$  because of adiabatic cooling in the inner coma and photolytic heating and radiative cooling in the outer coma. The predicted net effect of these competing processes is a temperature distribution that varies rapidly for  $r < 10^3$  km and becomes reasonably constant, and low, at larger  $r$  (Bockelée-Morvan and Crovisier 1987a). The average kinetic temperature deduced from airborne observations of H<sub>2</sub>O was  $\approx 50$  °K (Weaver *et al.* 1987, Bockelée-Morvan 1987). The synthesized H<sub>2</sub>O line widths cannot, therefore, be significantly altered by varying the kinetic temperature by small factors about its low observed value (see Fig. 5.8).

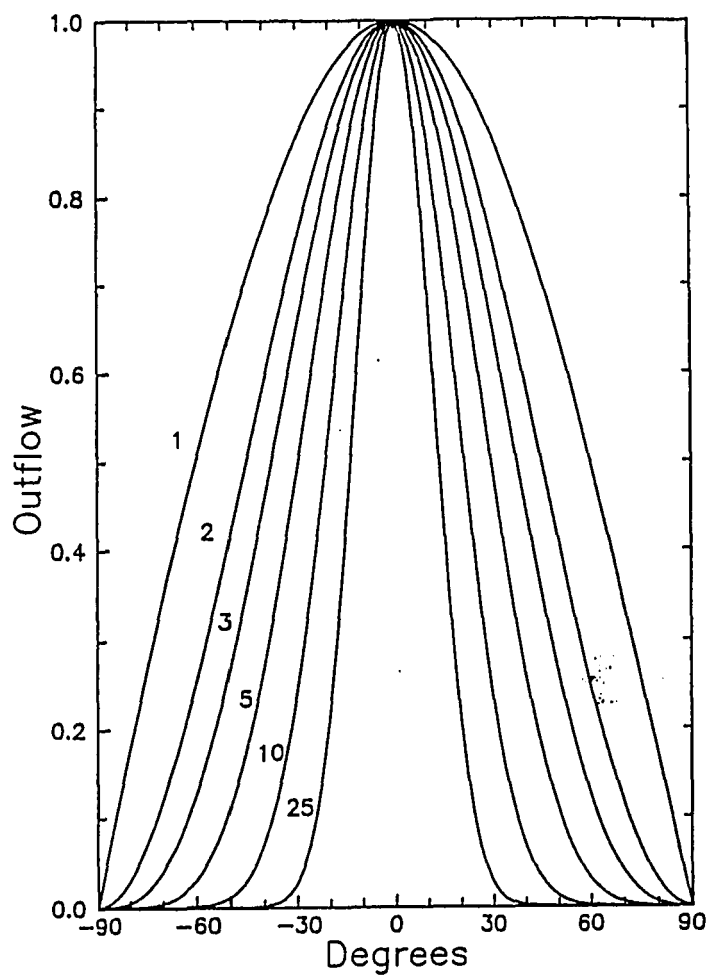


**Figure 6.3.** Functions  $\cos^n\theta$  ( $n = 1, 2, 3, 5, 10,$  and  $25$ ) used in the kinematic model to simulate non-uniform outflow into a hemisphere. The angular position of maximum outflow can be shifted relative to the subsolar point to accommodate leading and lagging distributions.

#### 6.2.4. $H_2O$ "Images"

The best fit synthetic line profiles are based upon calculated three-dimensional outflow distributions. We converted these distributions to two-dimensional column density maps in order to create the "spectroscopic" pictures of  $H_2O$  emission in Figs. 6.5, 6.9, and 6.13. These images simulate those that could have been recorded with an IR camera provided with a narrow-bandwidth filter or Fabry-Perot etalon centered on one of the strong  $H_2O$  lines in Fig. 6.1. Direct images of  $H_2O$  have not been obtained for any comet, however.

### 6.3. Interpretation of Cometary $H_2O$ Line Profiles

We discuss each comet observation separately. For the observed and synthetic cometary line profiles, "line width" is understood to mean the full width at the half maximum intensity points (FWHM). The width of the *sinc* function that satisfies the classic Rayleigh criterion for resolving two spectral lines with an FTS is not FWHM but  $FWHM/1.206$  (this is also equal to the distance between the peak and first zero of the *sinc* function). To avoid confusion we will give two width values in all subsequent references to the FTS, one appropriate to the resolution limit of the instrument and the second expressed as FWHM for direct comparison with cometary line widths.

#### 6.3.1. Comet P/Halley Preperihelion

The averaged  $H_2O$  line profile is included in Fig. 6.2 (curve with no symbols). Its width is  $3.9 \text{ km sec}^{-1}$  and its peak intensity is blue-shifted (Earth-approaching) by  $0.33 \pm 0.08 \text{ km sec}^{-1}$  (L87). The velocity resolution (unapodized) of the FTS for these

data was  $3.2 \text{ km sec}^{-1}$  ( $3.9 \text{ km sec}^{-1}$  FWHM). The ILS calculated for this resolution is included for comparison in Fig. 6.2 (curve with open symbols); only its first few side lobes are displayed. The observed  $\text{H}_2\text{O}$  line profile has the width, symmetric shape, and prominent side lobes of the ILS which means that the cometary line was unresolved and that its intrinsic width was therefore much less than  $3.9 \text{ km sec}^{-1}$ . The agreement also demonstrates that the achieved ILS met theoretical expectations and, consequently, that deconvolution of these data should yield a reliable measure of the intrinsic shape  $F(\nu)$  of the cometary  $\text{H}_2\text{O}$  line profile.

The deconvolved  $\text{H}_2\text{O}$  line profile is included in Fig. 6.2 (curve with solid symbols) and in Fig. 6.4 (solid line). As expected, the retrieved width is very narrow, only  $0.87 \text{ km sec}^{-1}$ , and that could actually be an upper limit. Outflow distributions fit to this profile must be highly collimated to produce its narrow line width and they must be directed into the Sun-facing hemisphere to generate the blue-shifted line position. As illustrated in Chapter 5, the line shift is diagnostic of asymmetric outflow, one consequence of which is that the width of the deconvolved line is coupled to the outflow distribution and therefore cannot be used by itself to estimate the outflow velocity  $v_{\text{H}_2\text{O}}$ . Our best fit synthesized  $\text{H}_2\text{O}$  line profile (dashed curve in Fig. 6.4) represents the superposition of three outflow components: isotropic outflow ( $3\% Q_{\text{H}_2\text{O}}$ ), a jet at  $\phi - 10^\circ$  ( $n = 25$ ,  $25\% Q_{\text{H}_2\text{O}}$ ), and a jet at  $\phi + 20^\circ$  ( $n = 15$ ,  $72\% Q_{\text{H}_2\text{O}}$ ) where  $\phi$  is the Sun-comet-Earth (or phase) angle. The two-dimensional column density map in Fig. 6.5 is an alternate display of this spatial distribution. The best fit profile establishes three important properties of Halley's preperihelion outflow. First, the isotropic component

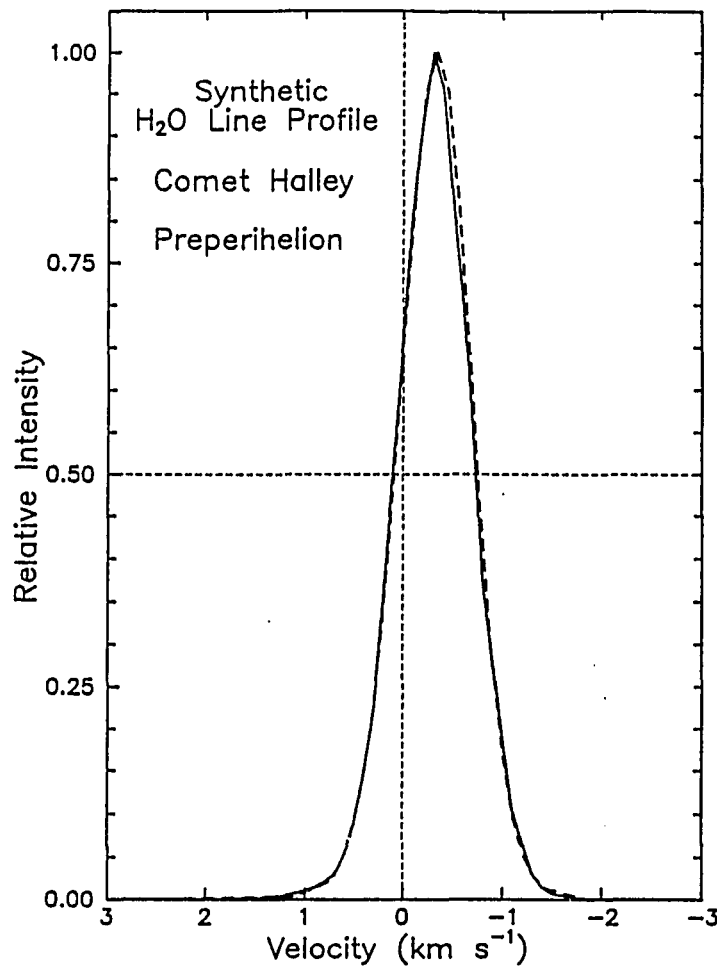


**Figure 6.4.** Model fit to the deconvolved H<sub>2</sub>O line profile in comet P/Halley preperihelion. *Solid curve:* the deconvolved line from Fig. 6.3. *Dashed curve:* the synthetic H<sub>2</sub>O line profile generated from the kinematic model. The close agreement was achieved by varying only anisotropy factors. The radial dependence of the outflow velocity and the kinetic temperature was fixed by hydrodynamic equations.

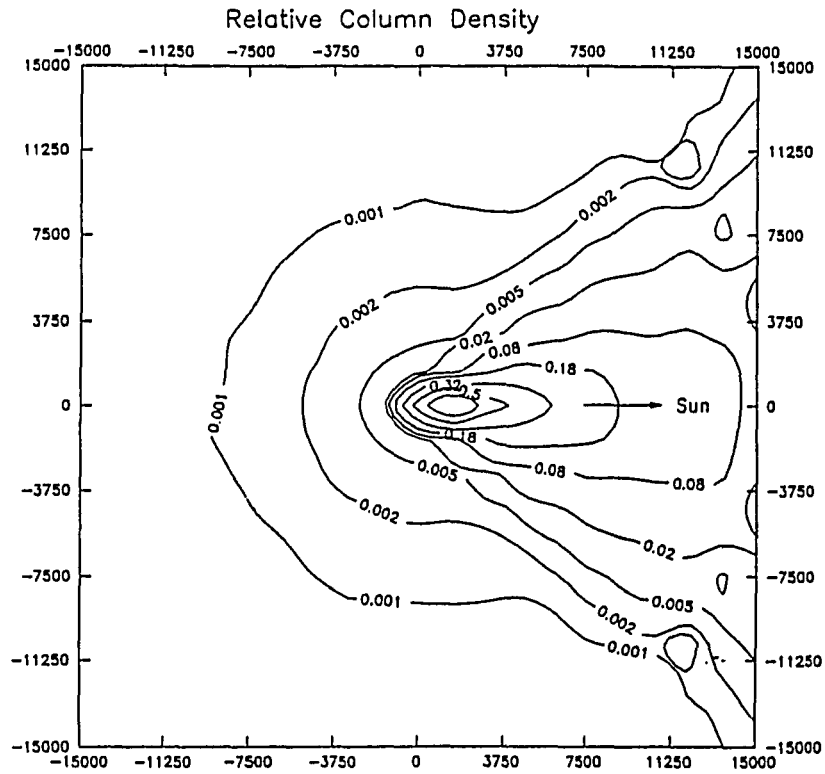


**Figure 6.5.** The two-dimensional column density map of  $\text{H}_2\text{O}$  in comet P/Halley preperihelion. This image was produced from the three-dimensional spatial distribution of  $\text{H}_2\text{O}$  used in the best fit synthetic line profile in Fig. 6.4. The spectrometer's FOV was circular with radius  $r = 1.5 \times 10^4$  km.

is necessarily restricted to only a few percent of the total H<sub>2</sub>O production in order to keep molecules in the FOV with velocity components  $>0$  km sec<sup>-1</sup> (Earth-receding) at their low observed abundances. Second, only a few narrow, jet-like features within 20° or less of the comet-Sun axis are necessary to model the observed velocity profile. Finally, the outflow is consistent with the temperature and velocity profiles obtained from standard hydrodynamic equations of the coma. The calculated radial velocity curve used to fit Halley's preperihelion line profile is included in Fig. 6.6.

The coma description given above is considerably more detailed than L87's previous analysis of these data. L87 characterized the preperihelion outflow with a constant expansion velocity ( $v_{\text{H}_2\text{O}} \approx 0.9$  km sec<sup>-1</sup>) while the present work is consistent with a profile in which  $v_{\text{H}_2\text{O}}$  increases slowly to  $\approx 0.9$  km sec<sup>-1</sup> at the edge of the FOV ( $1.5 \times 10^4$  km radius, see Fig. 6.6). L87 did identify the sunward-tailward asymmetry in the H<sub>2</sub>O distribution, but without a formal deconvolution of the data they could not retrieve the very narrow width of the cometary line and associate it with just a few jet-like features directed towards the Sun. Since multiple dust jets associated with discrete surface features due to long term erosion were observed directly in postperihelion images of comet P/Halley from spacecraft, it is reasonable to assume that the preperihelion outflow (both gas and dust) was also dominated by similar discrete surface sources. They are also the obvious explanation of Halley's considerable temporal activity during this preperihelion period (see L87 for details).

Hydrogen cyanide (HCN) is the only other parent molecule for which velocity-resolved spectra were acquired during Halley's last apparition (Bockelée-Morvan *et al.*

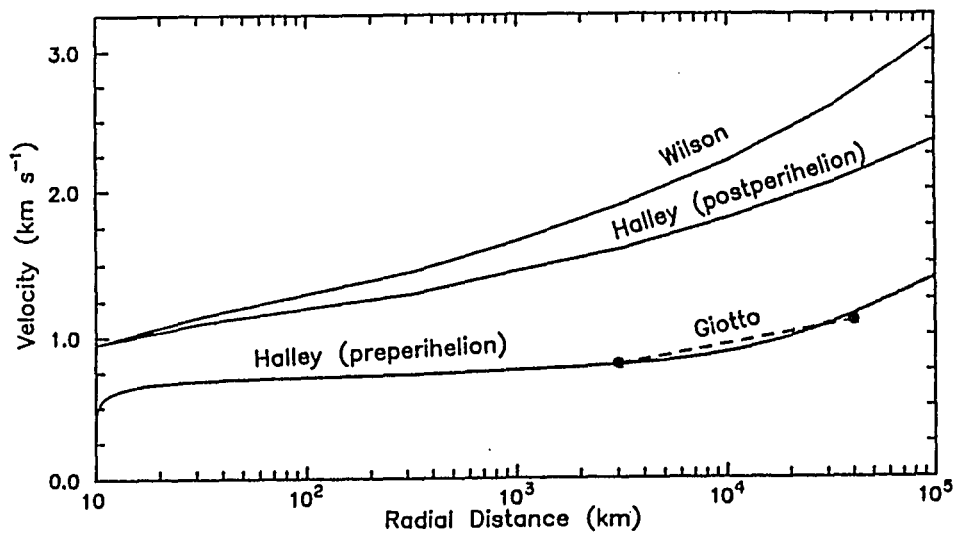


Figure 6.6. The velocity curves used in the kinematic model to fit observed H<sub>2</sub>O line profiles in comets Halley and Wilson. The curve for comet Halley preperihelion is unmodified from hydrodynamic calculations while those for Halley postperihelion and Wilson were scaled empirically from hydrodynamic calculations. The dashed line represents the *in situ* neutral gas velocity measurement from the *Giotto* NMS experiment.

1986; Schloerb *et al.* 1986, 1987a). Noteworthy similarities between the observed IR H<sub>2</sub>O and radio HCN lines include their Gaussian shapes and blue-shifted positions. However, the preperihelion HCN data were separated by  $\approx 12$  days from our observations of H<sub>2</sub>O on 24 December 1985 and the HCN line profiles have not been fit to outflow models. Consequently, the observed H<sub>2</sub>O and HCN lines should not be compared too closely because of the uncompensated influence of different phase angles, different beam sizes, and Halley's notorious temporal activity. The HCN expansion velocity is currently the only kinematic parameter that can be compared to results from H<sub>2</sub>O. Bockelée-Morvan *et al.* (1986) and Schloerb *et al.* (1987a) both concluded that  $v_{\text{HCN}}$  increased from  $\approx 0.8 \text{ km sec}^{-1}$  in early December 1985 to  $\approx 1.3 \text{ km sec}^{-1}$  near perihelion. Within errors, the interpolated HCN velocity on 24 December 1985 is consistent with the velocity profile used in our analysis of H<sub>2</sub>O.

The radio OH monitoring programs described in Gérard *et al.* (1987), Schloerb *et al.* (1987b), Tacconi-Garman (1989), Tacconi-Garman *et al.* (1990) [hereafter TGSC], and Bockelée-Morvan *et al.* (1990) revealed important variations in the shapes and positions of OH lines that relate to the parent distribution. The observed OH line profiles give direct evidence for OH kinematics, of course, but the retrieved parent distributions are dependent upon assumptions used in modelling the production, excitation, and distribution of OH. TGSC (1990) used the vectorial model for OH and monokinetic outflow modified by Maxwellian velocity dispersion at  $T = 50 \text{ °K}$  for H<sub>2</sub>O. Bockelée-Morvan *et al.* (1990) also used a vectorial model for OH, but only monokinetic outflow for H<sub>2</sub>O although they did explore the consequences of velocity

dispersion in the parent outflow on their model. TGSC's two OH spectral averages closest to our preperihelion H<sub>2</sub>O data were from 10-12 December 1985 and 3-5 January 1986. The observed OH line widths were  $\approx 2.0$  and  $2.4 \text{ km sec}^{-1}$  from which TGSC derived H<sub>2</sub>O parent velocities of  $0.8$  and  $1.0 \text{ km sec}^{-1}$ , respectively. TGSC attributed the increase in  $v_{\text{H}_2\text{O}}$  to decreasing heliocentric distance  $R_h$ , from which we interpolate an OH-derived H<sub>2</sub>O outflow velocity of  $\approx 0.9 \text{ km sec}^{-1}$  on 24 December 1985, in excellent agreement with our direct analysis of H<sub>2</sub>O. The H<sub>2</sub>O expansion velocity ( $\approx 1.4 \text{ km sec}^{-1}$ ) retrieved by Bockelée-Morvan *et al.* (1990) from their radio observations of OH during this period differs from TGSC's and our value. One factor that must be considered in assessing this difference is that the outflow models used to interpret the observed OH line profiles differ significantly in their treatment of anisotropic gas production. TGSC modelled asymmetric parent molecule production through a sunward-tailward anisotropy factor, but within each hemisphere he assumed that the outflow was isotropic. For December 10-12 TGSC deduced that the ratio of outflow into the day and night sides was  $\approx 2$  while during 3-5 January the outflow was isotropic. Bockelée-Morvan *et al.* (1990), on the other hand, assumed spherically symmetric H<sub>2</sub>O outflow in order to use trapezoidal synthetic line shapes as a simple means of interpreting observed OH line profiles. In general, TGSC's OH data demonstrate convincingly that neutral gas anisotropy persists to large radial distance in the coma (up to  $2 \times 10^6 \text{ km}$ ) and Bockelée-Morvan *et al.* (1990) admit that some of their OH profiles cannot be analyzed with their simple model because of obvious anisotropy in the OH spatial distribution. Untreated anisotropy should underestimate the expansion velocity according to Chapter 5 but

Bockelée-Morvan *et al.*'s preperihelion value of  $v_{\text{H}_2\text{O}}$  already seems too high. The discrepancy between the preperihelion values of  $v_{\text{H}_2\text{O}}$  deduced from OH measurements may therefore be due to additional factors, but it is beyond the scope of this paper to pursue them.

The day/night asymmetry in  $\text{H}_2\text{O}$  inferred from TGSC's OH data (factors from 1 to 3) is much less than that which we derived from  $\text{H}_2\text{O}$  (factor of  $\approx 50$ , see Fig. 6.5). This difference could be due to at least four factors. Changes in the coma due to Halley's temporal variability cannot be ignored since the  $\text{H}_2\text{O}$  and OH observations were separated by at least 12 days. In addition, the OH observations are typically averaged over many days in order to build up the SNR in the line profile, a procedure that would smooth short term behavior, whereas the  $\text{H}_2\text{O}$  line profiles provide much shorter (<2 hours) spectroscopic "snapshots" of coma activity. Another very important distinction between the  $\text{H}_2\text{O}$  and OH analyses is that our spectral outflow model accommodates very anisotropic distributions such as jets while TGSC's model is limited to hemispherical asymmetry. Finally the smoothing effect on molecular line profiles would increase with beam size, consistent with the small  $\text{H}_2\text{O}$  anisotropy factor deduced from radio observations of OH in the whole coma. We therefore conclude that the large difference between the radio and IR anisotropy factors for  $\text{H}_2\text{O}$  is due to model limitations which may eventually be relaxed and to differences in the way that the Halley OH and  $\text{H}_2\text{O}$  data were acquired and processed which cannot be changed.

In summary, Halley's preperihelion  $\text{H}_2\text{O}$  line profile indicates very localized gas production at the nuclear surface and a remarkably high day/night anisotropy factor of

$\approx 50$  at  $r \approx 10^4$  km. This description rests upon a combination of observational and interpretive factors (*e.g.*, observation of a parent species, short integration time, high SNR, versatile outflow model) that is unique to airborne IR observations of H<sub>2</sub>O.

### 6.3.2. Comet P/Halley Postperihelion

The averaged H<sub>2</sub>O line profile is included in Fig. 6.7 (solid curve without symbols). Its SNR is more than twice that of the preperihelion average in Fig. 6.2 due to higher  $Q_{\text{H}_2\text{O}}$  postperihelion (Weaver *et al.* 1987, see values in Table 6.1). The observed line width is 2.9 km sec<sup>-1</sup> and the peak intensity is blue-shifted by  $-0.26 \pm 0.07$  km sec<sup>-1</sup> from H<sub>2</sub>O rest positions (L87). The velocity resolution (unapodized) of the FTS was 1.1 km sec<sup>-1</sup> (1.3 km sec<sup>-1</sup> FWHM); the calculated ILS for this resolution is included in Fig. 6.7 (curve with open symbols). The observed line profile is more than twice as wide as the ILS and it exhibits no side lobes. The cometary H<sub>2</sub>O lines were therefore resolved and consequently the observed line profile remained essentially unchanged upon deconvolution with the ILS (see dashed curve in Fig. 6.7). The width of the postperihelion H<sub>2</sub>O line is 3.2 times that of the preperihelion line in spite of similar  $R_h$  (1.03 and 1.13 AU, respectively). We identify below physical changes in the coma that could have been responsible for the line broadening.

As with the preperihelion data, the observed blue-shift in the postperihelion line implies that the outflow was concentrated into the Sun-facing hemisphere. This is not difficult to model with combinations of isotropic and Sun-directed outflow components but the width of the postperihelion H<sub>2</sub>O line profile cannot be fit by any outflow distribution in a model that assumes the "standard" hydrodynamic velocity curve. The

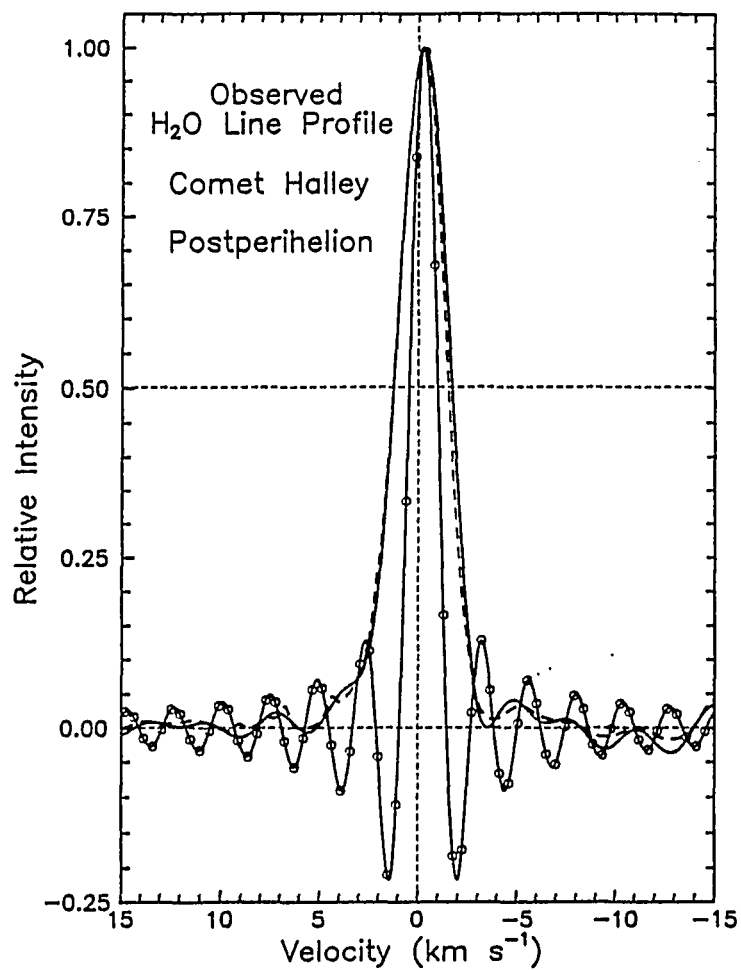


**Figure 6.7.** The H<sub>2</sub>O line profile in comet P/Halley postperihelion. *Solid curve*: the observed "average" line profile obtained by coadding individual lines in the spectrum. *Curve with open symbols*: the theoretical instrumental line shape (unapodized) for the FTS. The many side lobes are characteristic of the unapodized instrumental line shape of an FTS. Their absence in the observed profile indicates that the H<sub>2</sub>O lines were unresolved. *Dashed curve*: the deconvolved cometary line profile.

predicted velocities are just too small to yield components  $>1 \text{ km sec}^{-1}$  along the LOS for a significant fraction of the  $\text{H}_2\text{O}$  molecules in the FOV. The closest fit that the model could provide with the standard hydrodynamic velocity profile is indicated in Fig. 6.8 (short dashes). We were able to fit the observed width only by increasing  $v_{\text{H}_2\text{O}}$  by  $\approx 50\%$  over the calculated hydrodynamic values. The fit was also sensitive to the shape of the velocity curve. Uniform expansion velocity, even over the limited "plateau" region of the hydrodynamic velocity profile, was unsatisfactory. It was necessary to include a high velocity tail in our empirical curve at large radial distance in order to fit the high velocity wings of the observed profile. The velocity profile that provided an acceptable fit to the deconvolved  $\text{H}_2\text{O}$  line profile in Fig. 6.8 is included in Fig. 6.6. The best fit synthetic  $\text{H}_2\text{O}$  line in Fig. 6.8 (long dashes) based on this empirical velocity curve corresponds to the following outflow distribution: isotropic outflow ( $18\% Q_{\text{H}_2\text{O}}$ ); three jets ( $n = 15$ ) directed into a cone with half angle  $30^\circ$  along the comet-Sun axis ( $63\% Q_{\text{H}_2\text{O}}$ ); and an anti-sunward component ( $n = 7$ ,  $19\% Q_{\text{H}_2\text{O}}$ ). The equivalent two-dimensional map of this distribution is in Fig. 6.9; its bipolar appearance is due to the presence of sunward and anti-sunward outflow components. The inclusion of anti-sunward outflow in our fit was necessary to fill in the line profile for positive velocity components along the LOS. Use of a larger isotropic component was unsatisfactory for this purpose because it led to a broad plateau in the synthetic profile that was incompatible with the observed line shape. The anti-sunward component most likely represents an outburst, or at least the remnants of one. Outbursts, as distinguished from periodic temporal variations due to rotation of discrete surface sources into the Sun-

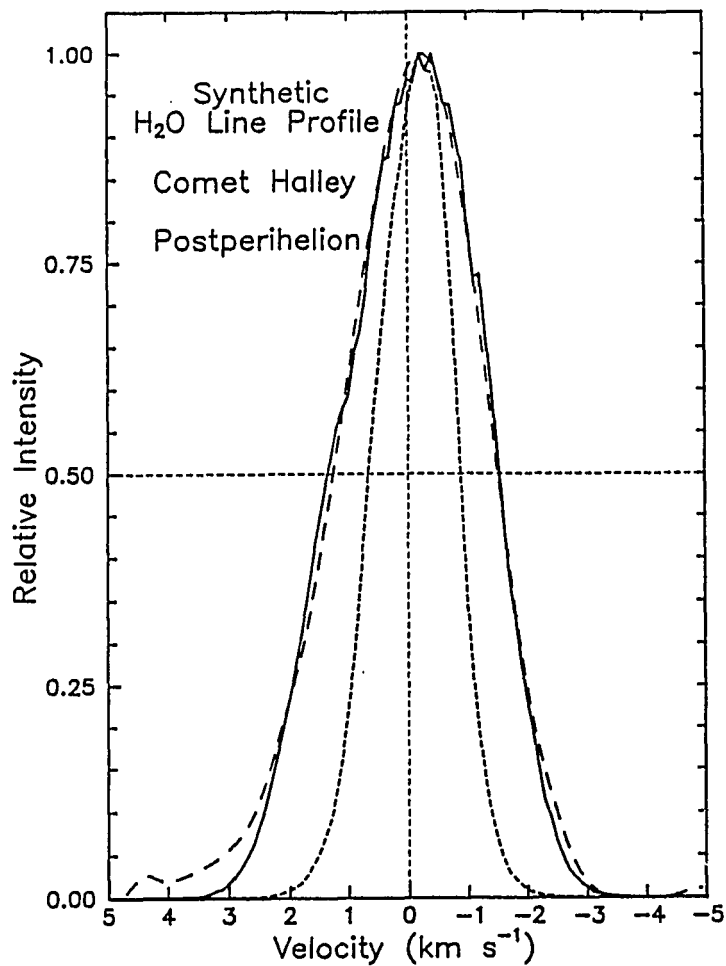


**Figure 6.8.** Model fit to the deconvolved H<sub>2</sub>O line profile in comet P/Halley postperihelion. *Long dashes*: the deconvolved line from Fig. 6.6. *Short dashes*: the closest fit possible with the outflow velocity and kinetic temperature calculated from standard hydrodynamic equations. *Solid curve*: the best fit synthetic H<sub>2</sub>O line profile generated with an empirical velocity profile in the kinematic model.

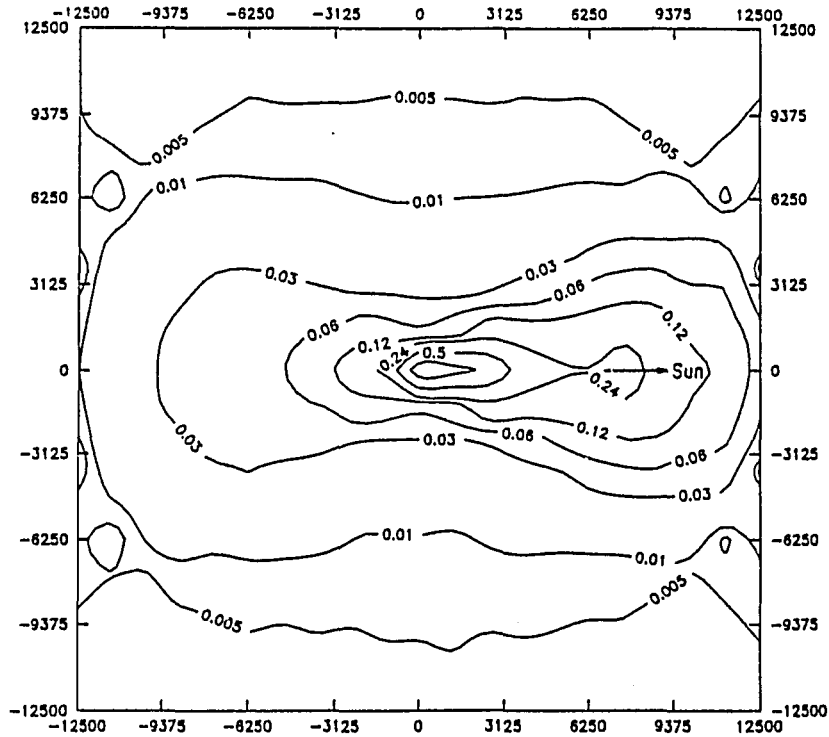


**Figure 6.9.** The two-dimensional column density map of  $\text{H}_2\text{O}$  in comet P/Halley postperihelion. This image was produced from the three-dimensional spatial distribution of  $\text{H}_2\text{O}$  used in the best fit synthetic line profile in Fig. 6.8. The spectrometer's FOV was circular with radius  $r = 1.1 \times 10^4$  km.

facing direction, apparently were frequent during this postperihelion period. Visible images of an anti-sunward outburst were recorded on UT 24.7 March 1986 (Rettig *et al.* 1987) and a major outburst of H<sub>2</sub>O was observed on UT 20.7 March 1986 (Larson *et al.* 1990), although its direction was not determined. It is possible that some of the anti-sunward component of H<sub>2</sub>O required to fit the observed line profile on UT 22.7 March 1986 is a remnant of the outburst that occurred two days earlier if mass ejection was more or less in the anti-sunward direction.

In the previous interpretation of Halley's postperihelion H<sub>2</sub>O line profile L87 recognized that the outflow distribution was asymmetric and that  $v_{\text{H}_2\text{O}}$  was significantly higher than the preperihelion value. They estimated the assumed constant  $v_{\text{H}_2\text{O}}$  to be half the width of the resolved H<sub>2</sub>O line profile, or  $1.4 \pm 0.2 \text{ km sec}^{-1}$ . In Chapter 5 we have demonstrated that this approach is adequate for isotropic outflow at constant velocity but it underestimates the velocity for asymmetric distributions and it provides little insight into velocity profiles that vary significantly with radial distance. Combi (1989) made similar remarks for analyses of radio HCN line profiles. We confirm here that  $v_{\text{H}_2\text{O}}$  postperihelion was high, but its profile in Fig. 6.6 is more relevant than some average value. If we adopt  $v_{\text{H}_2\text{O}}$  at the edge of the spectrometer's FOV as the basis for comparing our revised results, the postperihelion value ( $\approx 1.8 \text{ km sec}^{-1}$ ) is approximately twice the preperihelion value ( $\approx 0.9 \text{ km sec}^{-1}$ , see Fig. 6.6). TGSC's March OH average yielded  $v_{\text{H}_2\text{O}} = 1.6 \pm 0.07 \text{ km sec}^{-1}$  and Bockelée-Morvan *et al.* (1990) obtained  $v_{\text{H}_2\text{O}} \approx 1.4 \text{ km sec}^{-1}$ , both consistent with our empirical velocity curve in Fig. 6.6. The postperihelion outflow velocity obtained from HCN was  $\approx 1.2 \text{ km sec}^{-1}$  (Schloerb *et al.*

1987a), but HCN expansion velocities inferred from analyses of CN shell-like structures were much smaller ( $\leq 0.7 \text{ km sec}^{-1}$ , Celnik and Schmidt-Kaler 1987). A significant fraction of the observed CN may have been derived instead from grains in the coma (cf. A'Hearn *et al.* 1986), however, in which case direct comparison with velocities observed in gaseous HCN and H<sub>2</sub>O may not be appropriate.

TGSC's OH spectral line profile for March was significantly wider than others in their monitoring program and it had a distinctly non-Gaussian shape. Gérard *et al.* (1987a) noted the same behavior in their March 1986 radio OH line profile. These radio data therefore indicate that there was unusual kinematic activity in the coma during the same period in which large temporal variations in gas and dust production were noted by many authors (*e.g.*, McFadden *et al.* 1987, Larson *et al.* 1990, and references therein). TGSC also noted the pronounced pre/postperihelion asymmetry in  $v_{\text{H}_2\text{O}}$  ( $1.02 \pm 0.10$  and  $1.60 \pm 0.07 \text{ km sec}^{-1}$ , respectively, at 1 AU) that is evident in our retrieved velocity curves, but Bockelée-Morvan *et al.* (1990) did not find a similar result in their radio OH data. The asymmetry in velocity is predicted by outflow models if the production rate  $Q_{\text{H}_2\text{O}}$  is asymmetric with  $R_h$  (Bockelée-Morvan and Crovisier 1987b, Combi 1989), as was the case for comet Halley (*e.g.*, Weaver *et al.* 1987, Fink and DiSanti 1990). Combi (1989) used his dusty-gas-dynamic/Monte Carlo model to calculate pre- and postperihelion velocity curves that resemble our empirical curves in Fig. 6.6;  $v_{\text{H}_2\text{O}}$  at the radius of the collision zone was  $0.82 \text{ km sec}^{-1}$  for  $Q_{\text{H}_2\text{O}} \approx 10^{29} \text{ sec}^{-1}$  preperihelion and  $1.24 \text{ km sec}^{-1}$  for  $Q_{\text{H}_2\text{O}} \approx 10^{30} \text{ sec}^{-1}$  postperihelion. His model underestimates the postperihelion velocities derived from OH and H<sub>2</sub>O, however,

particularly the high velocities at large  $r$  in our retrieved curve in Fig. 6.6. The relative simplicity of Combi's model compared with Halley's anisotropic, time-dependent behavior is certainly one factor, but other recent theoretical work demonstrates that closer agreement is possible as other features are added to the models. For example, Crifo (1990) modeled the velocity and temperature profiles in comet P/Halley at the time of the spacecraft encounters. In general, his predicted velocity profile does not have the flat "plateau" region characteristic of the standard hydrodynamic velocity curve and the values are higher than in most other models ( $\approx 1.45 \text{ km sec}^{-1}$  at  $r = 10^4 \text{ km}$ ). These characteristics are due to heating in the inner coma by condensation of  $\text{H}_2\text{O}$  into clusters. The work of both Combi and Crifo therefore demonstrates that coma models still have considerable capacity to "stretch" in order to reproduce observations.

One postperihelion velocity measurement does not appear consistent with the above results. The *in situ* measurements from *Giotto* indicated lower velocities ( $0.8 - 1.1 \text{ km sec}^{-1}$  between  $r = 3 \times 10^3 - 4 \times 10^4 \text{ km}$ ) (Lämmerzahl *et al.* 1987, see also Fig. 6.6) than those derived from remote observations of OH,  $\text{H}_2\text{O}$ , and HCN. One possible explanation of this difference is that the remote and *in situ* measurements of  $v_{\text{H}_2\text{O}}$  should not be compared directly at all. The spectroscopic measurements average much of the coma but they are dominated by high density outflow in gas jets in the subsolar region. *Giotto*'s neutral mass spectrometer, on the other hand, may have sampled lower density material away from the centers of the jets where physical conditions could have been as different as observed. This point was emphasized by Crifo (1990) whose velocity calculations in regions of peak outflow were also higher than the *Giotto* measurements.

The Sun-directed activity in our postperihelion fit is consistent with many other observations of comet Halley during this period. The striking images from *Giotto* convincingly demonstrated that dust originated almost exclusively in discrete areas on the sunlit side of the nucleus (Keller *et al.* 1987) and the TKS experiment on *Vega* established that H<sub>2</sub>O was ejected into a cone of angle  $50 \pm 10^\circ$  in the sunward direction (Krasnopolsky *et al.* 1988). This angular distribution is similar to the sunward components retrieved from our H<sub>2</sub>O lines although detailed comparison is inappropriate given the weeks between the *Vega* encounter and the *KAO* observations. Behavior of the gaseous component elsewhere in the coma during this period is indicated by numerous analyses of Earth-based observations. Weaver *et al.* (1986) detected a sunward-tailward asymmetry of only  $\approx 3$  in the H<sub>2</sub>O column density at  $r \approx 3 \times 10^4$  km from analysis of the relative intensities of H<sub>2</sub>O lines observed in FOV's centered on the nucleus and at offset locations. Radio observations of OH and HCN during 1986 March support this picture. TGSC derived a day/night anisotropy factor of 2.4 in the parent distribution from OH observations averaged over 15-19 March and Bockelée-Morvan *et al.* (1990) concluded that their OH average for 29-31 March required a strong, Sun-directed jet. Schloerb *et al.* (1987a) noted blue-shifts in radio HCN lines ( $-0.18 \pm 0.05$  km sec<sup>-1</sup>) which they attributed to dominant sunward activity, although they did not retrieve spatial distributions. In principle, images of [OI] <sup>1</sup>D emission at 6300 Å should map the spatial distribution of H<sub>2</sub>O in those regions of the coma where the emission is not quenched by collisions. The forbidden [OI] line is excited following photodissociation of H<sub>2</sub>O and its lifetime (110 sec) is so short compared to the photochemical lifetime

of H<sub>2</sub>O ( $8.3 \times 10^4$  sec) that an [OI] photon marks the position of the parent H<sub>2</sub>O molecule to within  $\approx 100$  km. Magee-Sauer *et al.* (1988) noted that the spatial distribution of [OI] was symmetric about the nucleus during observations in 1986 April and May, while Fink and DiSanti (1990) acquired at least one [OI] scan (2 March 1986) showing strong asymmetry in the sunward direction. Unfortunately, none of the published [OI] data is presented in the form of two-dimensional column density maps and the [OI] observations are separated by many weeks from our airborne H<sub>2</sub>O data. Direct comparisons of [OI] and H<sub>2</sub>O spatial distributions are therefore not possible.

Earth-based spectroscopic observations of the neutral gas outflow in comet Halley postperihelion provide ample evidence for anisotropy, but all measurements of the day/night asymmetry were much less than that observed in the dust outflow from spacecraft. Possible explanations include more efficient isotropization of the gaseous component of the coma or the preferential release of gas over dust on the night side as solar heating reached subsurface ice layers. Model calculations support the measurements of gas anisotropy in comet Halley. Kömle and Ip (1987) used an axisymmetric hydrodynamical model to predict that day/night anisotropy factors up to  $\approx 30$  would persist at  $r \approx 10^4$  km. Their calculations of spatial anisotropy were very sensitive to thermal balance in the coma, thus suggesting a potentially important observational link between kinematic and thermal models of the coma. In an initial test of their model, Kömle and Ip successfully reproduced the observed postperihelion asymmetry in H<sub>2</sub>O that Weaver *et al.* (1986) measured and which we independently obtained in our line profile analysis. The relatively low value of this anisotropy factor

( $\approx 3$ ) is consistent with the tendency of a hotter coma (as inferred from the high outflow velocity postperihelion) to isotropize more efficiently. Kömle and Ip's model requires that our much higher preperihelion anisotropy factor ( $\approx 50$ ) be associated with a cooler coma, as is the case. Numerical simulations of the observed preperihelion anisotropy in  $\text{H}_2\text{O}$  were not performed by Kömle and Ip, however.

There is also evidence for anisotropic outflow in the *in situ* density measurements made with the PLASMAG and NGE experiments on *Vega*. The measurements revealed inbound/outbound asymmetry in the neutral gas density due apparently to gas jets originating at the nucleus (Remizov *et al.* 1986, Hsieh *et al.* 1987). In addition, significant spatial and temporal deviations from a simple  $r^{-2}$  dependence were noted in the PLASMAG data during the outbound leg on *Vega-1* (Gringauz *et al.* 1986) although similar behavior was not evident in the NGE data from the same spacecraft. It is unfortunate that NMS/*Giotto* stopped functioning just before closest approach and was therefore unable to provide data on the outbound leg for comparison both with its inbound density profile and the *Vega* data.

Although the spacecraft measurements revealed anisotropy in the coma, difficulties remain in understanding instrument performance and in interpreting the data quantitatively. We illustrate the problem as follows. The inbound data from each experiment were fit to the Haser model

$$n(r) = \frac{c_0}{r^2} \exp\left(-\frac{r}{c_1}\right) \quad (6.2)$$

Table 6.2. Haser Model Fits to *In Situ* Observations of Comet Halley

Experiment	Trajectory	Normalizing Factor ( $c_0$ ) (molecules $\text{cm}^{-3} \text{ km}^2$ )	Scale Length ( $c_1$ ) (km)
PLASMAG/ <i>Vega</i> <sup>1</sup>	Inbound	$1.0 \times 10^{14}$	$2.0 \times 10^6$
NGE/ <i>Vega</i> <sup>2</sup>	Inbound	$8.9 \times 10^{13}$	$1.7 \times 10^5$
	Outbound	$5.6 \times 10^{13}$	$2.9 \times 10^5$
NMS/ <i>Giotto</i> <sup>3</sup>	Inbound	$4.7 \times 10^{13}$	$4.0 \times 10^4$

<sup>1</sup> Gringauz *et al.* 1986

<sup>2</sup> Hsieh *et al.* 1987

<sup>3</sup> Krankowsky *et al.* 1986

with the parameters listed in Table 6.2. The parameter  $c_1$  is dimensionally equivalent to a scale-length which is  $8.3 \times 10^4$  km for  $\text{H}_2\text{O}$  in a Haser model assuming  $v_{\text{H}_2\text{O}} = 1.0$  km  $\text{sec}^{-1}$  and a photochemical lifetime  $\tau_{\text{H}_2\text{O}} = 8.3 \times 10^4$  sec at 1 AU. The large discrepancies between the measured scale-lengths in Table 6.2 and the nominal Haser value for  $\text{H}_2\text{O}$  could be due to many factors, including detection of material other than gaseous  $\text{H}_2\text{O}$ , technical problems with the experiments, spatial and temporal differences in Halley's coma *between* the *Vega* and *Giotto* flybys, anisotropy in Halley's coma *during* the measurements, and error in the theoretical value of  $\tau_{\text{H}_2\text{O}}$ . A systematic evaluation of all of these factors is beyond the intent of this paper, and may not even be possible. In the following discussion we review some of the known sources of discrepancy in the scale-length measurements and we demonstrate the potentially large effect of anisotropy on them.

The PLASMAG experiment gave the highest density and largest scale-length in

Table 6.2. This is probably a consequence of using a ram Faraday cup that may have responded to scattered Ly  $\alpha$  photons and energetic charged particles in addition to neutral molecules of all species. Thus, the PLASMAG scale-length cannot be compared directly with other density measurements that apply primarily to gaseous H<sub>2</sub>O. Several known problems with the NGE experiment affect its scale-length measurements. The crippled power supply of the field ionization source (FIS) and saturation at  $r < 5 \times 10^4$  km in the electron impact ionization source (EIS) significantly compromised its mass resolution and increased its background contamination (Curtis *et al.* 1987). By ignoring NGE data at  $r > 6 \times 10^4$  km where background uncertainties dominate, the discrepancy between the NGE/*Vega* and NMS/*Giotto* scale-lengths in Table 6.2 decreases from a factor of  $\approx 5$  to  $\approx 2$  as  $r$  decreases to  $8.9 \times 10^3$  km, the closest approach of *Vega-1*. This smaller difference could be due to temporal and spatial differences in the coma between the two spacecraft observations. Thus, the largest discrepancies in Table 6.2 seem to disappear when instrumental factors are considered, but large uncertainties still apply.

One practice that certainly needs to be critically reviewed in the context of these spacecraft measurements is the use of symmetric outflow models (*e.g.*, Eq. 6.2) to analyze density distributions that are demonstrably anisotropic. We therefore sampled our retrieved H<sub>2</sub>O density distribution for comet Halley postperihelion along hypothetical spacecraft trajectories in order to characterize the signatures of anisotropy in *in situ* measurements. Four representative inbound/outbound density profiles extracted from our best fit H<sub>2</sub>O outflow distribution (see Fig. 6.9) are included in Fig. 6.10. Although our retrieved H<sub>2</sub>O density distribution on 23 March cannot be

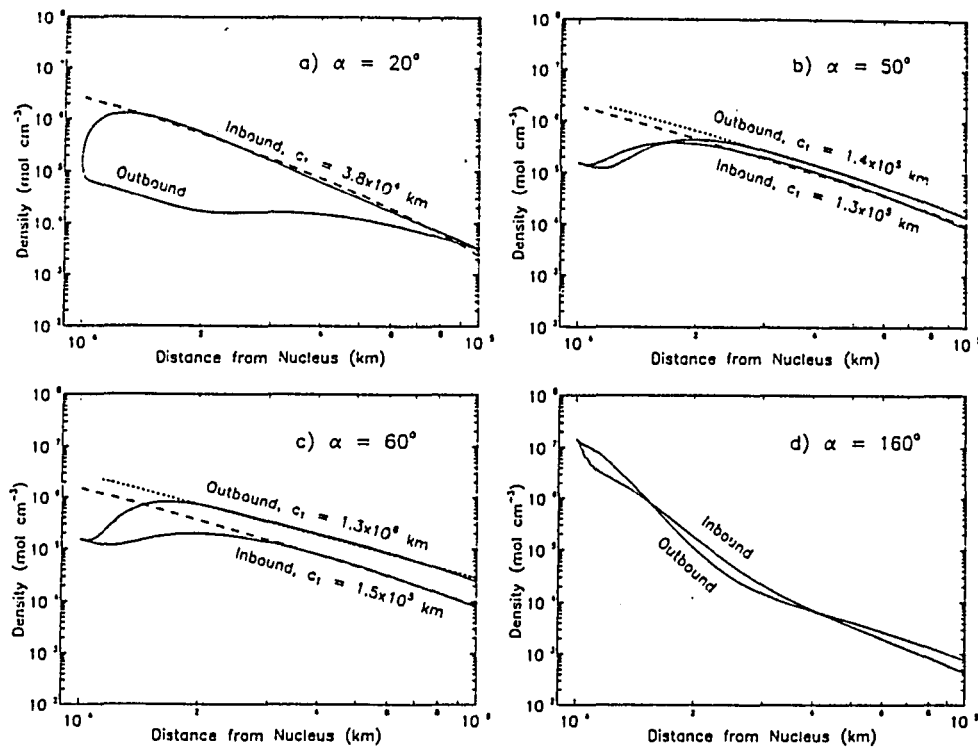


**Figure 6.10.** Synthetic *in situ*  $\text{H}_2\text{O}$  density profiles along hypothetical spacecraft trajectories in the coma of comet Halley postperihelion for the spatial outflow distribution in Fig. 6.9. The trajectories are in the comet-Sun-Earth plane with the flyby angle  $\alpha$  measured from the Earth-comet axis towards the Sun (*i.e.*,  $\alpha = 90^\circ - \phi$  for a trajectory normal to the comet-Sun axis where  $\phi$  is the phase angle). The distance of closest approach was  $10^4$  km on the sunward side of the nucleus for all examples. The dashed curves represent Haser models fit to those portions of the density profiles exhibiting approximate  $r^{-2}$  behavior. The adjustable parameter  $c_1$  (see Eq. 6.2) corresponds to the  $\text{H}_2\text{O}$  scalelength in the traditional use of the Haser density profile. The retrieved values should be  $8.3 \times 10^4$  km but none of the examples in this figure 6.9. comes closer than a factor of 1.6 and the extreme values differ by a factor of 30. These errors are due entirely to neglect of anisotropy in the coma.

compared literally with that encountered by *Vega* and *Giotto* several weeks earlier, some generalizations are still relevant. One obvious indication of anisotropy in Fig. 6.10 is the inbound/outbound asymmetry in the density profiles. Variations in the shape and slope of each density curve are additional indications of anisotropy in the coma. The curves are very sensitive to the flyby direction. Some profiles display the  $r^{-2}$ -dependence expected for symmetric outflow, at least over a limited range of radial distance, while others are clearly incompatible with any simple power law. We fit Eq. 6.2 (the dashed curves in Fig. 6.10) to some of our synthetic density profiles in the same manner as was done for the *Vega* and *Giotto* data. For many profiles in Fig. 6.10 the Haser model fits portions of the data very well in a numerical sense, but the adjustable parameter  $c_1$  represents density variations introduced *both* by photodissociation and anisotropic outflow so its physical interpretation as a measured scale-length would therefore be erroneous. In fact, our retrieved scale-lengths differ by more than a factor of 30 with none equaling the nominal value expected for the assumed Haser conditions. From these numerical simulations we conclude that the measured "scale-lengths" in Table 6.2 could be influenced as much by anisotropy in the coma as by any of the instrumental factors listed above. Consequently, such "scale-lengths" should not be converted into photochemical lifetimes simply by dividing by the assumed constant expansion velocity in the Haser model. This realization is especially relevant to the NMS/*Giotto* experiment since it offers in principle a direct measurement of  $\tau_{\text{H}_2\text{O}}$  for comparison with photochemical calculations. Krankowsky *et al.* (1986) obtained a value of  $\tau_{\text{H}_2\text{O}}$  from use of Eq. 6.2 that was  $\approx 50\%$  lower than expected which they

attributed to solar ultraviolet flux variations during the flyby. Allen *et al.* (1987) noted that the discrepancy became smaller upon correcting an error in the distance scale (see *Note added in proof* in Krankowsky *et al.* 1986) and adopting a revised value of the outflow velocity. They did not give their numerical value of  $\tau_{\text{H}_2\text{O}}$ , however, perhaps because they concluded that even their revised analysis was invalid since the assumption of constant outflow velocity in the Haser model is incorrect. We demonstrated here that the analysis could also be questionable because the coma was significantly anisotropic during the *Giotto* flyby. Thus, the discrepancy between the original NMS measurement and the generally accepted theoretical value of  $\tau_{\text{H}_2\text{O}}$  has not yet been satisfactorily reconciled. Of the four sources of systematic error listed above, only one (the distance scale) has been factored into the measurement of  $\tau_{\text{H}_2\text{O}}$ . An outflow model can accommodate the non-uniform expansion velocity (Chapter 5), but independent knowledge of the asymmetry along *Giotto*'s trajectory would ultimately be required to retrieve a definitive measurement of  $\tau_{\text{H}_2\text{O}}$  from the NMS data.

In summary, Halley's postperihelion  $\text{H}_2\text{O}$  line profile differs from that preperihelion because of intrinsically higher outflow velocities and increased velocity dispersion due to more complicated jet activity. The different pre- and postperihelion spatial distributions are easy to reconcile given Halley's evolved surface, while the changes in the velocity profiles are due to heating of the coma by higher  $Q_{\text{H}_2\text{O}}$  postperihelion and other processes such as  $\text{H}_2\text{O}$  recondensation and radiation trapping that may be strong functions of  $Q_{\text{H}_2\text{O}}$  and anisotropy in the subsolar region.

### 6.3.3. Comet Wilson (1987 VII)

The averaged H<sub>2</sub>O line profile is displayed in Fig. 6.11 (solid curve without symbols). The observed line width is 4.8 km sec<sup>-1</sup> and the peak line intensity is blue-shifted by  $-1.17 \pm 0.08$  km sec<sup>-1</sup> from H<sub>2</sub>O rest frequencies (L89). The velocity resolution (unapodized) of the spectrometer was 3.2 km sec<sup>-1</sup> (3.9 km sec<sup>-1</sup> FWHM). The ILS corresponding to this resolution is displayed in Fig. 6.11 (curve with open symbols). The observed H<sub>2</sub>O line profile is  $\approx 23\%$  wider than the ILS and it displays attenuated sidelobes shifted relative to those of the ILS, characteristics that indicate a partially resolved spectral line. The symmetry in the observed H<sub>2</sub>O line profile is evidence that the achieved ILS was correct and, consequently, that deconvolution will give an accurate result. The velocity width of the deconvolved line (dashed curve in Fig. 6.11) is 2.8 km sec<sup>-1</sup>. This value is comparable to that measured in comet P/Halley postperihelion, but the cometocentric line shift for Wilson ( $-1.2$  km sec<sup>-1</sup>) is much higher than for Halley ( $< -0.3$  km sec<sup>-1</sup> both pre- and postperihelion).

The large blue-shift requires that the maximum H<sub>2</sub>O outflow was directed along or near the comet-Earth LOS rather than towards the Sun. Since so few molecules had positive velocity components, isotropic outflow is excluded and strict limits apply to any type of anti-sunward activity. As was the case with comet Halley postperihelion, the large width of comet Wilson's line profile is incompatible with the standard hydrodynamic velocity curve. Our best fit is illustrated with the synthetic line profile in Fig. 6.12 (dashed curve), the two-dimensional H<sub>2</sub>O column density map in Fig. 6.13, and the empirical velocity curve in Fig. 6.6. The outflow distribution consists of a

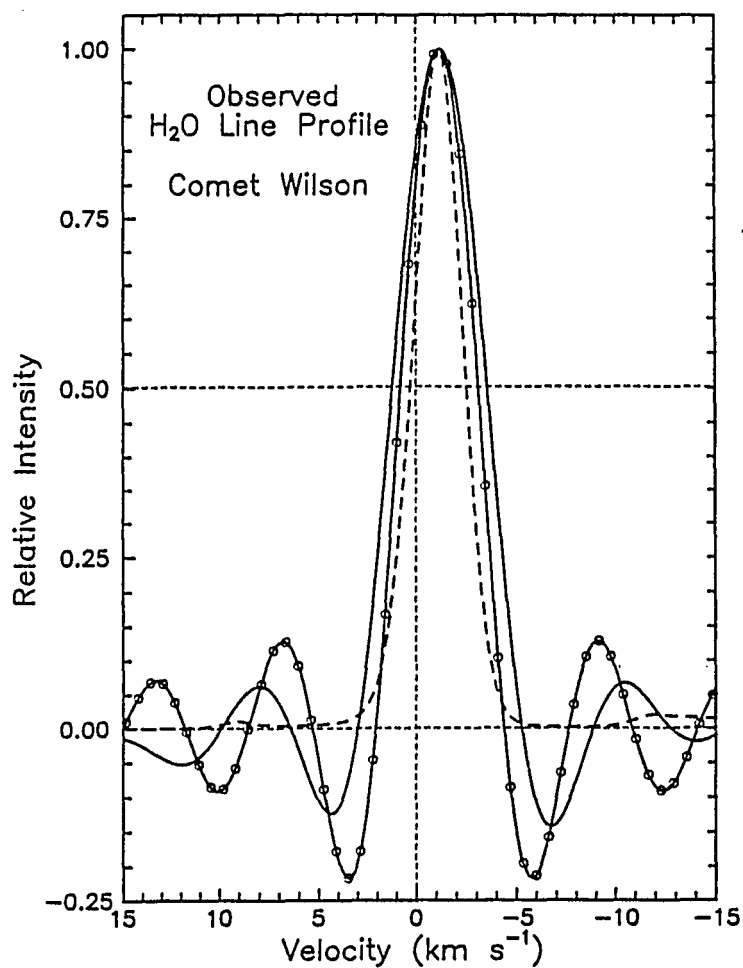
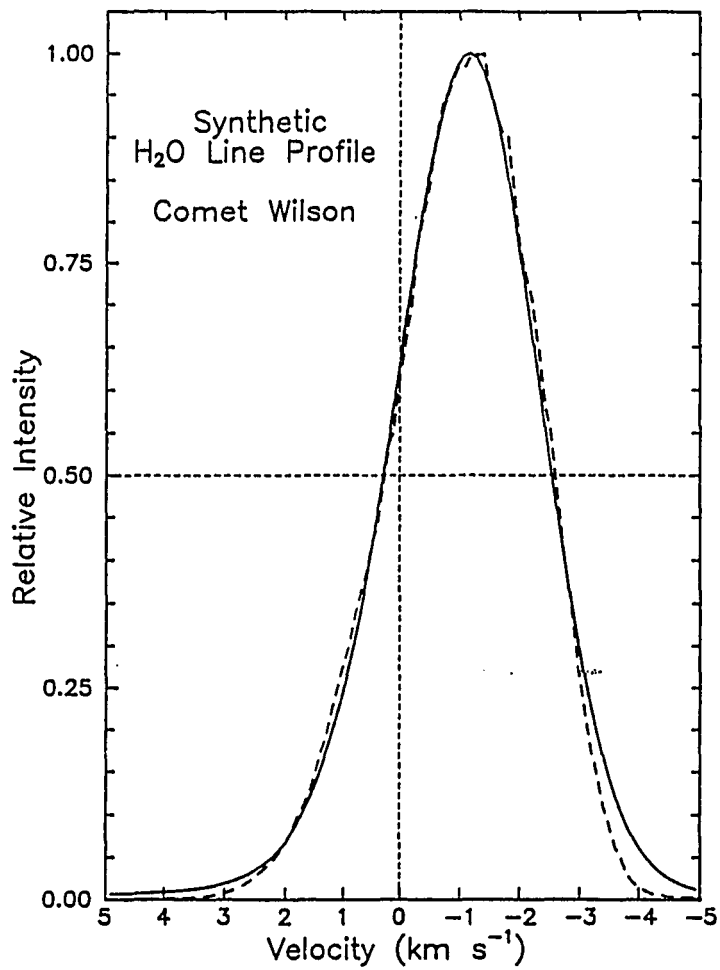
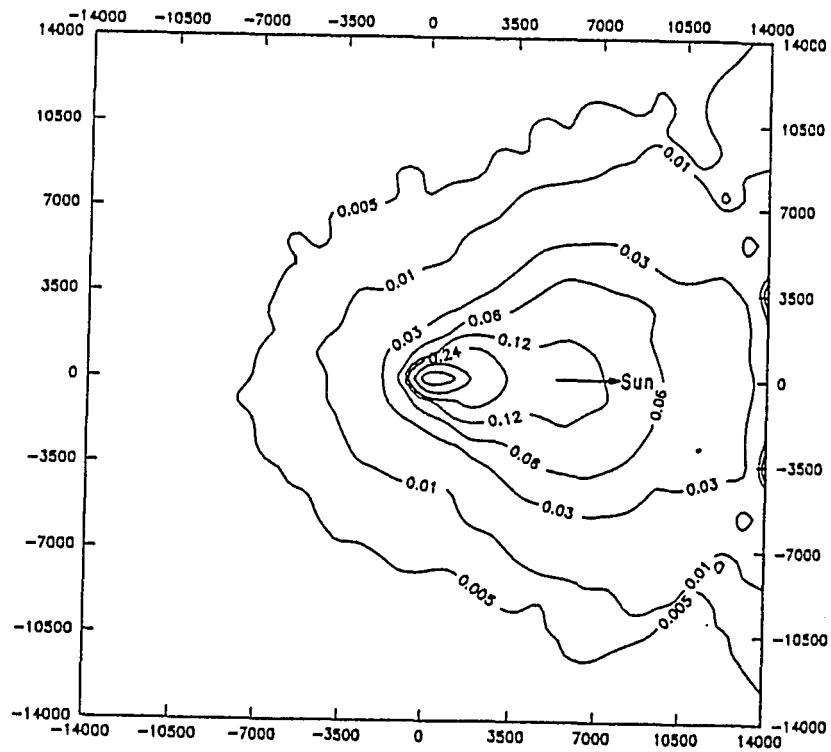


Figure 6.11. The H<sub>2</sub>O line profile in comet Wilson. *Solid curve*: the observed "average" line profile obtained by coadding the individual lines in the spectrum in Fig. 6.1. *Open symbols*: the theoretical instrumental line shape (unapodized) for the FTS. The attenuated amplitude of the side lobes in the observed profile indicates that the H<sub>2</sub>O lines were partially resolved. *Dashed curve*: the deconvolved cometary line profile. All profiles peak at the observed cometocentric velocity of  $-1.17 \text{ km sec}^{-1}$  (Earth approaching).



**Figure 6.12.** Model fit to the deconvolved H<sub>2</sub>O line profile in comet Wilson. *Solid curve:* the deconvolved line from Fig. 6.11. *Dashed curve:* the best fit synthetic H<sub>2</sub>O line profile generated with an empirical velocity profile in the kinematic model.



**Figure 6.13.** The two-dimensional column density map of H<sub>2</sub>O in comet Wilson. This image was produced from the three-dimensional spatial distribution of H<sub>2</sub>O used in the best fit synthetic line profile in Fig. 6.12. The spectrometer's FOV was circular with radius  $r = 1.4 \times 10^4$  km.

small isotropic component (5%  $Q_{\text{H}_2\text{O}}$ ) and four relatively broad ( $n = 3$ )  $\cos^n\theta$ -distributions (95%  $Q_{\text{H}_2\text{O}}$ ) spaced between the comet-Sun axis and the comet-Earth LOS ( $\phi = 77^\circ$ ) with intensities adjusted to reproduce the observed line profile. The number of components is probably not significant; a larger number of narrower features could have done as well. The physically relevant aspect of their superposition is that a relatively broad beam peaked at  $\phi - 60^\circ$  concentrated maximum  $\text{H}_2\text{O}$  production towards Earth. The phase delay ( $\approx 60^\circ$ ) implies that there was thermal inertia in the nuclear surface due perhaps to a thin refractory crust if nuclear rotation were retrograde. Comet Wilson's surface had to be relatively unevolved, however, given the lack of evidence for short term temporal variability in gas and dust production (L89, Campins *et al.* 1989, Roettger *et al.* 1989, Lynch *et al.* 1989). Campins *et al.* (1989) concluded from thermal IR images of Wilson's dust emission that most of the dust in the coma of comet Wilson was ejected in a "beam" from the afternoon side of the subsolar point and that nuclear rotation was prograde with respect to its orbital motion. The Doppler information in our spectral line profile also gives some insight into the sense of Wilson's nuclear rotation but we suggest that nuclear rotation was retrograde in order to place maximum outflow from the afternoon side of the nucleus near the comet-Earth LOS. Were the rotation prograde, the spectral line profile would shift by  $\approx 1 \text{ km sec}^{-1}$  towards positive cometocentric velocities. The apparent contradiction between our sense of rotation and Campins *et al.*'s might be due to changes in aspect that occurred during the month between the two observations. This might be resolved if independent knowledge of the pole of comet Wilson were available.

Since the H<sub>2</sub>O outflow was concentrated along the comet-Earth LOS, many molecules stayed in the cylindrical FOV until they photodissociated. Our line profile fit is therefore sensitive to the velocity of parent molecules at large radial distance ( $r > 10^4$  km) where coma models are less constrained. The empirical velocity curve used to fit the observed line profile is included in Fig. 6.6. We modified the standard hydrodynamic velocity curve only after maximum line broadening had been obtained from adjustments to the spatial distribution. The empirical velocity curve for comet Wilson is steeper than for comet Halley postperihelion with velocities at large  $r$  up to 50% higher than even Halley's high postperihelion values. Such high velocities were important to fitting the negative velocity wing of Wilson's observed line profile. This fit indicates that some H<sub>2</sub>O molecules, presumably those at radial distances of many scale-lengths, were accelerated to velocities up to  $\approx 4$  km sec<sup>-1</sup>. L89's previous analysis of these data indicated that the outflow velocity had to be  $> 2$  km sec<sup>-1</sup> in parts of the coma, but they did not present a velocity profile.

The only other kinematic analyses of comet Wilson were by TGSC and Bockelée-Morvan *et al.* (1990) using radio OH line profile averages from March and May, 1987. TGSC derived small day/night anisotropy factors ( $\approx 1.5$ ) and low values of  $v_{\text{H}_2\text{O}}$  ( $\approx 0.7$  km sec<sup>-1</sup> at 1.26 AU) which differ substantially from our asymmetry factor ( $\approx 12$ , see Fig. 6.13) and  $v_{\text{H}_2\text{O}}$  measurement ( $\approx 2$  km sec<sup>-1</sup> at  $r = 10^4$  km, see Fig. 6.6). Likewise, Bockelée-Morvan *et al.* (1990) derived  $v_{\text{H}_2\text{O}} = 0.7 \pm 0.1$  km sec<sup>-1</sup>. The H<sub>2</sub>O and OH observations were separated by approximately one month so the retrieved velocities need not be equal, but the differences, if real, are so large as to be interesting

in themselves.

The high outflow velocities observed in comet Halley postperihelion initially presented a challenge to modelers because there was little precedent for them. These measurements now seem less provocative because they are supported by new models in which the treatment of production rates, spatial anisotropy, recondensation, radiative trapping, and other coma processes can lead to high outflow velocities. It is not clear how the progress in understanding conditions in Halley's coma can be applied to comet Wilson, however. Its measured  $Q_{\text{H}_2\text{O}}$  was not unusually high (see Table 6.1) and its outflow was not concentrated in narrow, high density, time-dependent features. Both conventional wisdom and the insight gained from kinematic analyses of Halley's coma suggest that Wilson's expansion velocity should be more or less in accord with standard hydrodynamic models. In order to accept a result that is contrary to these expectations there should be no questions associated with either the comet's behavior or the observations. Of particular concern are factors that could shift or broaden spectral lines anomalously. Path difference sampling errors or optical misalignment in an FTS would produce obvious phase distortion in the transformed spectrum, but we already noted the symmetry in the partially resolved observed  $\text{H}_2\text{O}$  line in Fig. 6.11. If the comet's  $\text{H}_2\text{O}$  flux decreased during observations the observed line profile would become optically apodized, that is, broader with attenuated side lobes. The opposite (*i.e.*, an  $\text{H}_2\text{O}$  outburst) occurred during observations of comet Halley which rendered the recorded interferogram unusable in the conventional sense (Larson *et al.* 1990). Comet Wilson did not exhibit any rapid temporal variability, however, and *rapid fading* is implausible

on physical grounds anyway. All line positions in a Fourier spectrum are referred to the single reference wavelength (6328 Å) used to command samples from the interferogram. The accuracy of individual, strong H<sub>2</sub>O line positions in comet Wilson's spectrum was  $\pm 0.002 \text{ cm}^{-1}$  or  $\pm 0.15 \text{ km sec}^{-1}$  (L89) after corrections were applied for non-standard air, finite size of the FOV, and residual uncertainty in the reference wavelength. The same calibration procedure applied to other spectra acquired during and after the Wilson flight program revealed no systematic error comparable to the large blue-shift in Wilson's H<sub>2</sub>O lines. Thus, we cannot identify any adverse influence on either the widths or the positions of the cometary H<sub>2</sub>O lines. Note that both of these line profile parameters would have to be reduced in order to make  $v_{\text{H}_2\text{O}}$  consistent with standard hydrodynamic predictions for Wilson's coma (*i. e.*,  $\approx 1 \text{ km sec}^{-1}$ ). If the line width were made very small ( $\approx 1 \text{ km sec}^{-1}$ , for example), the observed line position would still require that  $v_{\text{H}_2\text{O}} > 1.5 \text{ km sec}^{-1}$ , whereas if the line shift were reduced ( $< 0.3 \text{ km sec}^{-1}$ , for example) the observed line width would keep  $v_{\text{H}_2\text{O}} > 1.4 \text{ km sec}^{-1}$ . Thus, we would have to invoke multiple, independent sources of systematic error to make such revisions to our line profile analysis, but since none can be identified the case for accepting the measurements at face value is strengthened.

Our high retrieved velocity for comet Wilson therefore presents a special challenge: to identify another source of coma heating that was not relevant to comet Halley. One of the compelling reasons for conducting airborne observations of comet Wilson was to compare dynamically "old" and "new" comets for the first time with high resolution IR spectra. One anticipated difference between Halley and Wilson was the

composition and morphology of their surfaces. We already noted that Wilson's spatial anisotropy and temporal behavior are consistent with a much less evolved surface physically than Halley's. Wilson's surface material, however, could have been very evolved chemically compared to Halley's because of radiation damage from long term exposure to ionizing radiation in the Oort cloud. This mechanism is capable of producing new volatiles and refractory solids within the first few meters of parent molecular material (for background see Johnson *et al.* 1987 and references therein). The presence of these chemical modifications in new comets has been linked to their early brightening and to the formation of thermally stable crusts prior to their first passage through the inner solar system. There may be additional consequences of warming up this radiation-processed material that have not yet been considered, such as its influence on energy balance in the coma. Specifically, could the high observed value of  $v_{\text{H}_2\text{O}}$  be indicative of latent chemical energy released in exothermic reactions in a radiation-processed "primordial" crust? No models deal with this situation but the possibility is at least consistent with the constraint that it not be relevant to Halley which would have lost its radiation-processed crust long ago. It is tempting to relate this type of surface to Wilson's thermal spectrum. Lynch *et al.* (1989) observed both a broad silicate emission feature at 10  $\mu\text{m}$  and a narrow emission line at 12.2  $\mu\text{m}$ . The 12.2- $\mu\text{m}$  feature was not previously seen in comets nor could Lynch *et al.* assign it convincingly to a mineral. Moreover, the 10- $\mu\text{m}$  silicate feature disappeared between 25 April and 1 June 1987. Lynch *et al.* concluded that there were compositional inhomogeneities in Wilson's nucleus and two chemically distinct grain populations. Pursuing this idea, we

suggest that the unassigned 12.2- $\mu\text{m}$  feature could be due to a radiation-processed species and the change in silicate emission could represent the transition from erosion of the last of the radiation-processed crust to the onset of mass loss from the underlying primordial material. This scenario itself is reasonable but there is no obvious link to  $v_{\text{H}_2\text{O}}$ . We therefore conclude that the high  $\text{H}_2\text{O}$  expansion velocity in comet Wilson cannot be explained with available kinematic models of cometary comae.

## 6.4. Summary

### 6.4.1. Outflow Distribution.

The three deconvolved cometary  $\text{H}_2\text{O}$  line profiles are compared in Fig. 6.14 to each other and to a synthetic line assuming isotropic outflow at constant expansion velocity (*i.e.*, a Haser profile). All of the observed cometary lines are shifted in position relative to the symmetric case, indicating that asymmetric outflow was common to these otherwise dissimilar comets. The Gaussian appearance of the observed cometary line shapes is due primarily to velocity dispersion from collisions while their positions and widths are influenced by anisotropic outflow and the radial expansion velocity. None of the observed  $\text{H}_2\text{O}$  line profiles even remotely resembles the symmetric case. One conclusion that clearly emerges from Fig. 6.14, therefore, is that spherically symmetric, monokinetic outflow is unrealistic for modeling parent molecule distributions in comets. This result is not in itself surprising because there are so many other observational and theoretical indications of asymmetric outflow, but this is the first time that anisotropy has been traced from the nucleus to  $r > 10^4$  km with  $\text{H}_2\text{O}$ , the most

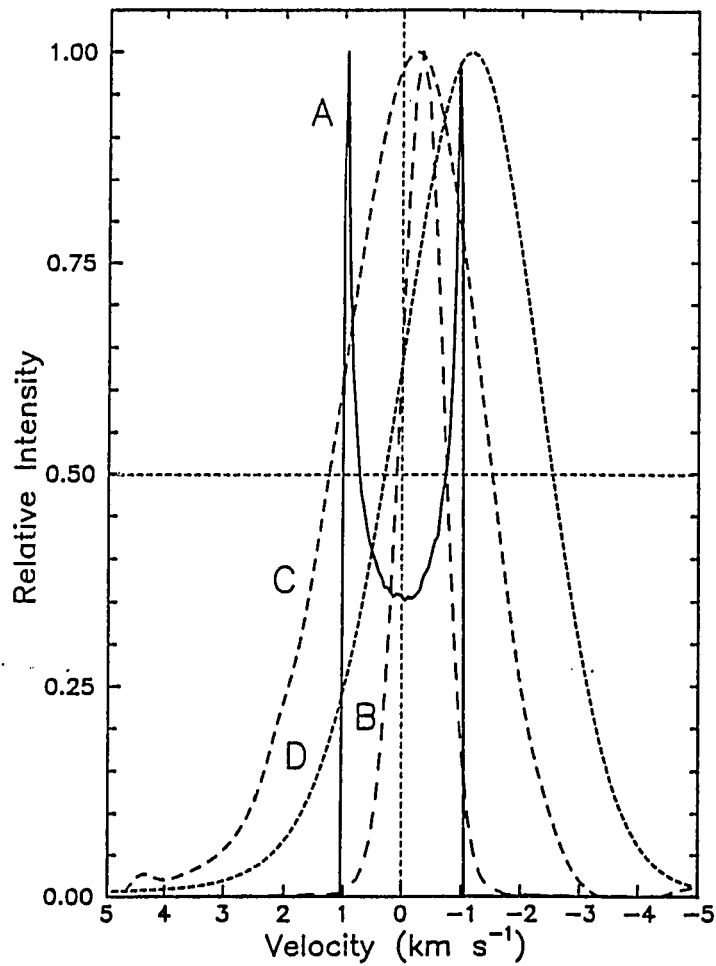


**Figure 6.14.** Comparison of the synthetic  $\text{H}_2\text{O}$  line profiles fit to comets Halley and Wilson with a Haser line profile. *A.* Haser model: spherically symmetric outflow at uniform velocity. *B.* Comet Halley preperihelion. *C.* Comet Halley postperihelion. *D.* Comet Wilson.

abundant parent molecule in the coma. Kinematic studies of OH and HCN at radio wavelengths demonstrate that gas anisotropy actually extends to at least  $r \approx 10^6$  km. Even before Halley's last apparition, Bockelée-Morvan and Gérard (1984) attributed asymmetries in observed radio OH line profiles to anisotropic outflow of H<sub>2</sub>O, the presumed parent. They concluded as we do that a Haser model is inappropriate for the parent distribution [although it is still retained in the latest models (see *e.g.*, Bockelée-Morvan *et al.* 1990)].

#### 6.4.2. Outflow Velocity.

The expansion velocity is a manifestation of energy balance in the coma, hence its importance as an observable to identifying and understanding the roles of competing heating and cooling mechanisms. This parameter has received much attention following Halley's last apparition as observations and theory emphasized the need to consider more complex interactions than just simple balance between photolytic heating and radiative cooling. The convenient assumption of uniform radial expansion velocity has been suspect for some time and the spectroscopic results presented and reviewed in this paper demonstrate convincingly that during a comet's apparition  $v_{\text{H}_2\text{O}}$  depends upon more parameters than just  $R_h$  (*e.g.*,  $v_{\text{H}_2\text{O}} = 0.58R_h^{-1/2}$ , Delsemme 1982). Models now predict significant influence on  $v_{\text{H}_2\text{O}}$  by  $Q_{\text{H}_2\text{O}}$  (at least above a certain threshold value), spatial anisotropy, H<sub>2</sub>O recondensation, optical trapping, and the gas-to-dust ratio (Crovisier 1984, Bockelée-Morvan and Crovisier 1987b, Combi 1989, Crifo 1990). The Gaussian line shapes of the H<sub>2</sub>O line profiles in Fig. 6.14 contrast dramatically with the sharp, vertical profile based on constant  $v_{\text{H}_2\text{O}}$  and their widths and high velocity wings require

that  $v_{\text{H}_2\text{O}}$  increase with radial distance in the coma. Our retrieved velocity profiles in Fig. 6.14 provide the first opportunity using remote observations to compare the *radial dependence* of  $v_{\text{H}_2\text{O}}$  rather than just an average value to outflow models. The most obvious result is the individuality of the curves. In addition, the continuing rise in  $v_{\text{H}_2\text{O}}$  at  $r > 10^4$  km is diagnostic of heating in the outer coma, a condition that warrants further study.

#### 6.4.3. Surface Properties

The spatial distributions fit to the observed line profiles, augmented by other evidence such as temporal variability, constitute important remote signatures of the surface properties of cometary nuclei. The narrow line profile for comet Halley preperihelion, for example, would have inevitably been associated with jets even without the insight provided by spacecraft images a few months later.

## CHAPTER 7.

### SUMMARY AND DISCUSSION

In this study we addressed two major issues in cometary modeling: theoretical models of cometary comae, and methods to infer kinematic properties. In Chapter 2 we developed a new gas dynamic model for the neutral coma based on the concepts of dilute gas theory. In our approach, we recognized the discrete nature of a gas molecular system and described the movement of molecules in terms of a probability function  $f = \{f_s(\mathbf{r}, \mathbf{v}, \epsilon_k, t) : s = \text{H}_2\text{O}, \text{OH}, \text{H}, \text{HCN}, \dots ; k = 1, 2, \dots\}$ . This distribution function is related to its variables by the cometary Boltzmann equation. Theoretically speaking, the cometary Boltzmann equation fully describes dynamic processes inside the coma. Given proper initial and boundary conditions the explicit dependence of the distribution function  $f$  upon spatial and temporal coordinates can be found through numerical integration. Knowledge of the distribution function  $f$  allows us to calculate all macroscopic properties inside the coma, such as temperature, pressure, and outflow velocity.

In Chapter 3 we used our dilute gas model to compare previous physical models of the coma. We demonstrated that the hydrodynamic equations and Haser's formulae are limiting cases of our dilute gas theory. In the inner coma where intermolecular collisions are intensive and the mean free path is small, the cometary Boltzmann equation reduces to the hydrodynamic equations and the two approaches give equivalent results. In the outer coma the mean free path for molecules becomes very large and the

hydrodynamic approach becomes invalid. The cometary Boltzmann equation, on the other hand, remains valid and reduces to the Haser formulae if Haser's assumptions are applied.

Our dilute gas model is built on a very general platform. For example, the key parameters in traditional molecular excitation models are the relative populations of the energy levels for each molecular species. This is replaced in our theory by the distribution function  $f_s(\mathbf{r}, \mathbf{v}, \epsilon_k, t)$ . As a result, molecular excitation models become essentially a subset of our model. Also, the statistical equilibrium equation in excitation models is not self-consistent and needs additional input from other models. In our case the presence of the distribution function allows us to establish a self-consistent dynamic equation: the cometary Boltzmann equation.

In §3.3 we proposed a general algorithm for implementing Monte Carlo particle trajectory models. We view all previous MCPTM's as specific applications of this algorithm and ignore differences between them in order to concentrate on the relationship between the statistical approach and the cometary Boltzmann equation. We demonstrated that the general MCPTM algorithm is a statistical method for solving the cometary Boltzmann equation. Other methods, such as direct Monte Carlo simulation techniques, are available to solve the classic Boltzmann equation numerically and may be generalized for our cometary Boltzmann equation.

In Chapter 4 we generalized gas density distributions directly from the cometary transport equation. The unrealistic assumptions associated with Haser's formulae, such as collisionless outflow and uniform expansion velocity, were eliminated. In addition,

anisotropic number density distribution function. These formulae provide the necessary tools to interpret both *in situ* and remote observations.

In Chapter 5 we built a spectral outflow model for simulating velocity-resolved spectral line profiles in cometary comae. We demonstrated that the line broadening in an observed profile is primarily due to LOS components of the coma expansion velocity and velocity components acquired during collisions inside the coma. Such line profiles can therefore provide much information about kinematic properties inside the coma. To retrieve the kinematic parameters, we map the predicted density distributions into synthetic line profiles for comparison with observations. A Monte Carlo computational procedure was implemented to calculate the three-dimensional integral. Our initial use of the model showed that the expansion velocity and spatial anisotropy in the outflow have the largest influence on the line width, while the FOV and kinetic temperature change the shape of a line profile dramatically. We found that the Haser model, frequently used to analyze spectral data, is inadequate to interpret observed line profiles.

In Chapter 6 we utilized the spectral outflow model to analyze velocity-resolved spectral line profiles of H<sub>2</sub>O in comets P/Halley and Wilson. We presented our results as synthetic spectral line profiles, two-dimensional column density maps, empirical velocity curves, and density profiles along hypothetical spacecraft trajectories, each of which conveys complementary insight into coma conditions. In most instances our results were consistent with other measurements when they were suitable for direct comparison. Our results demonstrate that detailed kinematic information can be extracted from remote, wide-field spectroscopic observations of parent molecules in any

reasonably bright comet. The techniques can be considerably refined when high resolution IR imaging spectrometers and new high altitude observing platforms (*e.g.*, *SOFIA*) become available.

Further study of our dilute gas model may proceed in three directions. First, the model should be expanded to include general treatments of the dust and plasma components of the coma. Second, new approximations and simplifying models should be found in order to interpret observations. Finally, numerical procedures should be formulated in order to solve the cometary Boltzmann equation directly.

In summary, our new gas dynamic model already provides a solid theoretical foundation for coma modeling. Further development of this approach should allow calculation of very complex density distributions and kinematic properties in the coma, which then can be used to interpret the increasingly detailed data that are being obtained.

## LIST OF REFERENCES

- A'HEARN, M. F., S. HOBAN, P. V. BIRCH, C. BOWERS, R. MARTIN, AND D. A. KLINGLE-SMITH 1986. Cyanogen jets in comet Halley. *Nature* **324**, 649-651.
- ALLEN, M., M. DELITSKY, W. HUNTRESS, Y. YUNG, W.-H. IP, R. SCHWENN, H. ROSENBAUER, E. SHELLY, H. BALSIGER, AND J. GEISS 1987. Evidence for methane and ammonia in the coma of comet P/Halley. *Astron. Astrophys.* **187**, 502-512.
- BIRD, G. A. 1976. *Molecular Gas Dynamics*. Oxford University Press, London.
- BOCKELÉE-MORVAN, D. 1987. A model for the excitation of water in comets. *Astron. Astrophys.* **181**, 169-181.
- BOCKELÉE-MORVAN, D., AND E. GÉRARD. 1984. Radio observations of the hydroxyl radical in comets with high spectral resolution. Kinematics and asymmetries of the OH coma in C/Meier (1978 XXI), C/Bradfield (1979 X), and C/Austin (1983 g). *Astron. Astrophys.* **131**, 111-122.
- BOCKELÉE-MORVAN, D., J. CROVISIER, D. DESPOIS, T. FORVILLE, E. GÉRARD, J. SCHRAML, AND C. THUM. 1986. A search for parent molecules at millimeter wavelengths in comets P/Giacobini-Zinner 1984e and P/Halley 1982i. In *Proc. 20th ESLAB Symposium on the Exploration of Halley's Comet*, ESA SP-250, Vol. I, 365-367.
- BOCKELÉE-MORVAN, D., AND J. CROVISIER. 1987a. The 2.7  $\mu\text{m}$  water band of comet P/Halley: interpretation of observations by an excitation model. *Astron. Astrophys.* **187**, 425-430.
- BOCKELÉE-MORVAN, D., AND J. CROVISIER. 1987b. The role of water in the thermal balance of the coma. In *Proceedings, Symposium on the Diversity and Similarity of Comets*, ESA SP-278, 235-240.
- BOCKELÉE-MORVAN, D., J. CROVISIER, AND E. GÉRARD 1990. Retrieving the coma gas expansion velocity in P/Halley, Wilson (1987 VII) and several other comets from the 18-cm OH line shapes. *Astron. Astrophys.*, **238**, 381-400.
- CAMPINS, H., D.J. LIEN, R. DECHER, C.M. TELESKO, AND K.S. CLIFTON. 1989. Infrared imaging of the coma of comet Wilson. *Icarus* **80**, 289-302.
- CELNIK, W. E., AND TH. SCHMIDT-KALER 1987. Structure and dynamics of plasma-

- tail condensations of comet P/Halley 1986 and inferences on the structure and activity of the cometary nucleus. *Astron. Astrophys.* **187**, 233-248.
- CHAPMAN, S., AND T.G. COWLING 1970. *The Mathematical Theory of Non-uniform Gases (3rd Ed.)*. Cambridge University Press, London.
- CHIN, G., AND H. A. WEAVER 1984. Vibrational and rotational excitation of CO in comets. *Astrophys. J.* **285**, 858-869.
- COMBI, M. R. 1989. The outflow speed of the coma of Halley's comet. *Icarus* **81**, 41-50.
- COMBI, M. R., AND A. H. DELSEMME 1980. Neutral cometary atmospheres - 1. An average random walk model of photodissociation in comets. *Astrophys. J.* **237**, 633-340.
- COMBI, M. R., AND W. H. SMYTH 1988. Monte Carlo particle-trajectory models for neutral cometary gases. I. Models and equations. *Astrophys. J.* **327**, 1026-1043.
- CROVISIER, J. 1984. The water molecule in comets: fluorescence mechanisms and thermodynamics of the inner coma. *Astron. Astrophys.* **130**, 361-372.
- CROVISIER, J. 1987. Rotational and vibrational synthetic spectra of linear parent molecules in comets. *Astron. Astrophys. Suppl. Ser.* **68**, 223-258.
- CRIFO, J. F. 1989. Collisional coma models: an unorthodox overview. *Adv. Space Res.* **9**, 197-211.
- CRIFO, J. F. 1990. Water clusters in the coma of comet Halley and their effect on the gas density, temperature, and velocity. *Icarus* **84**, 414-446.
- CURTIS, C. C., C. Y. FAN, K. C. HSIEH, D. M. HUNTEN, W.-H. IP, E. KEPPLER, A. K. RICHTER, G. UMLAUFT, V. V. AFONIN, A. V. DYACHKOV, J. ERÖ, AND A. J. SOMOGYI. 1987. Comet P/Halley neutral gas density profile along the Vega-1 trajectory measured by the neutral gas experiment. *Astron. Astrophys.* **187**, 360-362.
- DAVIS, D. S., H. P. LARSON, M. WILLIAMS, G. MICHEL, AND P. CONNES. 1980. Infrared Fourier spectrometer for airborne and ground-based astronomy. *Appl. Optics* **19**, 4138-4155.
- DELSEMME, A. H. 1982. Chemical composition of cometary nuclei. In *Comets* (L.L. Wilkening, Ed.), 85-130. Univ. of Arizona Press, Tucson.

- DESPOIS, D., E. GÉRARD, J. CROVISIER, AND I. KAZES 1981. The OH radical in comets: observation and analysis of the hyperfine microwave transitions at 1667 MHz and 1665 MHz. *Astron. Astrophys.* **99**, 320-340.
- EDDINGTON, A. S. 1910. The envelopes of comet Morehouse. *M. N. R. A. S.* **70**, 422-458.
- FESTOU, M. C. 1981. The density distribution of neutral compounds in cometary atmospheres. I. Models and equations. *Astron. Astrophys.* **95**, 69-79.
- FINK, U., AND M. DISANTI 1990. The production rate and spatial distribution of H<sub>2</sub>O for comet P/Halley. *Astrophys. J.* **364**, 687-698.
- GÉRARD, E., D. BOCKELÉE-MORVAN, G. BOURGOIS, P. COLOM, AND J. CROVISIER. 1987. 18-cm wavelength radio monitoring of the OH radical in comet P/Halley 1982i. *Astron. Astrophys.* **187**, 455-461.
- GRINGAUZ, K. I., T. I. GOMBOSI, A. P. REMIZOV, I. APÁTHY, I. SZEMEREY, M. I. VERIGIN, L. I. DENCHIKOVA, A. V. DYACHKOV, E. KEPPLER, I. N. KLIMENKO, A. K. RICHTER, A. J. SOMOGYI, K. SZEGÖ, S. SZENDRŐ, M. TÁTRALLYAY, A. VARGA, AND G. A. VLADIMIROVA. 1986. First *in situ* plasma and gas measurements at comet Halley. *Nature* **321**, 282-285.
- GOMBOSI, T. I., AND M. HORANYI 1986. Time-dependent numerical modeling of dust halo formation at comets. *Astrophys. J.* **311**, 491-500.
- GULL, S. F., AND J. SKILLING 1984. Maximum entropy method in image processing. *Proc. IEEE.* **131**, Pt. F, 646-659.
- HASER, L. 1957. Distribution d'intensité dans la tête d'une comète. *Bull. Acad. Roy. Belgique (Cl. Sci.)* **43**, 740-750.
- HAVILAND, J. K. 1965. In *Methods of Computational Physics* (B. Alder et al., Ed.). Academic Press, New York. **4**, 109.
- HODGES, R. R. 1990. Monte Carlo simulation of nonadiabatic expansion in cometary atmospheres: Halley. *Icarus* **83**, 410-433.
- HSIEH, K.C., C.C. CURTIS, C.Y. FAN, D.M. HUNTEN, W.-H. IP, E. KEPPLER, A.K. RICHTER, G. UMLAUFT, V.V. AFONIN, J. ERÖ, AND A.J. SOMOGYI. 1987. Anisotropy of the neutral gas distribution of comet P/Halley deduced from NGE/Vega 1 measurements. *Astron. Astrophys.* **187**, 375-379.

- HU, H.-Y., H.P. LARSON, AND K.C. HSIEH. 1991. Theoretical description of spectral line profiles of parent molecules in cometary comae. *Icarus*, **91** in press.
- HUEBNER, W. F., AND J. J. KEADY 1983. Energy balance and photochemical processes in the inner coma. In *Cometary Exploration* (T.T. Gombosi, Ed.), **1**, 165-183. Academic Press, Budapest.
- IP, W.-H. 1985. An overview of gas phenomena in comet Halley. *Adv. Space Res.* **5**, 233-245.
- JOHNSON, R.E., J.F. COOPER, L.J. LANZEROTTI, AND G. STRAZZULLA. 1987. Radiation formation of a non-volatile comet crust. *Astron. Astrophys.* **187**, 889-892.
- KALOS, M. H., AND P. A. WHITLOCK 1986. *Monte Carlo Methods, Vol. I: Basics*, John Wiley & Sons, New York.
- KELLER, H.U., W.A. DELAMERE, W.F. HUEBNER, H.J. REITSEMA, H.U. SCHMIDT, F.L. WHIPPLE, K. WILHELM, W. CURDT, R. KRAMM, N. THOMAS, C. ARPIGNY, C. BARBIERI, R.M. BONNET, S. CAZES, M. CORADINI, C.B. COSMOVICI, D.W. HUGHES, C. JAMAR, D. MALAISE, K. SCHMIDT, W.K.H. SCHMIDT, AND P. SEIGE. 1987. Comet P/Halley's nucleus and its activity. *Astron. Astrophys.* **187**, 807-823.
- KITAMURA Y. 1986. Axisymmetric dusty-gas jet in the inner coma of a comet. *Icarus* **66**, 241-257.
- KITAMURA Y. 1987. Axisymmetric dusty-gas jet in the inner coma of a comet II. The case of isolated jets. *Icarus* **72**, 555-567.
- KITAMURA, Y., AND T. YAMAMOTO 1985. Hydrodynamic study of condensation and sublimation of ice particles in cometary atmospheres. *Icarus*, **68** 266-275.
- KITAMURA, Y., U. ASHIHARA, AND T. YAMAMOTO 1985. A model for the hydrogen coma of a comet. *Icarus* **61**, 278-295.
- KÖMLE, N.I., AND W.-H. IP, 1987. A model of the anisotropic structure of the neutral gas coma of a comet. In *Symposium on the Diversity and Similarity of Comets*, ESA SP-278, 247-254.
- KOROSMEZEY, A., AND T. I. GOMBOSI 1990. A time-dependent dusty gas dynamic model of axisymmetric cometary jets. *Icarus* **84**, 118-153.

- KRANKOWSKY, D., P. LÄMMERZAHN, I. HERRWERTH, J. WOWERIES, P. EBERHARDT, U. DOLDER, U. HERRMANN, W. SCHULTE, J.J. BERTHELIER, J.M. ILLIANO, R.R. HODGES, AND J.H. HOFFMAN. 1986. *In situ* gas and ion measurements at comet Halley. *Nature* 321, 326-329
- KRASNOPOLSKY, V. A., A. YU. TKACHUK, G. MOREELS, AND M. GOGOSHEV 1988. Water vapor and hydroxyl distributions in the inner coma of comet P/Halley measured by the Vega 2 three-channel spectrometer. *Astron. Astrophys.* 203, 175-182.
- LÄMMERZAHN, P., D. KRANKOWSKY, R.R. HODGES, U. STUBBEMANN, J. WOWERIES, I. HERRWERTH, J.J. BERTHELIER, J.M. ILLIANO, P. EBERHARDT, U. DOLDER, W. SCHULTE, AND J.H. HOFFMAN. 1987. Expansion velocity and temperatures of gas and ions measured in the coma of comet P/Halley. *Astron. Astrophys.* 187, 169-173.
- LANDAU, L. D., AND E. M. LIFSHITZ 1959. *Fluid Mechanics*. Pergamon Press, Oxford, England.
- LARSON, H.P., M.J. MUMMA, AND H.A. WEAVER. 1987. Kinematic properties of the neutral gas outflow from comet P/Halley. *Astron. Astrophys.* 187, 391-397.
- LARSON, H.P., H.A. WEAVER, M.J. MUMMA, AND S. DRAPATZ. 1989. Airborne infrared spectroscopy of comet Wilson (1986 $\ell$ ) and comparisons with comet Halley. *Astrophys. J.* 338, 1106-1114.
- LARSON, H.P., H.-Y. HU, M.J. MUMMA, AND H.A. WEAVER. 1990. Outbursts of H<sub>2</sub>O in comet P/Halley. *Icarus* 86, 129-151.
- LARSON, H.P., H.-Y. HU, K. C. HSIEH, H. A. WEAVER, AND M. J. MUMMA 1991. Descriptions of the neutral gas outflow in comets P/Halley and Wilson (1986 $\ell$ ) from analysis of velocity-resolved H<sub>2</sub>O line profiles. *Icarus*, 91, in press.
- LIFSHITZ, E. M., AND PITAEVSKII 1981. *Physical Kinetics*. Pergamon press, Oxford, England.
- LYNCH, D.K., R.W. RUSSELL, H. CAMPINS, F.C. WITTEBORN, J.D. BREGMAN, D.M. RANK, AND M. COHEN. 1989. 5-to 13- $\mu$ m airborne observations of comet Wilson (1986 $\ell$ ). *Icarus* 82, 379-388.
- MAGEE-SAUER, K., F. L. ROESLER, F. SCHERB, AND J. HARLANDER 1988. Spatial distribution of O(<sup>1</sup>D) from comet Halley. *Icarus* 76, 89-99.

- MCFADDEN, L.A., M.F. A'HEARN, P.D. FELDMAN, E.E. ROETTGER, D.M. EDSALL, AND P.S. BUTTERWORTH. 1987. Activity of comet P/Halley 23-25 March, 1986: IUE observations. *Astron. Astrophys.* **187**, 333-338.
- MENDIS, D. A., L. F. HOUPIS, AND M. L. MARCONI 1985. Physics of comets. In *Fundamentals of Cosmic Physics* **10**, 1-380.
- MUMMA, M.J., H. A. WEAVER, H. P. LARSON, D. S. DAVIS, AND M. WILLIAMS 1986. Detection of water vapor in Halley's comet. *Science* **232**, 1523-1528.
- MUNTZ, E. P., D. WEAVER, AND D. CAMPBELL (Eds.) 1989. Rarefied Gas Dynamics. *Proceedings of the 15th international Symposium, Progress in Astronautics and Aeronautics*. In press.
- MUNTZ, E. P. 1989. Rarefied Gas Dynamics. *Ann. Rev. Fluid Mech.* **21**, 387-417.
- REMIZOV, A. P., M. I. VERIGIN, K. I. GRINGAUZ, I. APÁTHY, I. SZEMEREY, T. I. GOMBOSI, AND A. K. RICHTER 1986. In *Proc. 20th ESLAB Symposium on the Exploration of Halley's Comet*, ESA SP-250, Vol. 1, 387-390.
- RETTIG, T.W., J.R. KERN, R. RUCHTI, B. BAUMBAUGH, A.E. BAUMBAUGH, K.L. KNICKERBOCKER, AND J. DAWE. 1987. Observations of the coma of comet P/Halley and the outburst of 1986 March 24-25 (UT). *Astron. Astrophys.* **187**, 249-255.
- REUTER, D. M., M. J. MUMMA, AND S. NADLER 1989. Infrared fluorescence efficiencies for the  $\nu_1$  and  $\nu_5$  bands of formaldehyde in the solar radiation field. *Astrophys. J.* **341**, 1045-1058.
- ROETTGER, E.E., P.D. FELDMAN, M.F. A'HEARN, M.C. FESTOU, L.A. MCFADDEN, AND R. GILMOZZI. 1989. IUE observations of the evolution of comet Wilson (1986 $\ell$ ): comparison with P/Halley. *Icarus* **80**, 303-314.
- SCHLOERB, F.P., W.M. KINZEL, D.A. SWADE, AND W.M. IRVINE. 1986. HCN production from comet Halley. *Astrophys. J. Lett.* **310**, L55-L60.
- SCHLOERB, F.P., W.M. KINZEL, D.A. SWADE, AND W.M. IRVINE. 1987a. Observations of HCN in comet P/Halley. *Astron. Astrophys.* **187**, 475-480.
- SCHLOERB, F.P., M.J. CLAUSSEN, AND L. TACCONI-GARMAN. 1987b. OH radio observations of comet P/Halley. *Astron. Astrophys.* **187**, 469-474.
- SHIMIZU, M. 1976. The structure of cometary atmospheres I: temperature distribution.

*Astrophys. Space Science* **40**, 149-155.

- TACCONI-GARMAN, L.E. 1989. Kinematic models of cometary comae. Ph. D. Dissertation, University of Massachusetts.
- TACCONI-GARMAN, L.E., F. P. SCHLOERB, AND M. J. CLAUSSEN 1990. High spectral resolution observations and kinematic modeling of the 1667 MHz hyperfine transition of OH in Comets Halley (1982i) Giacobini-Zinner (1984e), Hartley-Good (1985l), Thiele(1985m), and Wilson (1986l). *Astrophys. J.* **364**, 672-686.
- WEAVER, H. A., AND M. J. MUMMA 1984. Infrared molecular emissions from comets. *Astrophys. J.* **276**, 782-796.
- WEAVER, H.A., MUMMA, M.J., LARSON, H.P., AND DAVIS, D.S. 1986. Post-perihelion observations of water in comet Halley. *Nature* **324**, 441-444.
- WEAVER, H.A., M. J. MUMMA, AND H. P. LARSON 1987. Infrared investigation of water in comet P/Halley. *Astron. Astrophys.* **187**, 411-418.
- WHIPPLE, F. L. 1950. A comet model. Part I. The acceleration of comet Encke. *Astrophys. J.* **111**, 375-394.
- WHIPPLE, F. L. 1951. A comet model. Part II. Physical relations for comets and meteors. *Astrophys. J.* **113**, 464-474.